Superconductivity in Graphene Hetero-Structures: From Fundamental Physics to Functional Devices

Thesis by
Harpreet Singh Arora

In Partial Fulfillment of the Requirements for the
Degree of
Doctor of Philosophy

CALIFORNIA INSTITUTE OF TECHNOLOGY
Pasadena, California

2020
Defended June 4th, 2020

Harpreet Singh Arora
ORCID: 0000-0002-7674-735X

ACKNOWLEDGEMENTS

I'd like to begin by thanking my advisor Stevan for his continued support and mentorship through the last five years. Being the first member of the lab and not having any postdocs or senior students for guidance in the early stages of my PhD was particularly challenging. However, Stevan was always there to assist and nudge me in the right direction. Despite having a very hands-on approach to advising, he provided with me a lot of intellectual and creative freedom to craft my own projects. The interactive nature of our relationship has helped me become a better problem solver – an asset I will forever cherish.

I also want to thank Profs. Michael Roukes, Tom Rosenbaum, and Dave Hsieh for taking time out of their busy schedules to serve on my committee. Michael has been an amazing collaborator for our experiments related to thermometry in graphene. His enthusiasm about physics in general is very contagious, and discussions with him left me feeling energized about my scientific quests. Running into Tom randomly on the Caltech campus was a source of joy at all times. I will always admire how his humility shines through in every interaction I've had with him. Dave provided a sympathetic ear to problems faced by students in a highly competitive field, and his advice based on his own experience was priceless.

I consider myself very fortunate to have colleagues like Robbie Polski, Yiran Zhang, Jeannette Kemmer, Youngjoon Choi, Hyunjin Kim, and Hechen Ren. They helped create an atmosphere of collegiality in the lab, which helped me thrive. They also challenged me when I was wrong and showed me the value of constructive feedback. I hope all of you are successful in whatever endeavors you choose to pursue. I was also lucky to work with brilliant collaborators at Caltech who were crucial to the success of projects I worked on: Olli Saira, Alex Thomson, Raj Katti, Ewa Rej, Matt Matheny, and Prof. Jason Alicea. Special thanks to Christy, Angie, Cecilia, and Jennifer for making sure every non-scientific matter during my time at Caltech was resolved smoothly.

Finally, I want to thank the most important part of my life – my family. My parents for loving me unconditionally but also pushing me to be the best version of myself. Being twelve time zones away from you was one of the most difficult things I faced during my PhD. My grandparents, and my aunt and uncle for always cheering me on. My brother and sister-in-law for encouraging me to apply to Caltech and offering

invaluable guidance throughout my career. My Mediterranean-themed pups, Olive and Caper, for being excited to see me every single day when I got home, no matter how the day was. My love and my wife Jessica - thank you for never failing to remind me of my unique virtues on the many down days of a graduate career. Thank you also for making the joyous moments more memorable. Long walks with you and the pups always restore balance in my life.

ABSTRACT

While graphene has been dubbed as a "wonder material" because of its amazing characteristics, such as the ability to conduct electricity better than copper and being two hundred times stronger than steel, until recently, the key quantum phenomenon of superconductivity was missing from the list of properties exhibited by graphene. In 2018, an astonishing discovery showed that by placing two sheets of graphene on top of each other in a structure known as Twisted Bilayer Graphene, it is possible to realize superconductivity when the rotation angle between the sheets is close to the "Magic Angle" value of 1.1°. More surprisingly, superconductivity in the initial reports was observed in close proximity to insulating states - resembling the phase diagram of High T_c superconductors. This sparked a fierce debate about its origin and its possible relation to High T_c superconductors. In this thesis, we show that by carefully engineering the dielectric environment of TBG, it is possible to stabilize superconductivity in non-magic angle TBG devices without the presence of any insulating states. This discovery imposes severe constraints on the origin of superconductivity in TBG. We also report, for the first time, the successful induction of spin-orbit coupling in TBG and discuss its implications.

Superconductivity can also be induced into graphene via coupling to conventional superconductors, and the strength of the induced supercurrent depends strongly on temperature. We employ this thermal dependence by integrating graphene into superconducting circuits that serves two purposes a) to investigate graphene's thermal behavior at milliKelvin temperatures and b) to utilize its extremely low heat capacity in making functional devices that have the potential to achieve ultra-high thermal sensitivity.

PUBLISHED CONTENT AND CONTRIBUTIONS

Arora H.S., Polski R., Zhang Y., Thomson A., Choi Y., Kim H., Lin Z., Wilson I.Z., Xu X, Chu J-H, Watanabe K., Taniguchi T., Alicea J., Nadj-Perge S.
"Superconductivity in metallic twisted bilayer graphene stabilized by monolayer WSe_2". *Nature* (2020), In press.
H.A. designed the experiment. H.A. made the TBG-WSe_2 devices. H.A. performed the measurements. H.A. co-analyzed the data. H.A. assisted with the manuscript writing.

Y. Choi, J. Kemmer, Y. Peng, A. Thomson, H. Arora, R. Polski, Y. Zhang, H. Ren, J. Alicea, G. Refael, F. von Oppen, K. Watanabe, T. Taniguchi, S. Nadj-Perge, "Electronic correlations in twisted bilayer graphene near the magic angle," *Nature Physics* **15**, 1174 (2019). DOI: 10.1038/s41567-019-0606-5
H.A. assisted with the device fabrication

Arora H.S., Katti R., Saira O-P, Rej E., Watanabe K., Taniguchi T., Roukes M., Nadj-Perge S. "Microwave readout of thermal response in a superconducting graphene circuit." *In preparation*.
H.A. co-designed the experiment. H.A. made the graphene resonator devices. H.A. performed the measurements. H.A. co-analyzed the data. H.A. assisted with the manuscript writing.

Katti R., Arora H.S., Saira O-P, Nadj-Perge S. Schwab K., Roukes M., "Broadband Radiation Sensor based on a resonantly-coupled graphene SNS junction." *Provisional patent*, CIT-8438-P.
H.A. co-designed the experiment. H.A. made the graphene resonator devices. H.A. performed the measurements. H.A. co-analyzed the data. H.A. assisted with the patent writing.

TABLE OF CONTENTS

LIST OF ILLUSTRATIONS

LIST OF TABLES

Chapter 1

INTRODUCTION

Wolfgang Pauli once remarked that "God made the bulk, the surface was invented by the devil". His reasoning for making this statement was driven by the understanding that in the bulk of any material, the constituent atoms face a very different surrounding environment compared to atoms on the surface. Since the surface is directly in contact with the environment, its properties can be very different from the bulk - the energy landscape of the surface doesn't have to match the bulk energy landscape. Therefore, surface properties can be very difficult to control. In addition, when one dimension of the material becomes smaller than the electron wavelength, the degree of freedom enjoyed by electrons is reduced. In such a two-dimensional (2-D) material, quantum effects begin to dominate and can give rise to exotic electronic phases.

One can ask, what happens as you keep on thinning down a material? Can you even reach the limit of single atomic thickness? As it turns out, some materials are easier to thin down (or exfoliate) than others, the most prominent example being graphite which is ubiquitously used in pencils. The 3-D material is comprised of two-dimensional sheets of carbon (i.e. graphene) that are held together by weak van der Waals forces. This class of materials, which have strong forces between atoms of the same layer and weak van der Waals forces between atoms of different layers, are known as **van der Waals (vdW) materials**. Before its isolation in 2004 [1], it was a widely held belief that an atomically thin sheet of carbon would curl up or crumble upon isolation to a single layer. But as it turns out (luckily for us!), graphene was stable enough to be isolated in a monolayer form along with hundreds of other van der Waals materials. One of the biggest concerns about the isolation of graphene was the expectation that the thermal fluctuations (as one approaches the 2D limit) would be big enough to rupture the graphene sheet. While graphene does have weak π bonds that provide delocalized electrons, giving excellent electronic properties and the low energy bandstructure, the strong interatomic σ bonds make it structurally very stable. In fact, it remains defect free upto 500°C in atmosphere [2]. In addition, because it is isolated in a 2-D form from a 3-D crystal, it is believed that graphene is "quenched" into a meta-stable flat state [3].

As we will discuss more in Chapter 2 of this thesis, physicists were fascinated by the electronic properties of graphene due to its "massless" charge carriers. While quantum phenomena like the quantum hall effect usually can only be seen at very low temperatures, graphene's remarkably low scattering and high mobility enabled the observation of the quantum hall effect at room temperature in 2007, three years after its discovery[4]. Apart from its amazing electronic properties, graphene also has extraordinary strength [5]: it is the strongest material know to humans with with an intrinsic tensile strength of 130 GPa (19,000,000 psi) and a Young's modulus (stiffness) of 1 TPa (150,000,000 psi). Lastly, it has exceptionally high thermal conductivity [6, 7], which could have applications in thermal management and heat dissipation in integrated circuit-based electronic systems.

1.1 Emergent phenomena

In the context of materials where electrons begin to interact, the concept of *emergence* is of particular relevance. Emergence as a principle first gained attention in philosophy where [8] in 1846, the British philosopher John Stuart Mill wrote the following about the nature of living organisms:

> All organized bodies are composed of parts, similar to those composing inorganic nature, and which have even themselves existed in an inorganic state; but the phenomena of life, which result from the juxtaposition of those parts in a certain manner, bear no analogy to any of the effects which would be produced by the action of the component substances considered as mere physical agents. To whatever degree we might imagine our knowledge of the properties of the several ingredients of a living body to be extended and perfected, it is certain that no mere summing up of the separate actions of those elements will ever amount to the action of the living body itself. The tongue, for instance, is, like all other parts of the animal frame, composed of gelatine, fibrine, and other products of the chemistry of digestion; but from no knowledge of the properties of those substances could we ever predict that it could taste, unless gelatine or fibrine could themselves taste; for no elementary fact can be in the conclusion which was not in the premises.

In his seminal article "More is Different" [9], P.W. Anderson highlighted the importance of emergence in physics. Complex systems around us are layers upon layers of simple phenomena built upon each other. As physicists, one of the most rewarding

intellectual pursuits is to be able to reduce a complex problem down to simple laws that govern the nature of many things. It is then possible to ask, why do we care about this reductionist approach after all, since we know that the Schrodinger equation lies at the heart of all quantum mechanical phenomena? The words of Wigner and Seitz [10] perfectly answer this question:

> If one had a great calculating machine, one might apply it to the problem of solving the Schrodinger equation for each metal and obtain thereby the interesting physical quantities, such as the cohesive energy, the lattice constant, and similar parameters. It is not clear, however, that a great deal would be gained by this. Presumably the results would agree with the experimentally determined quantities and nothing vastly new would be learned from the calculation. It would be preferable instead to have a vivid picture of the behavior of the wave functions, a simple description of the essence of the factors which determine cohesion and an understanding of the origins of variation in properties from metal to metal.

How is any of this this relevant to vdW materials? Recently, it was shown that under the right conditions, in the case of graphene, the combination of graphene (a metal) and graphene, can give rise to a superconductor, an insulator [11, 12] and a ferromagnet [13]! It would be the equivalent of a stack of paper appearing blue but the individual sheets of paper themselves are red. As a result, understanding the behavior of these 2-D sheets both individually and collectively is a very interesting and challenging problem!

1.2 Novel quantum states of matter in vdW materials

As discussed earlier, understanding how different electronic phases interact with each other has been one of the most exciting problems in condensed matter physics. In this context, van der Waals (vdW) materials offer an interesting prospect to the experimental physicist. In contrast to other methods of creating hetero-structures, van der Waals (vdW) materials are not restricted by constraints such as lattice matching. The flexibility offered in this context is immensely important. For example, it is very easy to integrate graphene (a semi metal) into a vdW heterostructure with a superconductor [14], semiconductors with strong spin-orbit coupling [15], quantum spin hall insulators [16], and ferromagnetic insulators [17].

Topological phase - Quantum Spin Hall state

One of the most famous exotic electronic phases is the Quantum Spin Hall (QSH) state conceived by Eugene Mele and Charlie Kane in 2005 [18]. What is exotic about this phase? When the material is in this phase, electrical currents do not flow uniformly through the sample but only through the edges; additionally, the direction of movement of electrons on the edge is locked to their spin in a way that prevents them from reversing their direction on scattering from a defect or other sources of disorder (also known as "backscattering"). Backscattering electrons dissipate their lost energy in the form of heat - this dissipation is suppressed in QSH insulators. Because of this unique feature, QSH insulators can be promising materials for realizing low energy loss devices. In Chapter 2, we will look into more details on why graphene was expected to exhibit topological characteristics and how people harnessed the power of stacking to try to engineer robust topological states in graphene.

Correlated electronic states: Twistronics

As if this wasn't exciting enough, it was recently discovered that stacking the same 2-D material on top of each other with a small degree of rotation between the two layers (known as twisting) can also lead to correlated insulators, superconductivity, ferromagnetism, orbital magnetism, and Chern insulators! All within the same material system (composed of carbon atoms) accessed by tuning the Fermi level using an electrostatic gate. This was achieved by twisting two sheets of single-layer graphene on top of each other by approximately 1.1°, known as Magic Angle Twisted Bilayer Graphene (MATBG) [11]. More generally, rotating two sheets of graphene by an arbitrary angle results in Twisted Bilayer Graphene (TBG). For lack of a better phrase, TBG took the world of 2-D physics by storm. This led to an explosion of interest in "magic angle" graphene along with twisting and stacking all sorts of 2-D materials [19, 20, 21], giving rise to a new field known as "Twistronics". There have even been reports of observing superconducting states by twisting and stacking two semiconductors [22].

The discovery of superconductivity in TBG itself was truly astonishing, however, what made its existence even more remarkable was the fact that in the initial experiments, the superconducting pocket was always in close proximity to an insulating state (which was dubbed as a "Mott" Insulator). As we will see later in the thesis, this insulating state is not a necessary precondition for observing superconductivity in TBG. While several other interesting phases have been observed in magic angle

graphene, questions about the origins of these states remain unanswered. In this thesis, we will try to rule out certain theories while placing bounds on the other ones.

Engineering states in vdW materials by stacking

Many of the interesting vdW materials shown in Fig. 1.2 are very sensitive to air exposure, especially in the few layer limit where entire flakes can disappear upon exposure to air for a few seconds. Using micromanipulator-based setups inside glovebox(s), it is possible to achieve pristine quality interfaces between dissimilar materials [23, 24]. An example of this is shown in Fig1.1, where we sandwiched few-layer WTe_2 (a Weyl semimetal) between 2 flakes of few layer $NbSe_2$ (a 2D superconductor) in an Argon-filled glovebox (<0.5ppm O_2 and <0.5ppm H_2O). Both of these materials are sensitive to air exposure. Once the air sensitive layers are stacked, we cap them with insulating h-BN to protect them for the device processing steps done outside the glovebox. Despite both of these materials being very air sensitive, by using this method, we managed to induce robust superconductivity in WTe_2. Clean interfaces between superconducting and non-superconducting materials are notoriously difficult to realize, and the quality of the interface determines how strong the induced superconductivity will be in the non-superconducting material. Here, we were able to obtain a very clean interface between the two materials, as evidenced by a zero resistive state in WTe_2 for about 300μA in a few μm^2 junction area.

There are hundreds of known vdW materials and possibly, thousands undiscovered. Fig 1.1 shows just a few of these materials along with some of their interesting properties. It is possible to obtain atomically flat topographies and extremely pristine interfaces between two different vdW materials just by laying them on top of each other. Therefore, two dimensional van der Waals materials offer unlimited possibilities for designing novel nano-devices that study exotic electronic states.

1.3 Towards application-oriented devices

A promising direction towards ultra-sensitive calorimetry and detection of single-microwave photons exploits the temperature rise of absorbers with low heat capacities. Graphene, with its vanishing heat capacity and weak electron-phonon coupling at cryogenic temperatures, is a promising candidate. We therefore perform dispersive thermometry on a graphene Josephson Junction (gJJ) integrated with a resonant circuit. In contrast to other detection methods (ones that involve switching between

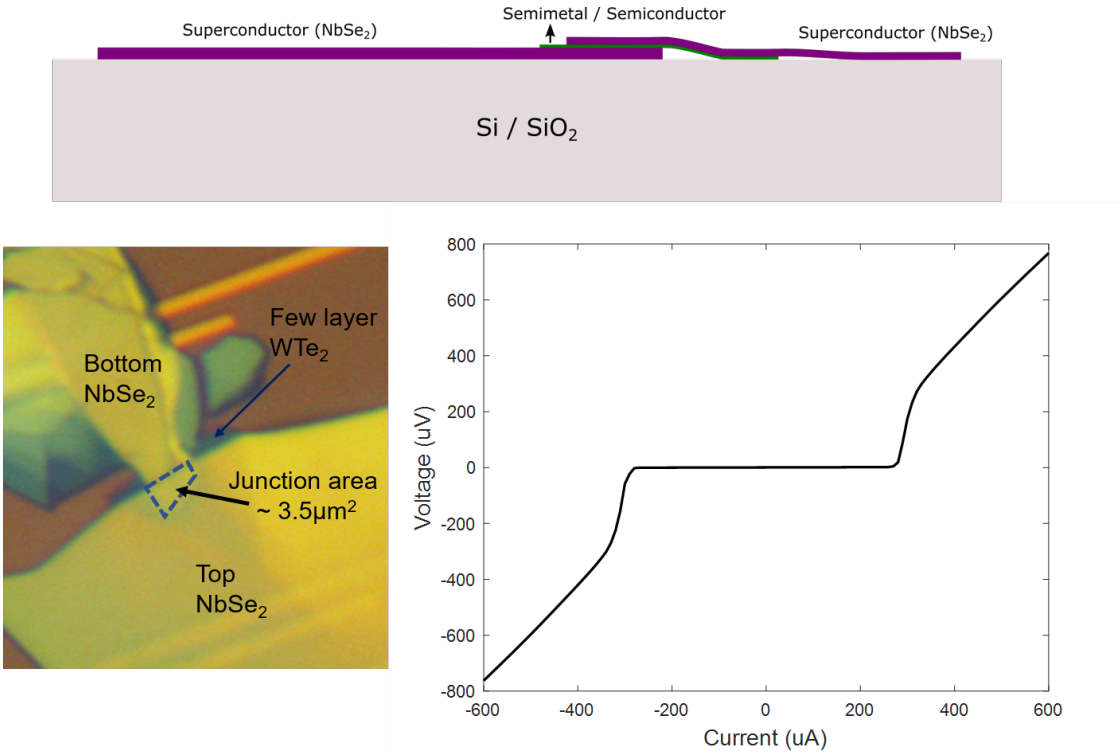

Figure 1.1: A vdW Josephson Junction made from stacking air sensitive materials.

Metal/Semimetal		Semiconductor		Insulator	Superconductor		Ferromagnet / Anti-Ferromagnet	
Graphene	$PtSe_2$	MoS_2	WS_2	h-BN	$NbSe_2$	NbS_2	CrI_3	$CrGeTe_3$
$HfTe_2$	$MoTe_2$ (1T′)	$MoSe_2$	WSe_2	Muscovite	TaS_2	$TaSe_2$	$CrBr_3$	$CrSiTe_3$
$TaTe_2$	$TiSe_2$	Black Phosphorous	InSe	Phlogopite	$NbTe_2$	$ZrTe_3$	$CrCl_3$	VSe_2
$TiTe_2$	AuSe	ReS_2	$ReSe_2$	MnO_2	$PdTe_2$	FeSe	$Pb_3Sn_4FeSb_2S_{14}$	$MnPS_3$
VSe_2	WTe_2	SnS_2	$SnSe_2$	Magic Angle Twisted Bilayer Graphene (MATBG)				$FePS_3$

Unstable in air Partially stable in air Stable in air

Figure 1.2: Family of van der Waals materials.

the superconducting and resistive states), ours allows for fast, continuous readout of electron temperature, paving the way for continuous detection of low-energy photons and phonons. Although we haven't approached the theoretical limit for graphene in our experiment, through better design of the device (minimizing area) and/or using a higher Tc superconductor for proximitizing graphene, or through changing the supporting substrate that minimizes the heat leak through the graphene flake, it is possible to come close to the theoretical detection limit.

1.4 Thesis outline

In Chapter 2, we will go into more detail about the unusual bandstructure of graphene and its implications for electronic transport at low temperatures along with its behavior in high magnetic fields. In addition, we discuss the emergence of interest in twisted bilayer graphene from a theoretical standpoint and the technical advancements that made it possible to make high quality samples with the correct rotation between the two graphene layers.

In Chapter 3, we introduce a new class of devices that build on the established structure of TBG devices. We will demonstrate the presence of superconductivity in these devices in the total absence of insulating states. The robust nature of superconductivity without insulating states in this new class of devices is in essence the central discovery of this work.

Chapter 4 will explore the behavior of WSe_2/TBG under the application of perpendicular magnetic fields. This can provide us insight into how symmetries are broken in TBG through proximity to WSe_2 along with the confirmation of the angle between the TBG layers. We will also discuss the theoretical modeling of the TBG bandstructure in the presence of spin-orbit along with some implications for the superconducting state.

In Chapter 5, we pivot towards an experiment that makes use of graphene's vanishingly small heat capacity and its thermal behavior at low temperatures in ultra-clean devices. We will also talk about why we haven't been able to achieve the desired responsivity in the current device, and how, through better design, we can circumvent the problems faced in the present experiment. Broadly speaking, there are two ways of approaching thermal measurements in graphene, the first is using microwave technology to better understand the fundamental physics of graphene and other 2-D materials with an eye towards applications in sensing. The second is to use 2-D materials like graphene in Josephson Junctions for improving qubit technology. In

this work, we will focus more on the former theme.

Chapter 6 talks about the possible future experiments that build from the work presented here. A wealth of new phenomenology remains to be discovered with graphene-based heterostructures, and we discuss a combination of new techniques and devices architectures to uncover some of this physics.

Finally, the appendices cover some technical details related to device fabrication and measurement setup.

Chapter 2

PHYSICS OF GRAPHENE AND TWISTED BILAYER GRAPHENE (TBG)

In early 2018, a breakthrough was made in the field of condensed matter physics when superconductivity was demonstrated in Twisted Bilayer Graphene (TBG). This discovery has sparked an intense debate among physicists about the origin of this superconductivity and created a buzz in the field that hadn't been seen since the isolation of graphene itself. To understand the reason behind this excitement, it's important to first discuss the physics of graphene, the theoretical predictions regarding the "magic angle" and the technical developments in twistronics that led to this breakthrough.

2.1 Overview of Graphene

The electronic structure of graphene is very peculiar, one big reason why physicists were excited about isolating it. The valence and conduction bands of graphene touch each other at the K and K' points of the Brillouin Zone and follow a linear dispersion for low energies. Even though the tight binding method is very simplistic, it is very effective for graphene's low energy bandstructure. Considering only nearest-neighbouring hopping, the Hamiltonian can be written as:

$$\hat{H} = -t_1 \sum_{<i,j>} (a_i^\dagger b_j + b_i^\dagger a_j) \tag{2.1}$$

where i(j) represent sublattice sites A(B), the operator $a_i^\dagger (a_i)$ creates (annihilates) an electron at the A site whose position is $\mathbf{r}_i$, and similarly for $b_i^\dagger (b_i)$. t_1 is the overlap between neighboring p_z orbitals and the usual value is chosen to be around 3.16 eV. Note, this nearest neighbor hopping occurs between atoms of different sublattices.

Fig. 2.1 displays the wavevectors and the Brillouin zone of graphene.

By replacing j with δ(the nearest neighbour vector), the summation can be re-written as:

$$\sum_{<i,j>} (a_i^\dagger b_j + b_i^\dagger a_j) = \sum_{i\epsilon A} \sum_{\delta} (a_i^\dagger b_{i+\delta} + b_i^\dagger a_{i+\delta}) \tag{2.2}$$

If N is the total number of sites, then we can assume that N/2 is the A sublattice

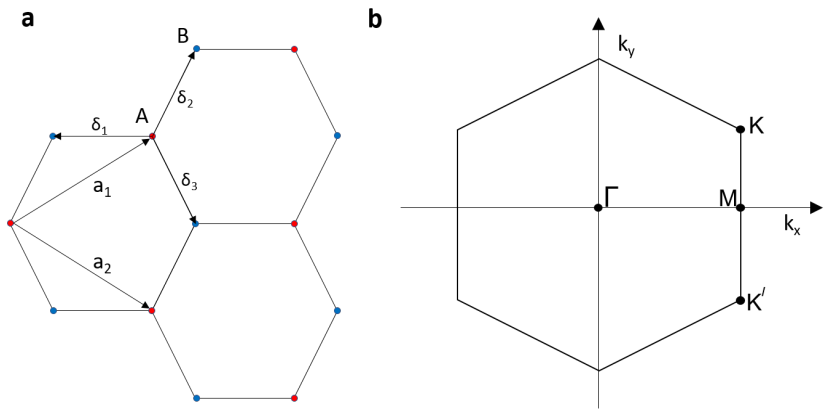

Figure 2.1: **a)** Honeycomb lattice of graphene showing wavevectors and sublattice points, **b)** First Brillouin zone of graphene denoting the K and K' Dirac points.

sites. Therefore, we can replace the creation and annihilation operators with the reciprocal lattice vectors through the following expression

$$a_i^\dagger = \frac{1}{\sqrt{N/2}} \sum_k e^{ik\cdot r_i} a_k^\dagger \tag{2.3}$$

Similarly for $b_{i+\delta}$. The simplified Hamiltonian then becomes

$$H = -t_1 \sum_{\delta,k} (e^{-ik\cdot\delta} a_k^\dagger b_k + e^{ik\cdot\delta} b_k^\dagger a_k) \tag{2.4}$$

To solve for the eigenvalues, the Hamiltonian is expressed as,

$$H = \sum_k \Psi^\dagger f(k) \Psi \tag{2.5}$$

the wavefunctions have the following form

$$\Psi = \begin{pmatrix} a_k \\ b_k \end{pmatrix} \qquad \Psi^\dagger = \begin{pmatrix} a_k^\dagger & b_k^\dagger \end{pmatrix} \tag{2.6}$$

also,

$$f(k) = -t_1 \begin{pmatrix} 0 & \Delta_k \\ \Delta_k^* & 0 \end{pmatrix} \tag{2.7}$$

and

$$\Delta_k = \sum_k e^{ik\cdot\delta} \tag{2.8}$$

Calculating Δ_k for a honeycomb lattice leads to

$$\Delta_k = e^{-ik_x a}[1 + 2e^{i3k_x a/2}\cos\left(k_y a\frac{\sqrt{3}}{2}\right)] \tag{2.9}$$

with eigenvalues of the form

$$\epsilon_\pm = \pm t_1\sqrt{\Delta_k \Delta_k^*} \tag{2.10}$$

More explicitly, the eigenvalues are:

$$\epsilon_\pm(k) = \pm t_1\sqrt{1 + 4\cos\left(\frac{3ak_x}{2}\right)\cos\left(\frac{\sqrt{3}ak_y}{2}\right) + 4\cos^2(\frac{\sqrt{3}ak_y}{2})} \tag{2.11}$$

These eigenvalues are used to model the conduction (π^*) and valence bands (π) as shown in Fig. 2.2

According to the band theory of solids, the effective mass of charge carriers is inversely proportional to the band curvature; therefore, for a linear dispersion like graphene, the effective mass of electrons (and holes) is zero. It also exhibits a very high Fermi velocity of 10^6 m/s, and the electrons (and holes) in graphene can enable the study of "relativistic condensed matter physics", offering an opportunity to observe physics that mimics QED (Quantum Electrodynamics) in table-top experiments.

One of the most beautiful features related to this bandstructure is Klein tunneling in graphene[25, 26]. Klein tunneling is a counter-intuitive relativistic effect in which an incoming electron can transmit perfectly through a potential barrier when the barrier height exceeds the rest energy of the electron (mc^2). Usually, quantum tunneling decays exponentially with increasing barrier height; in the case of Klein tunneling however, the transmission probability depends very weakly on the height of the barrier and approaches perfect transparency for very high barriers. When Klein tunneling occurs in a resonant cavity, such as between two graphene p-n junctions, the back reflection at zero magnetic field acquires a π shift in zero magnetic field, leading to a peculiar Fabry-Perot interference pattern which is shifted by half a period [27]. This clear experimental signature was confirmed in experiments by Young *et al.* and Stander *et al.* [28, 29].

2.2 Topology and topological phases in graphene

Quantum Hall Effect

The Quantum Hall Effect, discovered in 1980 by Klaus von Klitzing, was the first experimental demonstration of a topological phase [30] in condensed matter physics.

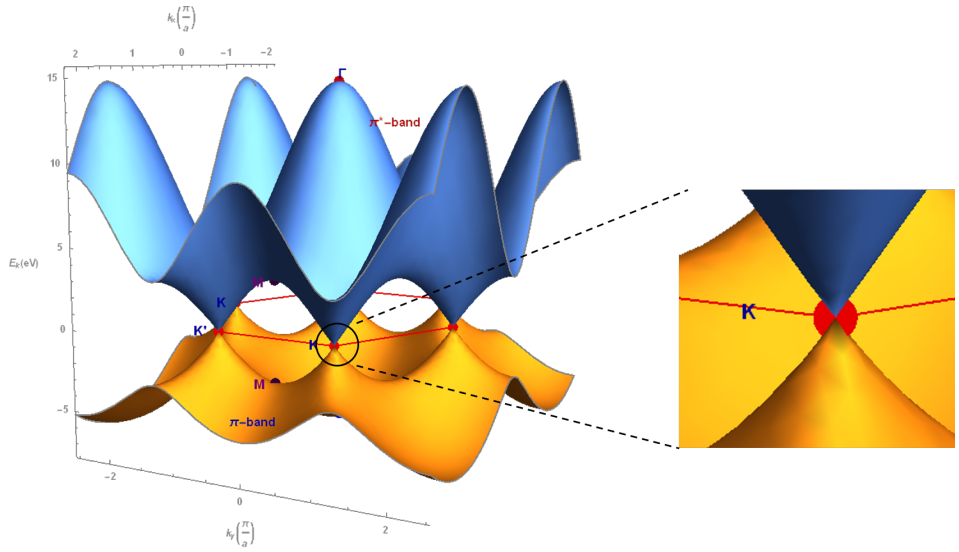

Figure 2.2: Tight binding simulation of the graphene bandstructure: Linear dispersion around K and K' points is clear from the zoom-in.

For classically charged particles, an applied magnetic field causes motion perpendicular to the direction of motion through the Lorentz force. If a current is sourced through in a horizontal direction and a magnetic field is applied perpendicular to the plane of the electron gas, electrons experience a vertical force in addition to the horizontal one, and a voltage can be measured in the vertical direction (Hall voltage also called as "Vxy"). This effect is the classical Hall effect, and the usual setup to measure the Hall voltage (or Hall conductance) is shown in Fig. 2.3. By equating the electric field and the Lorentz force, one can derive the Hall conductance (σ_H)

$$\sigma_H = neB^{-1}$$

where n is the carrier density. So, for the classical case, $\sigma_H \propto n$, which means that the Hall conductance should keep on increasing with an applied magnetic field.

What happens in the quantum case? For the case of a 2-D electronic system, with increasing magnetic field, electrons begin to become more localized and move in "cyclotron orbits" because of the Lorentz force. The cyclotron orbit radius becomes smaller with a larger field. This radius (r_c) is given by $r_c = mv/eB$. The magnetic field strength is B for an electron with velocity v. An electron performing a cyclotron orbit at velocity v has angular momentum $L = mvr_c = eBr_c^2$. Quantum mechanics dictates that the angular momentum of electrons in these orbits must be quantized i.e. $L = n\hbar$ will be allowed. Equating the quantized momentum to the classical

momentum derived using magnetic field, $r_c^2 = n\hbar/eB$, one obtains that only some discrete values are allowed for the radius, $r_n = \sqrt{n} l_B$, where $l_B = \sqrt{\hbar/eB}$ is called the magnetic length.

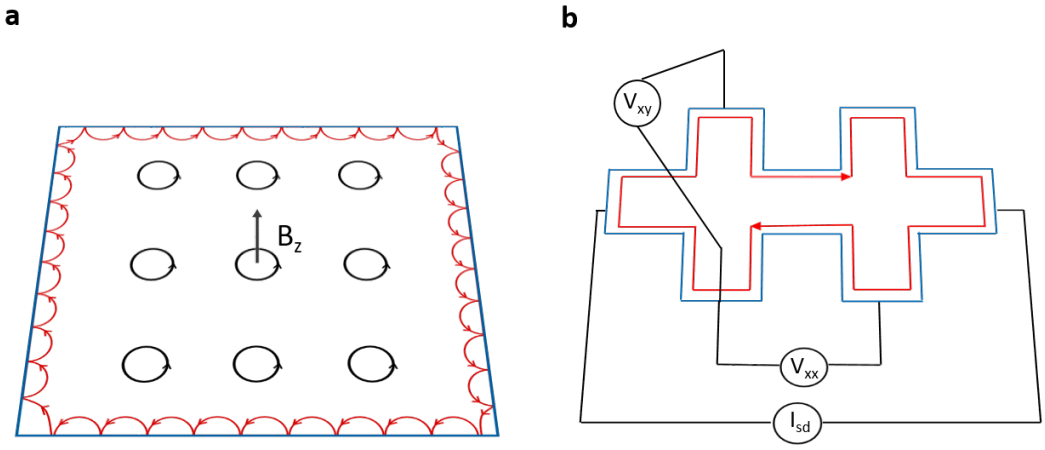

Figure 2.3: **a)** Electrons being localized as a result of perpendicular magnetic field. The edges can still conduct due to skipped orbits at the edges. **b)** Typical setup for measuring transverse (R_{xy}) and longitudinal resistance (R_{xx}).

The frequency of the cyclotron orbits is $\omega_c = eB/m$, which does not depend on the radius. The energy of the electron in this quantized orbit is equal to $L\omega_c = n\hbar\omega_c$. So, the energy spectrum is exactly the same as for a harmonic oscillator. All the energy levels are also shifted up from zero energy by the zero-point motion of the harmonic oscillator, $\hbar\omega_c/2$. We finally obtain the allowed energy levels:

$$E_n = \hbar\omega_c \left(n + \tfrac{1}{2}\right) .$$

These quantized energy levels of electrons in a magnetic field are called "Landau Levels (LLs)". How many electrons can you put in the same Landau level? One for every flux quantum of the magnetic flux passing through the system, so with increasing field, you can squeeze more electrons into the same level. At high enough fields, all the electrons in the sample can be fit into a single Landau level. The degeneracy of Landau levels also scales with the area of the sample.

Now, the electron energies are quantized in Landau levels, and if n Landau levels are filled at a given chemical potential, the filling factor is $\nu = n$. Therefore, adding the conductance from all channels give us the Hall conductance as $\sigma_H = \nu e^2/h = ne^2/h$. The longitudinal conductivity has to be zero because the gapped system does not

allow dissipation of energy in the bulk. How is this related to topology? The fact that the quantized hall resistance is independent of the sample geometry and microscopic characteristics (in fact, it has been measured to a precise value of one part in a billion) is an indication of toplogy being at play where the conductance is immune to local perturbations.

Haldane Model and the Quantum Anomalous Hall (QAH) Effect

By 1987, the integer Quantum Hall Effect was the only topological phase observed, and Duncan Haldane began to wonder if it would be possible to realize topological edge modes that wouldn't require the application of a magnetic field. He came up with a toy model known as the "Haldane model" [31] for a honeycomb lattice (like graphene, although he did not have specifically graphene in mind) that was the first theoretically predicted phase hosting topological modes in zero magnetic field. The Haldane model is the precursor for the Quantum Spin Hall (QSH) Effect developed by Kane and Mele [32, 33]. Quantized edge conductance in the absence of a magnetic field is known as the Quantum Anomalous Hall Effect (QAH) [34].

To make a topological quantum system, one would need to open a gap (in a gapless system), close it, and then reopen it depending on the choice of parameters used. When a system is gapless, the edge modes can become either topological or trivial based on the parameters and this evolution is shown in Fig. 2.4. A trivial way of opening up the gap is to simply break the onsite sublattice symmetry in graphene, for instance by aligning h-BN crystallographic axes with the graphene crystallographic axes.

What happens when you break the sublattice symmetry of graphene by aligning it with h-BN? It becomes energetically most favorable when half the carbon atoms in the graphene sheet are directly above boron atoms, and the centers of graphene's hexagonal structure are directly above the nitrogen atoms [35]. This results in the sublattice becoming corrugated in the z direction and no longer symmetric. How is this z dependence important? Revisiting the tight binding Hamiltonian again, where

$$\Delta_k = \sum_k e^{ik\cdot\delta} = \sum_k [\cos(k\cdot\delta) + i\sin k\cdot\delta] \tag{2.12}$$

$$f(k) = -t\sum_\delta \begin{pmatrix} 0 & \cos(k\cdot\delta) + i\sin(k\cdot\delta) \\ \cos(k\cdot\delta) - i\sin(k\cdot\delta) & 0 \end{pmatrix} \tag{2.13}$$

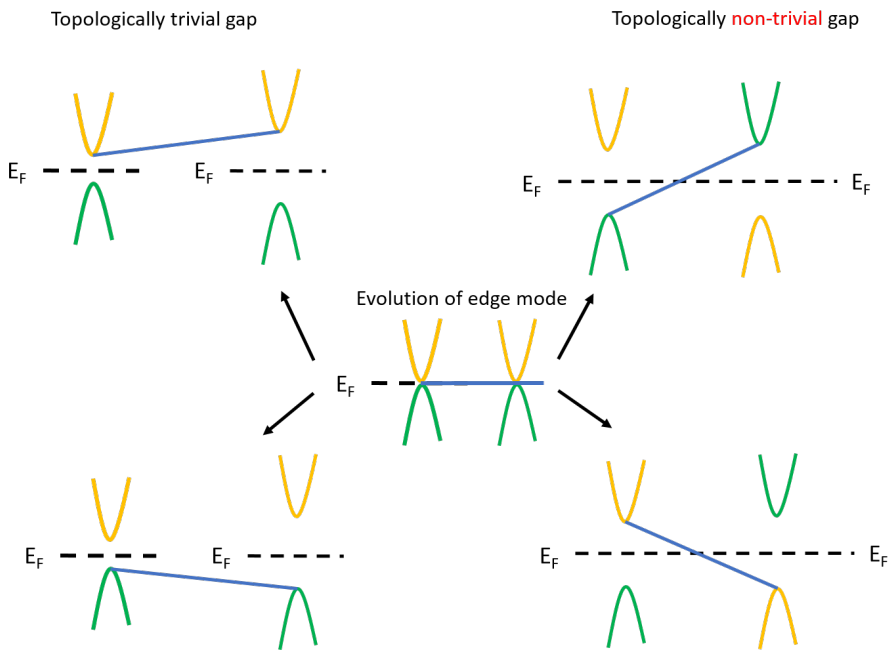

Figure 2.4: When a gap opens up in a honeycomb lattice model like graphene, modes on the edge can connect cones at different valleys in a trivial manner or a topological manner.

and using Pauli matrices

$$f(k) = -t \sum_{\delta} [\cos(k \cdot \delta)\sigma_x - \sin(k \cdot \delta)\sigma_y] \tag{2.14}$$

Adding a z direction term to this

$$f(k) = -t \sum_{\delta} [\cos(k \cdot \delta)\sigma_x - \sin(k \cdot \delta)\sigma_y + g\sigma_z] \tag{2.15}$$

$$f(k) = -t \sum_{\delta} \begin{pmatrix} g & \cos(k \cdot \delta) + i \sin(k \cdot \delta) \\ \cos(k \cdot \delta) - i \sin(k \cdot \delta) & g \end{pmatrix} \tag{2.16}$$

What this does is that it raises the energy of the A sublattice and lowers the energy of the B sublattice and the new eigenvalues are

$$\epsilon_{\pm}(k) = \pm t \sqrt{1 + 4\cos\left(\frac{3ak_x}{2}\right)\cos\left(\frac{\sqrt{3}ak_y}{2}\right) + 4\cos^2\left(\frac{\sqrt{3}ak_y}{2}\right) + g^2} \tag{2.17}$$

The Dirac points therefore become gapped (with a value g) and that has been experimentally observed in both monolayer graphene and TBG [36, 37, 38, 39, 13].

We saw earlier a tight binding description of graphene including the nearest neighbour hopping term. What Haldane realized is that if we include a complex second-nearest neighbor hopping term in addition to the nearest neighbor hopping, the lattice can be made topological as shown in Fig. 2.5.

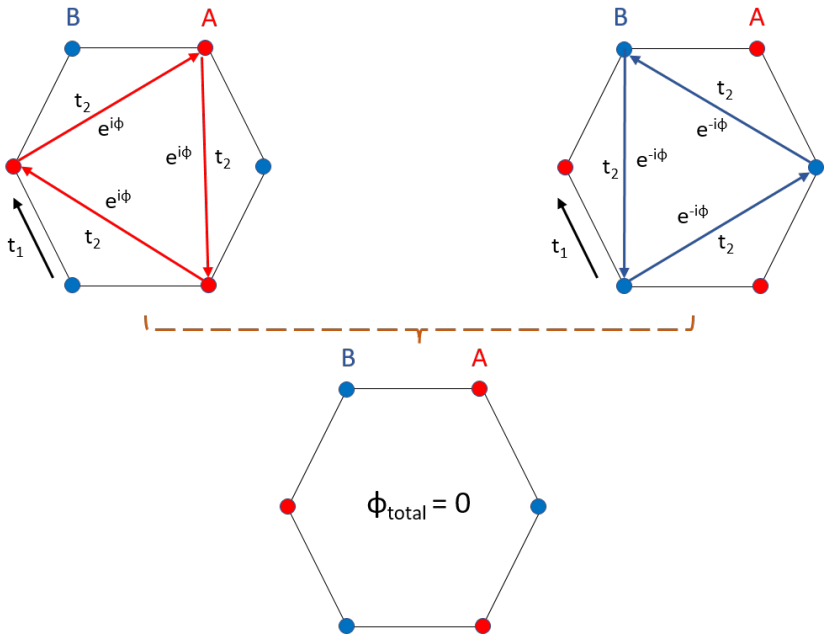

Figure 2.5: Next nearest neighbour hopping introduced by Haldane that considers hopping between atoms of the same sublattice (denoted by t_2).

The Haldane addition to the tight binding Hamiltonian (Eqn. 2.1) (with the next nearest neighbor hopping amplitude given by t_2) is

$$H_{Haldane} = t_2 \sum_{i,j} e^{i\phi_{ij}} a_i^\dagger b_j \tag{2.18}$$

The term $\phi_{i,j}$ is either $+\phi$ or $-\phi$ depending on the direction of hopping (clockwise or anti-clockwise). It is important for this hopping term to be complex to break the time reversal symmetry - if it is complex then the time reversed path will not be equal to the initial path. The Haldane term can be simplified to

$$H_{Haldane}(k, \phi) = 2t_2 \sin\phi[\sin(k \cdot a_1) - \sin(k \cdot a_2) - \sin(k \cdot (a_1 - a_2))]\sigma_z \tag{2.19}$$

where a_1 and a_2 are the lattice vectors of the honeycomb lattice. This can be further simplified for the K and the K' valleys as

$$H_K \approx \frac{-t_1\sqrt{3}}{2}(q_x\sigma_x - q_y\sigma_y) + (m - 3\sqrt{3}t_2 \sin\phi)\sigma_z \tag{2.20}$$

and

$$H_{K'} \approx \frac{-t_1\sqrt{3}}{2}(q_x\sigma_x + q_y\sigma_y) + (m + 3\sqrt{3}t_2 \sin\phi)\sigma_z \tag{2.21}$$

Where m is a mass term that breaks the sublattice symmetry (similar to the breaking discussed earlier). It is important to note that the gap can be closed and opened for several values of the extra parameter m. The phase diagram showing the relationship between this parameter and the topological nature of the gap is shown in Fig. 2.6. This was the first prediction, a topological phase in graphene (although not discovered at that time) without the need for an external magnetic field.

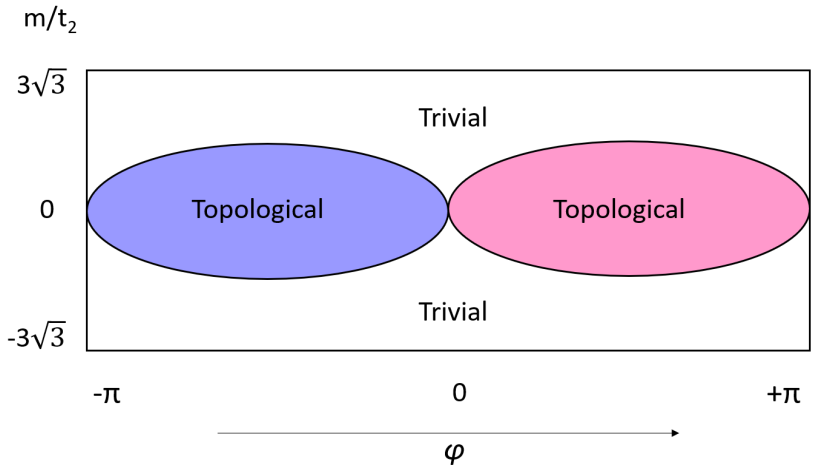

Figure 2.6: Phase diagram for the Haldane model showing the parameter space for which the system becomes topological.

Kane and Mele model - Quantum Spin Hall (QSH) Effect

Kane and Mele took the Haldane model further by removing the requirement of breaking time-reversal symmetry. They realized that if the spin was coupled to the momentum of the electrons, they could get two copies of the Haldane model and make the system topological even though the system remained time-reversal symmetric. When an electric field was applied to such a system, there would be no net Hall current, but there would be a net spin current. The model built up on the Haldane model by adding a spin dependence to the Next Nearest Neighbor (NNN) hopping. The Kane-Mele model used on-site spin orbit coupling in graphene to couple the spin to the hopping in the tight binding model. This opened up a gap at the Dirac point, which was topological as defined by the Z_2 topological invariant. The resulting band structure from their calculations is shown in Fig. 2.7. The chiral

edge states connecting the conduction and valence bands are visible. An excellent treatment of this topic can be found on [40].

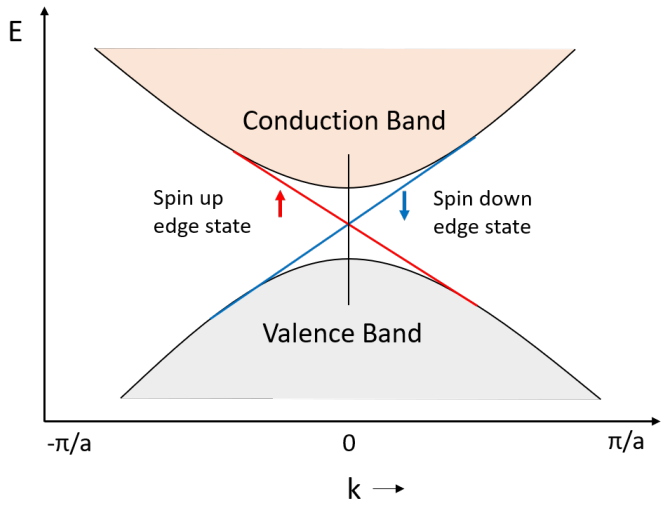

Figure 2.7: Qualitative band structure calculated for graphene within the Kane-Mele model. The chiral edge states connecting the conduction and valence band are visible are visible.

In spite a lot of experimental effort dedicated to observing the QSH Effect in graphene, it continues to remain elusive, with the reason being that the intrinsic spin-orbit coupling in graphene is too weak to effectively open a gap at the Dirac points. The QSH Effect, however, was later predicted and observed in other 2-D systems such as HgTe quantum wells and monolayer WTe_2 [41, 32, 42, 43]. In general, based on experimental observations, the QSH Effect seems to be less robust to microscopic disorder than the Quantum Hall or the Quantum Anomalous Hall and is possibly due to backscattering enhancement caused by magnetic impurities [42].

2.3 Inducing spin-orbit coupling in graphene

After it became clear that the intrinsic spin-orbit coupling in graphene was too weak on its own (to open up a gap large enough to see the QSH effect), physicists started exploring ways to provide spin-orbit coupling to graphene externally in an effort to revive its candidacy for hosting a topological phase. One such method was adatom deposition of heavy atoms on a sheet of graphene [44]. The proposal involved "decorating" an ordinary graphene sheet with a dilute concentration of heavy-element atoms so that graphene would inherit their strong spin-orbit coupling.

Calculations predicted that covering a graphene sheet by a few % of indium or thallium atoms would make graphene exhibit a robust topological Quantum Spin Hall (QSH) phase having gaps detectable in transport measurements. Experimentally however, this didn't work because on deposition, the adatoms would tend to cluster in pockets instead of remaining scattered throughout, which adversely affected the electronic quality of graphene.

The second method which ended up gaining more experimental traction was coupling a graphene sheet to another 2-D material with string intrinsic spin-orbit coupling. The most commonly available materials were the Transition Metal Dichalcogenides such as MoS_2, $MoSe_2$, WS_2, and WSe_2, and the effect of coupling these materials to graphene was investigated by many groups [45, 15, 46, 47]. Generally, WSe_2 was found to be the most effective in inducing the spin-orbit effect in graphene, and the values of measured spin-orbit coupling ranged from 1-10 meV (10-100 times stronger than the intrinsic spin-orbit interaction in graphene). Three different types of spin-orbit coupling are proposed to have been induced in graphene as a result of the proximity effect to TMDCs.

1. Rashba coupling, which is present in 2-D electron gases with structural inversion asymmetry [48];
2. Ising spin-orbit coupling, that couples the spin to the valley;
3. Kane-Mele coupling, which opens a gap at the Dirac point in graphene.

The presence of spin-orbit interaction in graphene is deduced from either Weak Anti-Localization measurements or the Shubnikov-de Haas oscillations that reveal the presence of two fermi surfaces, and details of these measurements will be discussed in Chapter 4. The former method is much more widely used and is an accepted proof. WAL measurements often involve fitting 3-4 parameters to a peak in conductance at zero magnetic field. This fitting procedure usually has a lot of flexibility because of the number of parameters used which results in large discrepancies for the values of spin-orbit coupling quoted. For instance, Wakamura *et al.* report [47] that the main type of spin-orbit coupling observed in their measurements was the Kane-Mele term, whereas in the work of Wang *et al.* [49], the dominant spin-orbit interaction was the Rashba one. What is consistent however in all the measurements, is that the overall spin-orbit strength measured in these devices, regardless of the type, is strong!

2.4 Search for superconductivity in single-layer graphene

Soon after the discovery of graphene, many people began speculating if graphene could support a superconducting state and if so, whether it would be a highly unconventional mechanism. It showed promise by being able to carry supercurrents in both hole and electron doped regimes by proximity to aluminum [50]. The observation of superconductivity in bulk graphite intercalated with alkali metal adatoms provided more lift to the hope of seeing superconductivity in graphene [51, 52].

One should look at the McMillan formula [53] to extract a superconducting transition temperature within the BCS theory,

$$T_c \propto \theta_D e^{-2/(\lambda_0 D(\epsilon))} \tag{2.22}$$

where θ_{D} is the Debye temperature, λ_0 is the electron-phonon coupling potential and $D(\epsilon)$ is the Density of States (DOS) as function of energy [53]. In spite of the Debye temperature being very high (over 2200K), the transition temperature is severely limited by the low density of states in graphene at the Dirac point. It therefore became clear that it would be challenging to observe phonon-driven superconductivity in pristine graphene without substantially increasing the DOS.

Two landmark theoretical studies [54, 55] proposed two different methods to boost superconductivity in graphene. The first approach focused on conventional (BCS) superconductivity and the means by which it could be achieved in graphene. Since phonons play a pivotal role in the BCS theory, it was important for graphene to have strong electron-phonon coupling. However, because the in-plane vibrations are very strong in graphene, it significantly reduces the electron-phonon coupling, thereby reducing a possible superconducting transition temperature to experimentally undetectable levels. In analogy to the bulk graphite superconductivity, Profeta *et al.* [54] studied Cooper pairs in graphene under the Eliashberg theory of phonon mediated superconductivity and suggested decorating the graphene sheet with lithium adatoms. According to their calculations, this would more effectively couple the soft, out-of-plane phonon modes and the vibrations in lithium surface atoms with the π electrons in the graphene sheet. As a result, Cooper pair formation would become favorable, and calculations indicated a transition temperature as high as 8K in LiC_6 and 18K in Li_2C_6.

The second approach relied on boosting electron pairing in graphene through a more unconventional mechanism i.e. through electron-electron interaction. Nandkishore

et al. [55] studied the behavior of electron-electron interaction in graphene at extremely high carrier densities (10^{13}/cm^{-2}) - carrier densities where the Fermi level would approach the saddle points (van Hove singularities in density of states) of the π^* bands shown in Fig. 2.2. Upon inducing electron-electron interactions under these conditions, it appeared that a single particle degenerate electron system was an unstable state. To figure out what the appropriate ground state should be, the authors used a renormalization-group approach to remove any implicit bias that calculations could have towards finding the ground states [56]. Surprisingly, a superconducting state was the most favored ground state akin to the case of La_2CuO_4 proposed by Dzyaloshinskii [57]. More excitingly, this superconductivity had d-wave pairing along with chiral Andreev states running along the edge of the sample. Naturally, experimentalists pursued this idea with a lot of enthusiasm.

Three years after the theoretical prediction, four groups reported observations of superconductivity within 4 days of each other through different measurements. Through lithium decoration of graphene in ultra-high vacuum, Ludbrook *et al.* [58] showed signatures of a superconducting gap (0.9 eV) in ARPES (Angle Resolved Photo Emission Spectroscopy) measurements. Tiwari *et al.* used the Meisnner effect to show a superconducting transition temperature of about 7K in Li intercalated flakes of multilayer graphene[59]. Chapman *et al.* isloated single-layer graphene, decorated it with calcium, and assembled it back together to report a superconducting T_c of 6K [60]. Finally, Ichinokura *et al.* got as close to monolayer graphene in electronic transport as possible by showing superconductivity in bilayer graphene intercalated with calcium atoms below 2K [61]. Because none of these claims have been able to demonstrate magnetic field dependence and zero resistance of the superconducting state for the case of monolayer graphene, they are still under scrutiny in the field [62].

Reaching high enough carrier densities as needed by the proposal in [55], required use of special gating techniques beyond the usual dielectrics. A normal h-BN or SiO_2 gate would break down on applying gate voltages commensurate with extremely high carrier densities. To solve this, Efetov *et al.* [63] used ionic liquid gating where mobile ions can be frozen in a polymer (typically below 250K). Upon applying a positive(negative) voltage to the top of the polymer, negative(positive) ions accumulate near the gate electrode and positive(negative) ions accumulate very close to the surface of graphene. As a result, it becomes possible to move the Fermi level substantially. However, even at carrier densities of 10^{14}/cm^{-2}, graphene

remained metallic down to milliKelvin temperatures [63]. This method however, has been used successfully in another 2-D material (MoS_2) to observe superconductivity [64].

Despite a lot of effort, observation of intrinsic superconductivity in graphene remains elusive. Against this backdrop, we will see why superconductivity in TBG quickly became one of the most exciting topics in condensed matter physics.

2.5 Periodic potentials in twisted bilayer graphene

As mentioned in the first chapter, different vdW materials can be stacked together without any specific thermodynamic constraints. One can also stack the same material on top of each other. An important role then is also played by the relative rotation. Using two sheets of materials with similar lattice constants, one can obtain a so-called "moiré" superlattice whose lattice constant depends on the relative rotation of the two sheets. If the lattice constants are the same (i.e. same material), then the superlattice can theoretically be made infinitely large. The dependence of the moiré wavelength on the relative rotation angle (for a heterostructure of a graphene sheet and a material with a lattice constant mismatch of δ) is shown in Eq. 2.5 where a is the lattice constant of graphene and ϕ is the relative rotation [65].

$$\lambda = \frac{(1+\delta)a}{\sqrt{2(1+\delta)(1-\cos\phi)+\delta^2}} \tag{2.23}$$

Twisted bilayer graphene became a subject of theoretical and experimental study soon after the isolation of graphene [66, 67, 68] as a system with two graphene layers that could be independently controlled. Because the low energy physics of graphene is dictated by non-zero K vectors, a large relative twist between two graphene results in two independent Fermi surfaces in the two layers without any significant overlap. Therefore, one obtains twice as many independent Dirac cones as single-layer graphene that preserve linear dispersion. This fact was used to simultaneously realize two Quantum Hall states with opposite chiralities. Quantum Hall states with opposing charge carriers but with similar level doping will have opposite chiralities (analagous to the Quantum Spin Hall effect but in the presence of magnetic field). Two single graphene layers with decoupled band structures but within the same heterostructure provide this necessary feature of coexisting electron-like and hole-like bands [69, 70].

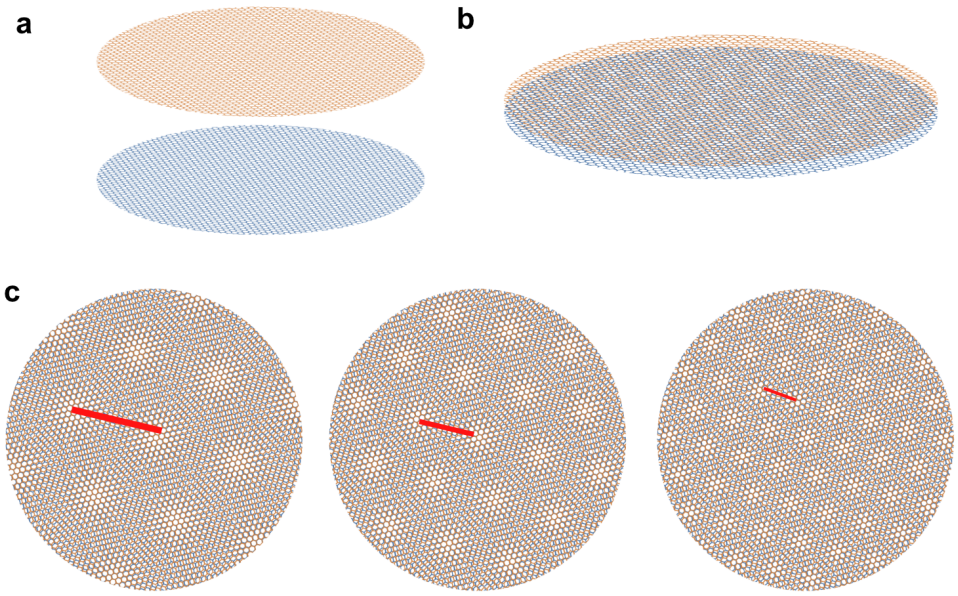

Figure 2.8: **a**), two sheets of graphene far apart. **b**), sheets of graphene in contact at arbitrary rotation angle. **c**), "Twisted Bilayer Graphene" with different rotation angles - difference in moiré wavelength are pointed out by red lines.

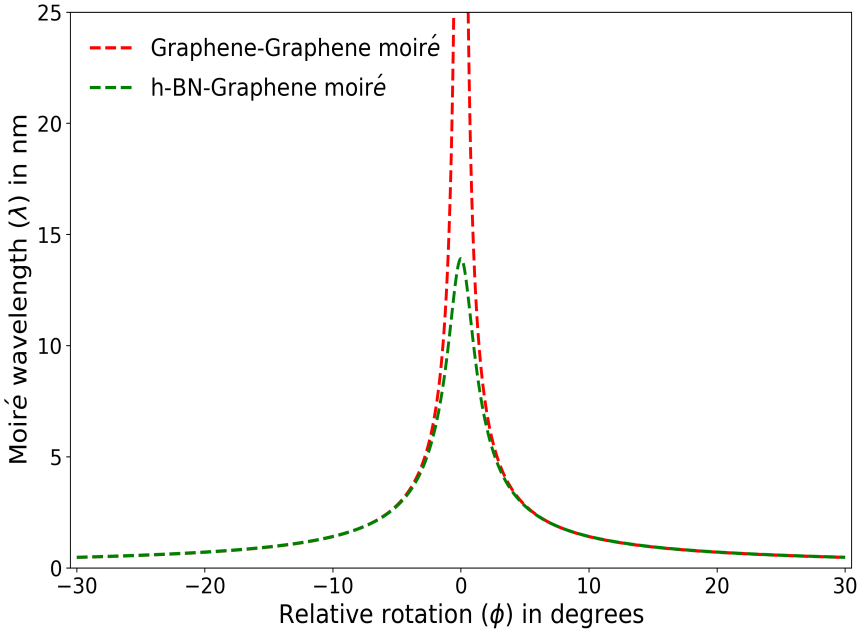

Figure 2.9: Moiré wavelength calculated from Eq. 2.5 for Gr-Gr and h-BN-Gr superlattices. Around zero angle mismatch, the Gr-Gr moiré wavelength diverges.

2.6 Low angle twisted bilayer graphene

What happens to the electronic bandstructure at lower angles with twisting? As you decrease the rotation angle, the interlayer coupling becomes stronger, leading to hybridization of the Dirac cones and a reduction in the Fermi velocity. As neighboring K points in the brillouin zones of the two layers begin to hybridize, the low energy linear dispersion of graphene begins to "flatten out". This flattening of the dispersion leads to a large increase in the corresponding density of states (DOS). A schematic is shown in Fig. 2.10. Since the superlattice edges are around 13 nm for the case of magic angle TBG vs the lattice constant of 0.246 nm for single layer graphene, the superlattice reciprocal wavevector is correspondingly a lot smaller.

In this two-layer system, because of the small twist, there are locations where the carbon atoms from the two layers are directly on top of each other, known as "AA" sites, and locations where carbon atoms have no overlap known as "AB" sites. The "AA" sites of two different moiré unit cells are connected by domain boundaries separating "AB" and "BA" regions. The electrons in this moiré unit cell prefer to localize on these "AA" sites. STM data from our lab [71] clearly demonstrated this localization in real space, as shown in Fig. 2.11.

An influential theoretical study in 2011 by Bistritzer and Macdonald [72] predicted that the Fermi velocity of twisted bilayer graphene would be slowed down significantly for several "magic angle" values - namely $\theta \approx 1.1°$, $0.5°$, $0.35°$, $0.24°$, and $0.2°$. The first of these angles later became know as the "magic angle". This calculation was made possible by making a simplifying assumption that the interlayer tunneling in TBG would be dictated only by the moiré unit cell (as a function of twist angle) and not by the (thousands of) individual constituent atoms. While usually there is a significant barrier for electrons in one layer to tunnel through to to the other layer and vice versa, Bistritzer and Macdonald calculated that for these special angles, the barrier would become exactly zero. As a result of this drastic increase in interlayer tunneling, the electrons in the same layer would slow down and begin interacting with each other. Their bandstructure calculations also predicted the emergence of "flat bands" which were low energy bands with almost no dispersion. When electrons begin to interact in these flat bands, interesting things begin to happen such as the rise of insulating states even in a largely metallic system. An illustration of this is shown in Fig. 2.12. Nobody however, dared to predict the emergence of superconductivity at the "magic angle". Bistritzer and MacDonald also calculated bandstructures for a few twist angles that showed a significant en-

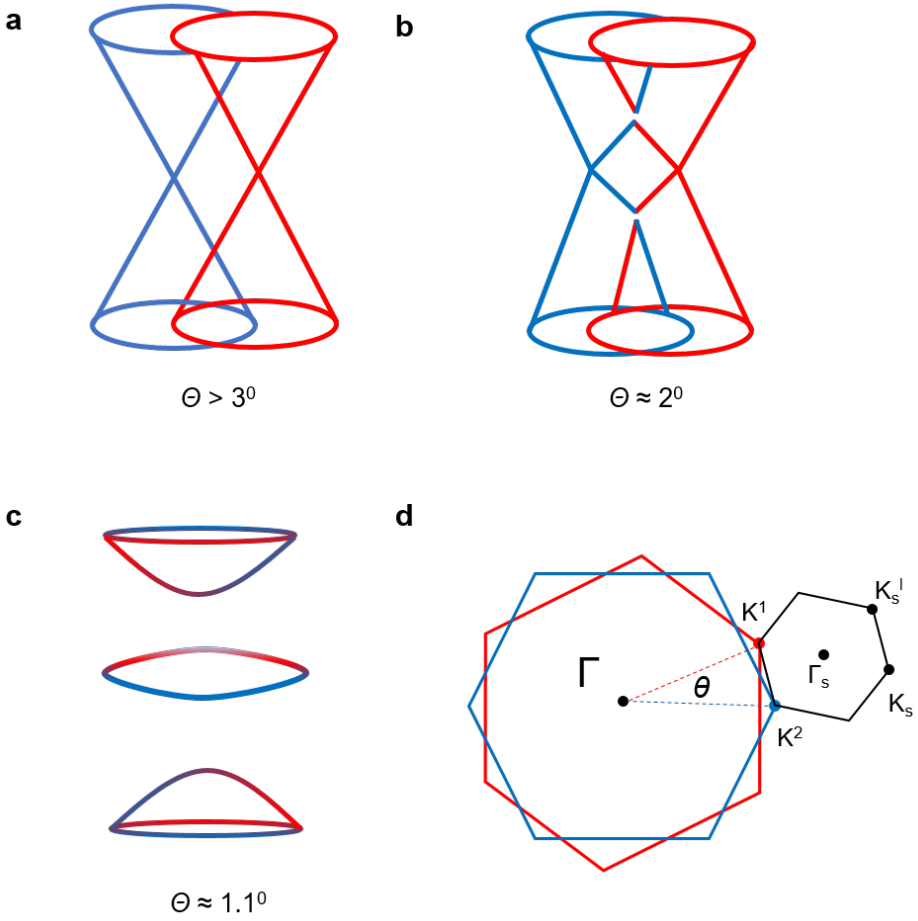

Figure 2.10: Schematic of Dirac cone hybridization in TBG with angle. **a)** The two monolayers are decoupled for large angles. **b)**, The two Dirac cones begin to hybridize around 2°. **c)** Around the magic angle, the interactions are maximized and "flat band" emerge. The density of states in these "flat bands" is extremely high. **d)** Reciprocal lattice behavior for two layers twisted below 2°. The superlattice brillouin zone is shown in black and is much smaller than the original brillouin zones.

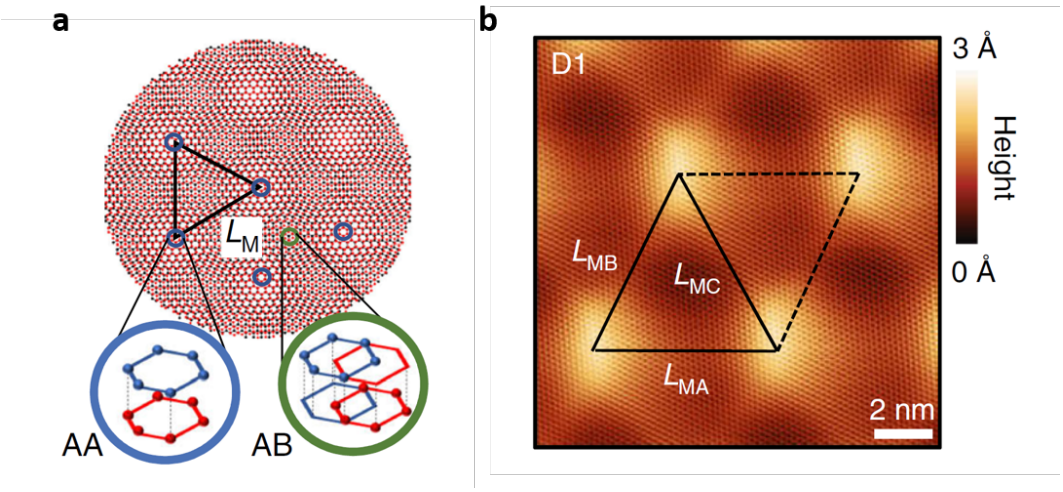

Figure 2.11: **a)** Determining the moiré wavelength - positions of individual carbon atoms are shown for "AA" and "AB" sites, **b)** Surface topography of TBG captured by an STM for twist angle of 1.92°, the AA(AB) sites appear to have increased(decreased) height because of increased(decreased) density of states. Images taken from our work in *Nature Physics* [71].

hancement in the DOS around the "first magic angle". Continuum model based calculation results performed for our devices and the associated band structures along with the details of the theoretical model will be discussed in Chapter 3.

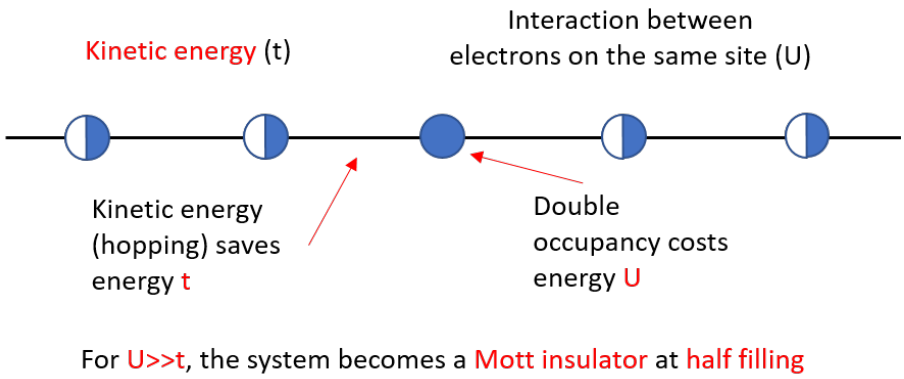

Figure 2.12: Tradeoff between Coulomb energy and Kinetic energy.

Another more conceptual (and less quantitative) way to think about the moiré wavelength (and therefore the angle) required to engineer strong correlations in a 2-D conductor is to think in terms of the bandwidth and Coulomb energy. For strong correlations, we want the coulomb energy U> kinetic energy of electron

bands t since,

$$U \propto \frac{e^2}{\epsilon L} \tag{2.24}$$

and

$$t \propto \frac{\hbar^2 k^2}{2m_e} \propto \frac{1}{m_e L^2} \tag{2.25}$$

where L is the lattice constant for a 2-D lattice. Therefore

$$\frac{U}{t} \propto m_e \cdot L \tag{2.26}$$

which means for $U/t \approx 1$,

$$m_e = 1 \cdot m_0 \longrightarrow L = 1nm$$
$$and \qquad m_e = 0.1 \cdot m_0 \longrightarrow L = 10nm.$$

Because the effective mass in graphene is so low, it seems reasonable to expect that a moiré wavelength of the order of 10s of nm would be necessary to observe the effects of strong correlations in TBG.

2.7 Tear and Stack method

To test out the predictions by Bistritzer and MacDonald, one would need to make a device with two sheets of graphene stacked on top of each other rotated by exactly 1.1°. This was very challenging to do experimentally, because one would require two different flakes of graphene with very well defined axis. Moreover, the edges of graphene come in two varieties (i.e. zigzag and armchair), making the task of making a device with an exact rotation of angle of 1.1° nearly impossible. A breakthrough came in late 2015 when an ingenious method of fabricating precisely controlled twisted bilayer graphene was invented [73, 74]. Though the details of this method can be found in these publications (see Appendix for a schematic of the modified version of this method), we will briefly summarize the key aspects. Here, instead of trying to find two different graphene flakes with well defined edges, you would start with one big graphene flake (the nature of its edges doesn't matter). Then, an h-BN flake is brought into contact with part of the graphene flake. Upon lifting up, the original graphene flake is "torn" and the part that was underneath the h-BN flake is picked up with the h-BN. This method utilizes the strong vdW forces between graphene and h-BN. We fabricated several of these devices in our lab and Fig. 2.13 displays images from the fabrication process of a representative device.

The initial papers that used this method [75, 74] reported for the first time, observations of single particle gaps opening up in low twist angle (<3°) TBG devices in contrast to previous studies [76, 77] where TBG was placed on SiO_2 with presumably the high charge disorder in SiO_2 obscuring the visibility of these gaps. These gaps separated the low energy flat bands from the higher energy dispersive bands with energy gaps ranging from 10-50 meV. This enabled the study of the flat band behavior done later, leading to the observation of superconductivity. Interestingly, the gaps observed experimentally are considerably larger than the ones predicted by theory and have not been reconciled yet.

2.8 Correlated Insulators and Superconductivity in Magic Angle Twisted Bilayer Graphene

After Cao *et al.* [74] and Kim *et al.* [75] showed the existence of low energy bands separated from high energy dispersive bands by large energy gaps (also known as *full filling gaps*) in low angle twisted bilayer graphene, Cao *et al.* began working on fabricating devices close to the magic angle (1.1°). They first discovered insulating states at half filling of the flat bands in addition to the previously observed full filling gaps. These half filling insulating states were attributed to electronic correlations at the magic angle, similar to Mott insulators. Near the half filling, unexpected jumps in conductance were also observed. Because these initial devices had only two contacts, it was hard to understand these jumps fully. However, upon fabricating devices that enabled a 4-point measurement, it became clear that these jumps were actually caused by superconductivity! What was more surprising was how closely spaced the superconducting and insulating phases were, akin to the phase diagram of high T_c superconductors. This observation led to an avalanche of research papers attempting to describe the origin of this superconductivity.

Superconductivity in TBG happens at astonishingly low electron(hole) densities of about $2x10^{12}/cm^{-2}$, an order of magnitude lower than $LaAlO_3/SrTiO_3$ interfaces and doped MoS_2, which themselves are orders of magnitude lower than other superconductors in terms of charge densities. To paint this picture in more concrete terms, superconductivity arises in TBG for 1 electron(hole)/100,000 carbon atoms - that's almost an unbelievable number.

Yankowitz *et al.* used pressure as a knob to change the conditions of the magic angle. For angles greater than 1.1°, the interlayer tunneling in TBG diminishes with increasing angle. On applying pressure, the separation between the two graphene

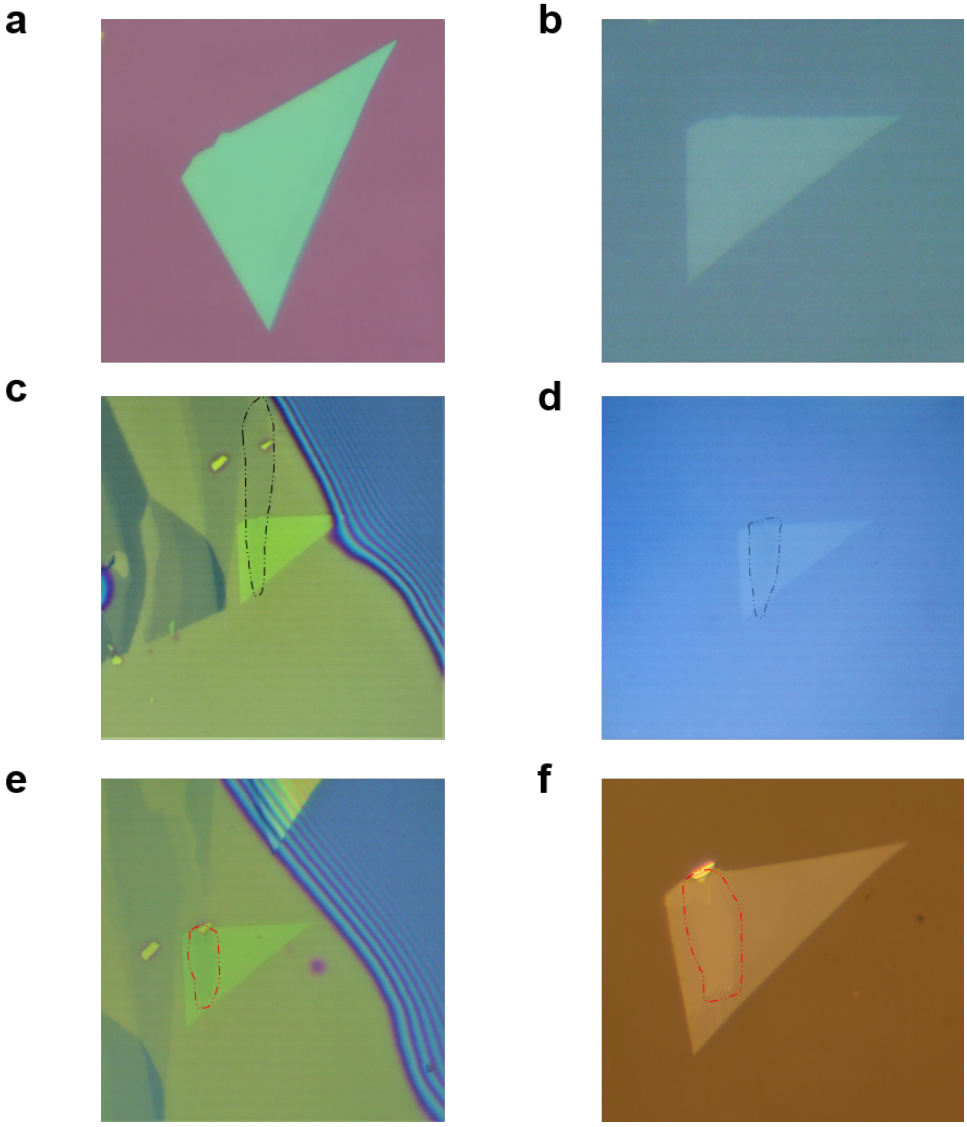

Figure 2.13: Images displaying different steps in making low angle TBG stack. **a)** h-BN flake on SiO_2 that will be on top of the TBG stack. **b)** h-BN flaked picked up PC (polymer used for assembly). **c)** h-BN flake approaching a big graphene flake (dashed black line). **d)** part of the graphene flake is torn and picked up by h-BN upon withdrawal. **e)** After rotating the stage by approximately 1.1°, remaining part of graphene flake is approached by h-BN/graphene. **f)** TBG (outlined by dashed red line) is picked by h-BN.

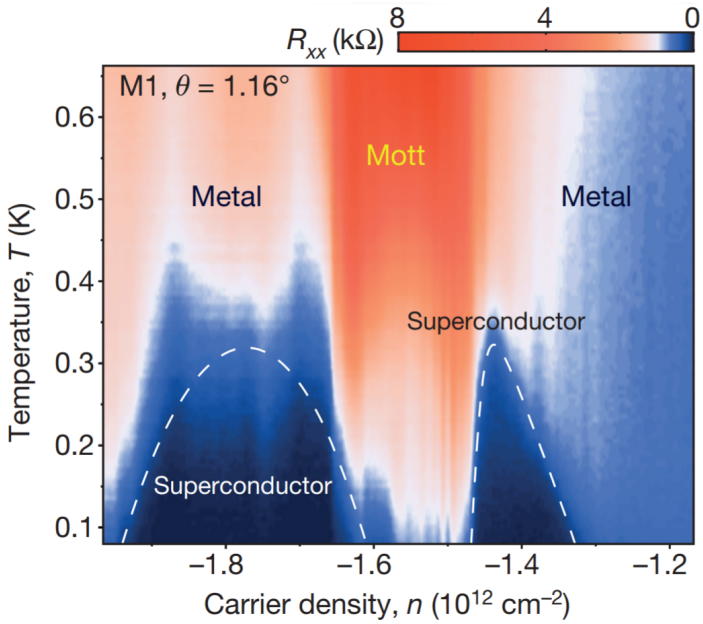

Figure 2.14: Unconventional Superconductivity in MATBG. Taken from [11], reprinted with permission from the copyright holder, Springer Nature.

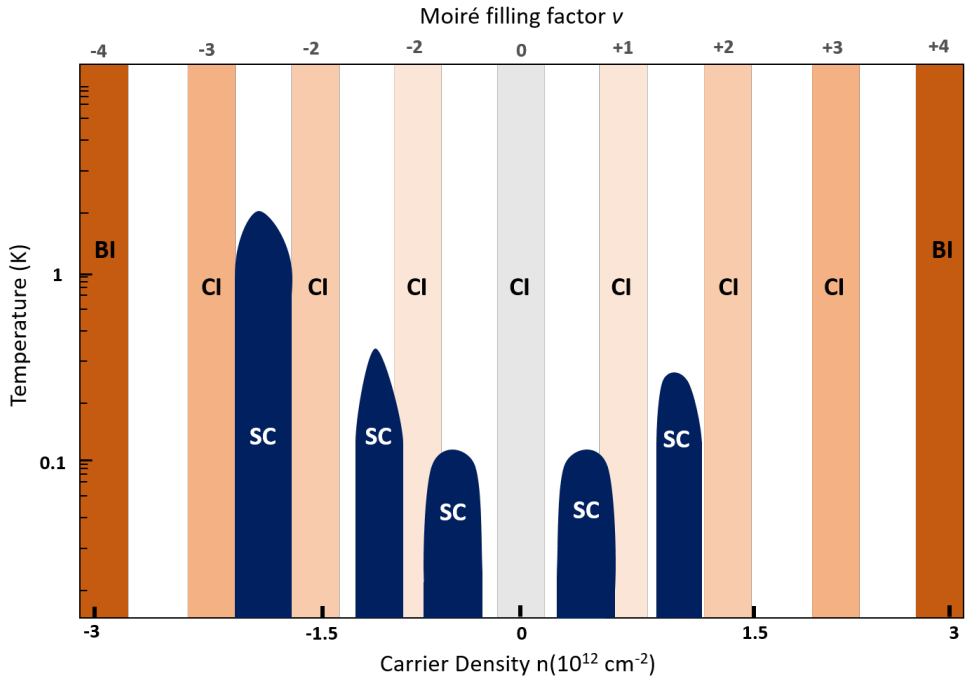

Figure 2.15: Cascade of insulators and superconductors in MATBG. Correlated insulators (CIs) are present for integer filling factors of the moiré unit cell and superconducting pockets. Similar to [79].

sheets decreases and interlayer tunneling increases. Using this fact, a TBG device (at 1.27°) that was neither superconducting nor showed correlated insulating states was made superconducting by the application of a few GPa of pressure.

A few months later, measurements done by Lu *et al.* [78] showed the emergence of several superconducting pockets in TBG along with many correlated insulators at integer filling factors, and one scenario that began to crystallize is shown in Fig. 2.15. Speculation was rife that the ground state of MATBG was superconductivity which was interrupted by correlated insulators [79]. The proximity of the superconducting pockets to the insulating states was analogous to Cuprates leading people to believe that the mechanism of superconductivity in TBG could be similar. So the biggest question became, were superconductivity and insulating phases competing against each other, or were they assisting each other? If they were competing, the mechanism for superconductivity could be phonon-driven, whereas in the assisting picture, the superconductivity was more exotic and thus could help unlock the secrets of high T_c superconductors.

2.9 Low control of twist angle

Initially, we began making regular TBG devices, without any special modifications to the process of making TBG stacks. Soon, we discovered that it was very difficult to control the twist angle that we ended up with in our devices despite being able to stack with a high precision of 0.01°. There was no correlation between the angle obtained and the twist angle that was aimed. This could be attributed to several possible effects [80] including:

1. Random jumping of the graphene when hBN approaches it during stacking.
2. Graphene can be strained during the fabrication process which can change the moiré wavelength of the resulting superlattice.
3. Graphene can slip on h-BN, and it is well known that the interface between h-BN and graphene has a very low friction coefficient. Even minor movement of graphene can result in a substantial change of the twist angle.
4. or Another microscopic mechanism that hasn't been observed yet.

Additionally, the behavior of TBG at room temperature indicates very little about what the twist angle of the device actually is and requires a full cool down of every fabricated device. We fabricated one device with a graphite bottom gate with a high

twist angle homogeneity, shown in Fig. 2.16 (twist angle of $\approx 0.945°$ assigning of the twist angle will be discussed in detail in Chapter 4). While the correlated insulating states can be seen clearly, superconductivity is notably absent at these small angles.

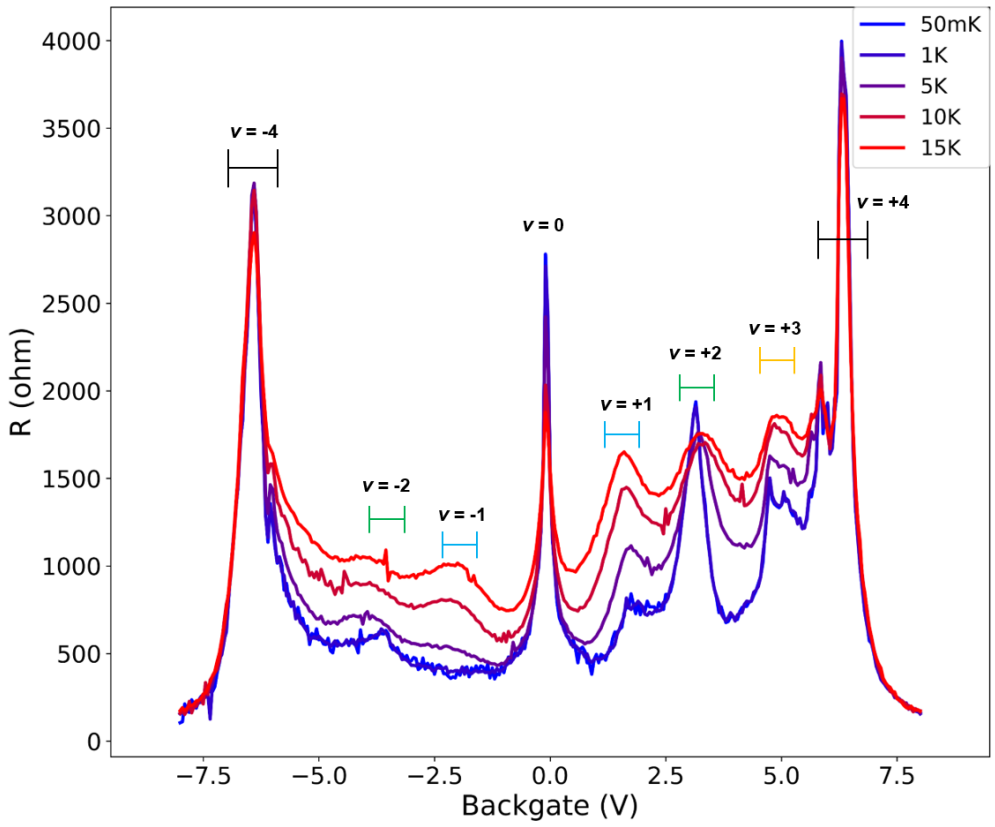

Figure 2.16: Temperature dependence of a TBG device with an angle $\approx 0.945°$. Assigning of the twist angle will be discussed in detail in Chapter 4. The device did not exhibit any signs of superconductivity but showed clear insulating states developing for partial filling of the flat bands which are shown for ±4, +3 ,±2, and ±1 along with the charge neutrality point (+0). The full filling resistance peak (±4) can be split into multiple peaks often, making the determination of twist angle more complicated.

2.10 Effect of encapsulating substrate

The TBG samples exhibiting superconductivity, were all made by encapsulation in hexagonal Boron Nitride (h-BN). Since h-BN is chemically very inert and doesn't

exhibit any exotic electronic phases on its own, one would not expect the substrate to play a big part in the physics of TBG. Traditionally, h-BN has acted as a substrate that reduced electronic disorder by reducing charge puddles and providing an atomically flat surface to support graphene. The first papers that reported superconductivity in TBG did not discuss the effects of the h-BN substrate on the electronic correlations or the observed phenomena. However, there is a quality to h-BN that separates it form being a just another insulating substrate for graphene. h-BN is a 2-D honeycomb lattice with a lattice constant remarkably close to that of graphene. When the two layers are aligned exactly, it is possible to achieve a moiré wavelength of 14nm (very similar to Magic angle physics moiré wavelength) and break the sublattice symmetry of the resulting hetero-structure (A/B atoms of h-BN are different). h-BN aligned with graphene can therefore provide a periodic potential of the order of the moire wavelength in magic angle twisted bilayer graphene, Fig. 2.9 shows this dependence as a function of twist angle. This can have drastic effects on the band structure of twisted bilayer graphene, and we will discuss a back of the envelope calculation of this effect in the next section.

Ferromagnetism in TBG

A year after the discovery of superconductivity in TBG, Sharpe *etal*. [13] discovered to much amazement - that when one of the graphene layers of MATBG is aligned with the (top or bottom) encapsulating h-BN layers, the system becomes a ferromagnet. This system is not just a regular ferromagnet - it is an orbital ferromagnet. Because carbon atoms in TBG have no intrinsic spin alignment, the system had to be an orbital ferromagnet (which is also strange, given the weak spin-orbit coupling in graphene) and is the first known material to be a purely orbital ferromagnet.

Chern insulators

In mathematics, two objects are considered topologically equivalent if they can be transformed into each other by a continuous deformation, stretching, or twisting, but no tearing. A ball and a plate can be considered topologically equivalent but a ball and donut are topologically non-equivalent because of the hole in the donut. The number of holes in an object determines its topological class. In condensed matter physics, the translation is that two quantum systems are topologically equivalent, if their Hamiltonians can be continuously deformed into each other without ever closing energy gaps. We also define something known as the "Chern number" in condensed matter physics that is the equivalent to the number of holes in mathemat-

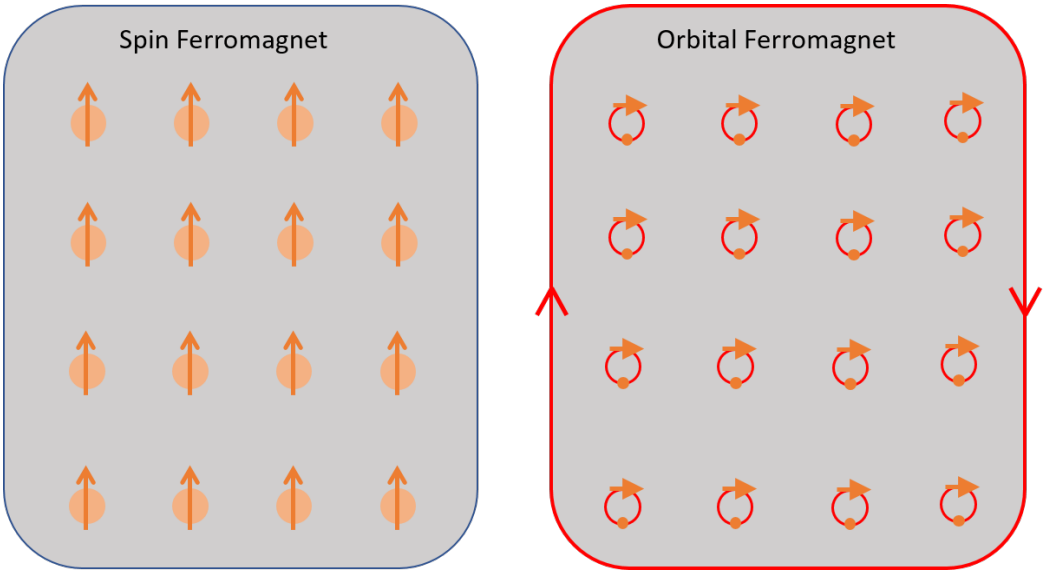

Figure 2.17: Two types of bulk ferromagnetism usually observed. Orbital magnetism is a stronger contributor in materials with a large spin-orbit coupling. Twisted Bilayer Graphene is a purely orbital ferromagnet without significantly strong spin-orbit coupling.

ical topology. Vacuum is designated to have a Chern number of 0. Any insulator with a non-zero Chern number is called a topological insulator and there many ways to calculate the topological invariant [81]. In Fig. 2.18, we discuss what happens on connecting two insulators. A trivial insulator connected to a trivial insulator doesn't result in anything special. However, when a topologically trivial insulator (denoted by 0) comes into contact with a topologically non-trivial insulator (denoted by 1), a conducting mode appears at the boundary between the two insulators that is protected by topological considerations, and hence its conductance is insensitive to the device geometry and immune to perturbations.

Chern Insulators and Twistronics

TBG also provides a playground for exploring topological phases. The first clue to the unusual nature of ferromagnetism in TBG was provided by the extremely large Hall signal (10s of kΩs) at zero magnetic field when the system is in an insulating phase (at filling factor of +3 or filling +3/4). This indicated that even though the bulk was insulating, the edges were somehow conducting. Secondly, non-local measurements strongly suggested the presence of conducting edge modes. It also became apparent that this system was a strong candidate for demonstrating the presence of a Quantized Anomalous Hall (QAH) state with a Chern number of 1.

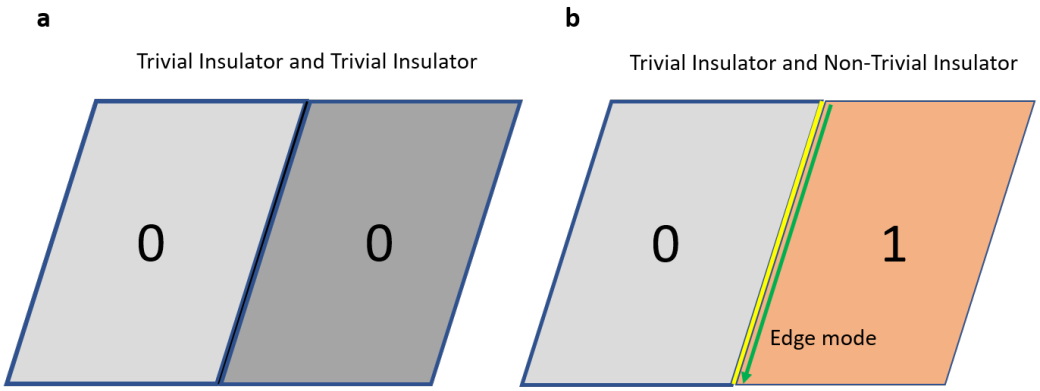

Figure 2.18: **a)** Two trivial insulators in contact with each other. The numbers in the insulator denote the "Chern number". Trivial insulators have zero Chern number, and topological insulators *usually* have non-zero Chern numbers. **b)** Trivial and topological insulator, in contact with each other. Because the Chern number of the topological insulator is 1, a single conducting mode appears at the boundary between the two insulators.

Sure enough, a few months later, Serlin *etal*. [39] confirmed this hypothesis within a few months, demonstrating the presence of a Quantized Anomalous Hall state surviving upto 6K - a lot higher than other systems that report the existence of the QAH state. The polarization of this quantized state could also be switched reliably by applying DC pulses on the order of a few nA. Notably, superconductivity is absent in these samples even though the TBG twist angles is extremely close to 1.1°. Unfortunately, the reproducibility of these samples is shockingly low, something that we hope we can address by our modified stacking technique that we will discuss in Chapters 3 and 4.

Very recently, Chen *et al.* [82] and Polshyn *et al.* [83] showed extremely interesting topological physics in heterostructures combining monolayer graphene with bilayer graphene. Instead of twisting two sheets of monolayer graphene, they took a monolayer graphene flake and stacked it on top of a bilayer graphene flake, making sure that the rotation between the two flakes was around 1.1°. Essentially, this means that you get a heterostructure comprising of Magic Angle TBG with a monolayer graphene flake aligned with the bottom graphene flake (very similar to TBG aligned with h-BN in that sense). For this type of structure, they observed topologically insulating behavior with a Chern number 2 ($h/\mathbf{2}e^2$) conductance along the edges and zero resistance in the bulk without any magnetic field. They were also able to switch the magnetization direction by applying magnetic fields of the order of a few

hundred mT.

It is clear from the above discussion that the substrate can play a huge role in determining the properties of TBG, and it becomes important to study the effect of substrates on TBG physics. In the next chapter, we tackle this question by swapping the h-BN substrate for WSe_2 - a Transition Metal Dichalcogenide (TMD) that has been previously studied as a high quality dielectric substrate for monolayer and bilayer graphene.

Chapter 3

SUPERCONDUCTIVITY IN TBG/WSe_2 HETEROSTRUCTURES

To further the understanding of superconductivity in TBG and to disentangle the myriad of electronic phases in TBG, we looked towards ways of explicit symmetry breaking (the origins and symmetry breaking involved in the many phases are mostly unknown and leave much to be explored). We decided to expand a well-established method, proximitizing graphene with WSe_2 - to TBG to explore which phases are further stabilized and which are suppressed. The surprising experimental discovery of our work is the striking resilience of superconductivity in TBG. Let's look at a few reasons why WSe_2 is an ideal choice for disentangling substrate effects in TBG.

3.1 Why WSe_2 with TBG?

Lattice mismatch

As discussed at the end of the last chapter, the closely related lattice constants of graphene and h-BN helped break the sublattice symmetry of graphene in TBG. The lattice constants of graphene and WSe_2 are significantly mismatched (0.353 nm for WSe2 and 0.246 nm for graphene - a 41% mismatch). As shown in Fig. 3.1, the maximum moiré wavelength you can achieve in this system is about 1 nm, which is much smaller than the magic angle wavelength (10 nm for the largest angle where correlated physics has been observed). This should assist in bringing out the "true" physics associated with the TBG moiré. Another effect that is certainly possible but not accounted for is the modification of TBG's phonon spectrum by WSe_2. If the superconductivity in TBG is purely driven by phonons, this substrate change should have a significant impact.

Induced spin-orbit coupling in Twisted Bilayer Graphene

After it became quickly established that TBG hosted physics related to strongly correlated electron systems, we asked ourselves, what would happen upon introducing spin-orbit coupling into this system? The following generic Hamiltonian describes such a system:

$$H = \sum_{i,j;\alpha\beta} t_{ij,\alpha\beta} c^{\dagger}_{i\alpha} c_{j\beta} + h.c. + \lambda \sum_{i} L_i \cdot S_i + U \sum_{i,\alpha} n_{i\alpha}(n_{i\alpha} - 1) \qquad (3.1)$$

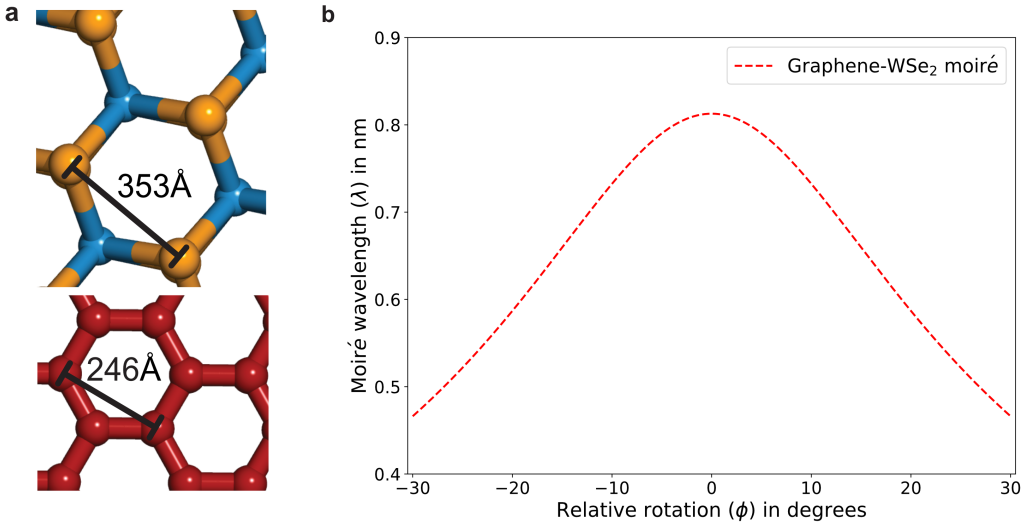

Figure 3.1: **a**) Lattice Mismatch between WSe_2 (yellow and blue) and Graphene (red). **b**) Resulting moiré between the two lattices.

where $c_{i\alpha}$ is the annihilation operator for an electron in orbital α at site i, $n_{i\alpha} = c^{\dagger}_{i\alpha} c_{i\alpha}$ is the corresponding occupation number, t is the hopping amplitude, λ is the atomic SOC entangling spin S_i and angular momentum L_i, and U is the Hubbard repulsion. Based on the relative strengths of U, λ, and t, one can be in a different electronic phase as represented by Fig. 3.2

It is important to emphasize that this simple looking Hamiltonian is not exactly solvable, and the lines demarcating different regions in the figure below are not rigid and serve more as a fluid boundary.

Drawing inspiration from other highly correlated electron systems, one could stabilize many phases in TBG depending upon the strength of induced spin-orbit coupling [84]. An obvious choice to induce spin-orbit coupling in TBG was WSe_2. WSe_2 itself has strong spin-orbit coupling because of the heavy W atoms (spin-orbit is a relativistic effect that connects the spin and orbital angular momenta of an electron and is proportional to Z^4 where Z is the atomic weight) [85]. Also, it had been well established in literature that monolayer WSe_2 in particular was believed to induce stronger spin-orbit coupling than few layer WSe_2.

High quality substrate

The quality (mean free path and charge inhomogeneity at charge neutrality point) of graphene devices is greatly affected by the supporting substrate for graphene. In some sense, the evolution of substrates for graphene since 2005 has led to the

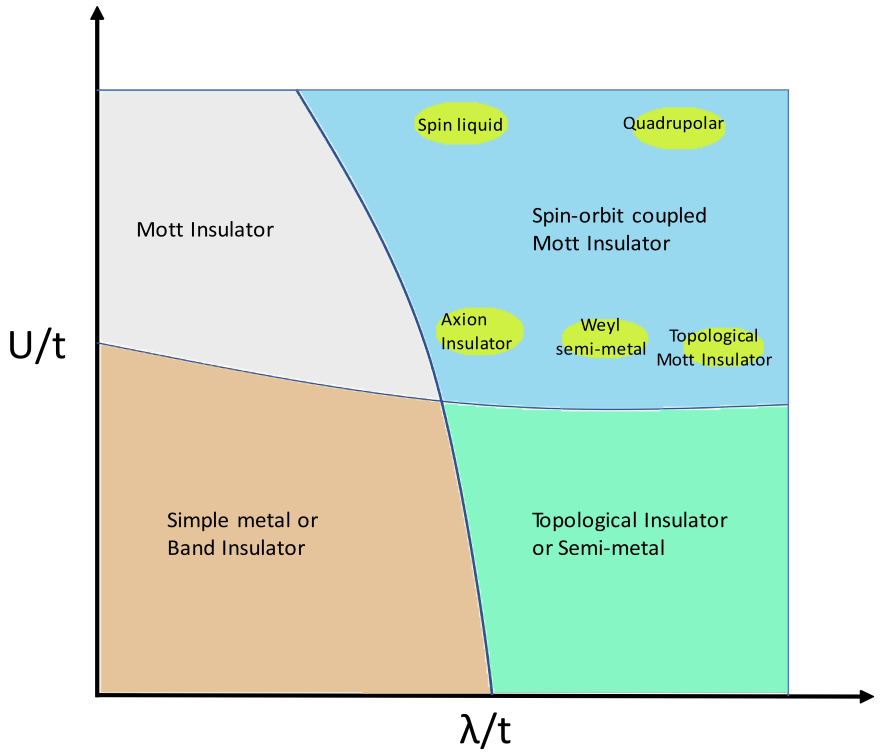

Figure 3.2: Different Phases in strongly interacting spin-orbit coupled systems, adapted from [84].

amazing discoveries in graphene. Prior to 2008, the widely used standard for high quality graphene devices was SiO_2 [4, 86]. It then became clear that isolating graphene from the substrate underneath by suspending would enable the fabrication of extremely high mobility graphene samples with mean free paths >2μm [87, 88, 89] and the observation of the fractional quantum hall effect in graphene for the first time [90, 91]. But these samples were very difficult to make given the tendency of suspended graphene to collapse during the fabrication process or upon applying a gate voltage.

Usage of hexagonal Boron Nitride (h-BN) as a substrate revolutionized the [92] world of graphene electronics by providing an atomically flat surface for graphene without residual charge puddles (unlike SiO_2). Phenomena that were observed in a few suspended graphene devices began being observed routinely with the use of h-BN. Other vdW materials also began being explored as possible substrates. Scanning Tunneling Microscopy (STM) and electronic transport measurements studied WS_2, WSe_2, MoS_2, and $MoSe_2$, among many others as possible choices [93, 94]. However,

WSe_2 consistently outperformed other materials, and graphene devices on WSe_2 have been shown to have similar quality as h-BN encapsulated devices [49, 93, 94]. In addition, WSe_2 is air stable, allowing the entire fabrication process to happen outside a glovebox, making the process a lot easier and more controllable. Therefore, WSe_2 was a natural extension as a substrate for TBG after h-BN.

3.2 Outline of devices studied in this chapter

Before diving into the physics of the TBG/WSe_2 devices that will be discussed in this chapter, it is important to explain what exactly we have measured. We will talk about data from 4 devices in this chapter and they are all fabricated using the method shown in Appendix B. Fig. 3.3 shows optical images of the devices along with pairs of contacts which were used to measure longitudinal resistances (R_{xx}) shown in blue lines and transverse resistance (R_{xy}) contacts shown in red lines. While there are several pairs of contacts that were fabricated for each device, not all the contacts worked equally well. Given TBG's unique bandstructure, we found that the yield of low resistance contacts was a lot lower than simple monolayer or bilayer graphene (75% compared to almost 100%). It has been suggested that using an SF_6 etch instead of a CHF_3 etch has much better yield and will be investigated in our lab in the next generation of devices. In light of the discussion about low control of twist angle in TBG devices in the last chapter, we emphasize again that most of the devices that we fabricate have at least one pair of contacts that we find to be of interest (defined below). The physical device also tends to be more homogenous than h-BN encapsulated devices. However, the twist angle can still vary by $\pm 0.1^\circ$ between adjacent pairs of contacts and $\pm 0.3^\circ$ from one end to the other end of the device. Therefore, the pairs of contacts studied here satisfy the following two criteria:

1. They have low contact resistance, a maximum of few kΩs measured in a two terminal geometry at high doping;
2. The area between the pair of contacts is within the range of interest ($1^\circ \pm 0.25^\circ$).

3.3 Superconductivity in TBG/WSe_2 close to magic angle

Because of how extremely sensitive the phase diagram of TBG is to details of fabrication, we were not sure of what to expect in terms of the robustness of different phases to a different substrate. No two TBG devices on h-BN show the

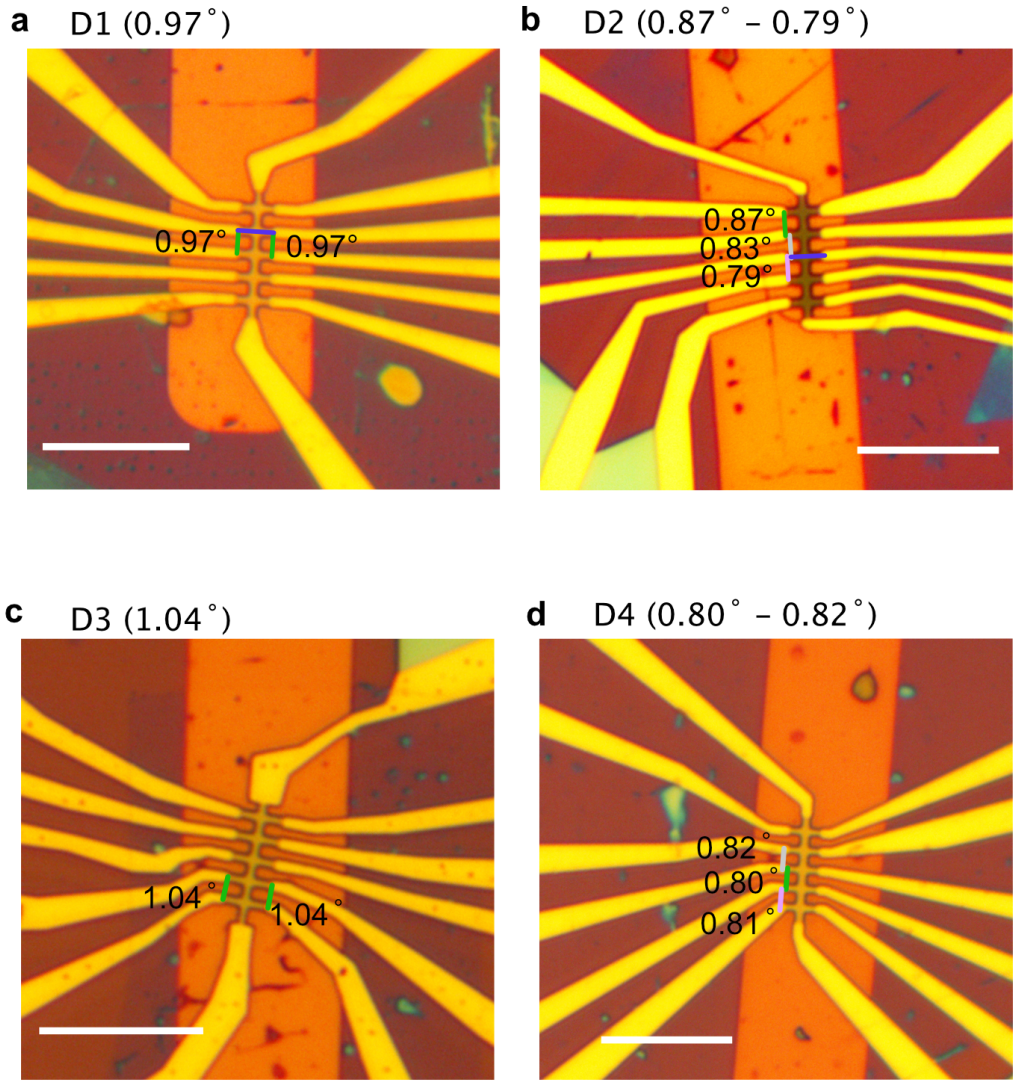

Figure 3.3: Optical images of devices discussed in Chapter 3. Electrodes that are used in the measurements and corresponding twisted angle are labeled for each device. The ones marked with the blue line are used for measuring transverse resistance (R_{xy}). Scale bar in each panel corresponds to 15 μm. The device hBN thicknesses for D1, D2, D3, and D4 are 62 nm, 40 nm, 48 nm, and 56 nm, respectively. D4 differs from the other devices since it features monolayer WSe_2 on both the top and bottom of the device. The gold gate under each TBG stack is used to modulate the density. The contact angle, for each pair of contacts listed, was determined from the Landau fan diagrams, as described in Chapter 4.

same exact behavior, inspite of being at the "same" angle and so far, the community has no idea how to resolve that issue. So it's very possible that swapping h-BN for WSe_2 could result in the emergence a new phase or the suppression of many. To this end, we ended up making a device with an angle relatively close to the magic angle of 1.1°(D3). As can be seen in Fig. 3.4, our device showed clear superconducting behavior as well as fully developed correlated insulating states, which provided us with confidence about the quality of these devices. Just based on the temperature data shown in Fig. 3.5, we didn't see any massive changes as compared to h-BN devices. However, we will discuss high-field data in Chapter 4 and highlight some differences observed in magnetic field. This device showed more twist angle disorder than other devices measured. This can be seen by how broad the correlated insulating state is around ν =+2, making it challenging to assign a single twist angle to this area. The fact that this device showed clear superconductivity despite the high angle disorder indicated that WSe_2 played a major role.

3.4 Fraunhofer-like field dependence: crucial test

Apart from zero resistance and the existence of a critical current, the verification of superconductivity hinges on the Meissner effect, where a superconductor expels external magnetic field acting like a perfect diamagnet (there is more to the Meissner effect, and this represents a simplistic view). In the case of a 2-D superconductor however, this crucial test is unavailable to experimentalists. Luckily, twisted bilayer graphene provides us with another method of independently corroborating the existence of 2-D superconductivity. Upon the application of a perpendicular magnetic field to TBG in the superconducting state, oscillations begin to emerge in the critical current as a function of field. These oscillations are periodic in nature and resemble the phase coherent oscillations of transport through an array of Josephson junctions akin to a superconducting quantum interference devices (SQUID) [80, 11]. The widely accepted belief in the community is that this effect arises due to different parts of TBG being at slightly different densities, therefore some parts are less superconducting than others or are perhaps even insulating (given how resistive TBG can be near the superconducting phase). So, the supercurrent densities can be different in neighboring areas manifesting themselves as phase coherent oscillations in magnetic field. Based on the period of these oscillations, it is common practice to quote the "effective junction area" (A) as

$$A = \varphi_0/\Delta B; \qquad \varphi_0 = h/2e$$

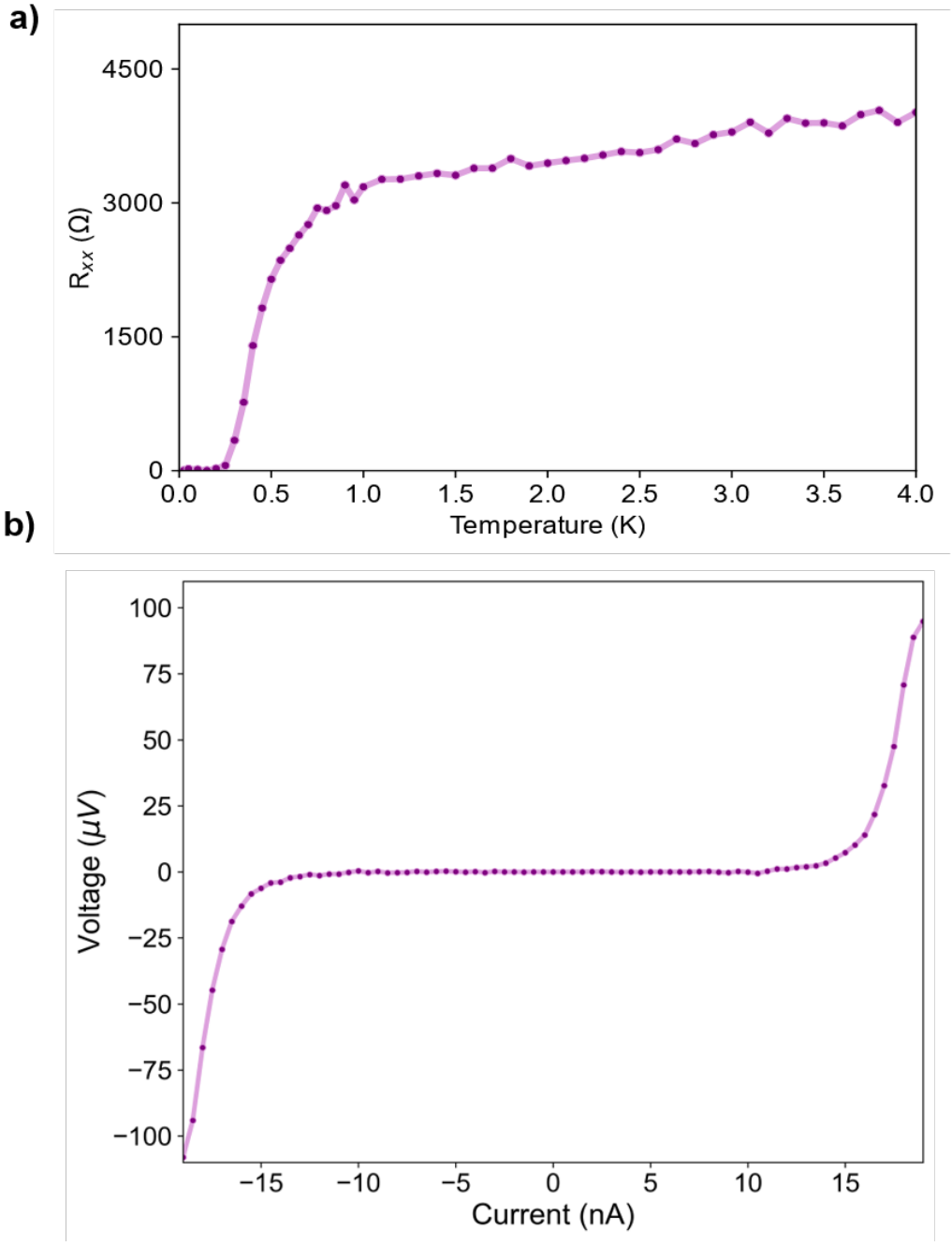

Figure 3.4: Superconductivity in device close to magic angle *i.e.* 1.04°(D3). **a)** Temperature dependence showing a drop in R_{xx} to zero indicative of superconductivity. **b)** Non linear I-V curve measured at ν =-2.3 filling factor at 50mK.

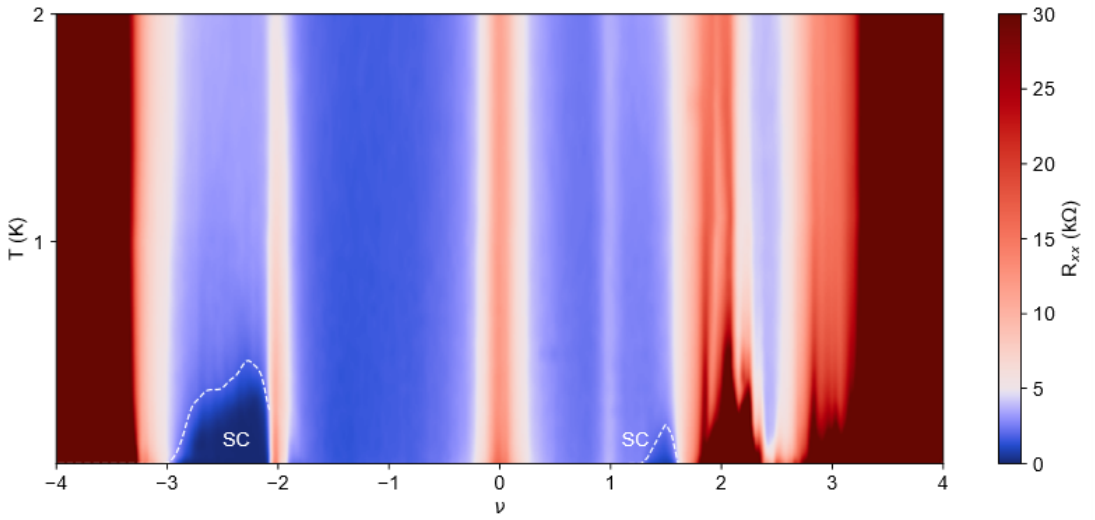

Figure 3.5: Temperature dependence as a function of electron(hole) density for low temperatures; ν denotes the filling factor of the flat band. Superconducting pockets around ±2 filling factor are visible.

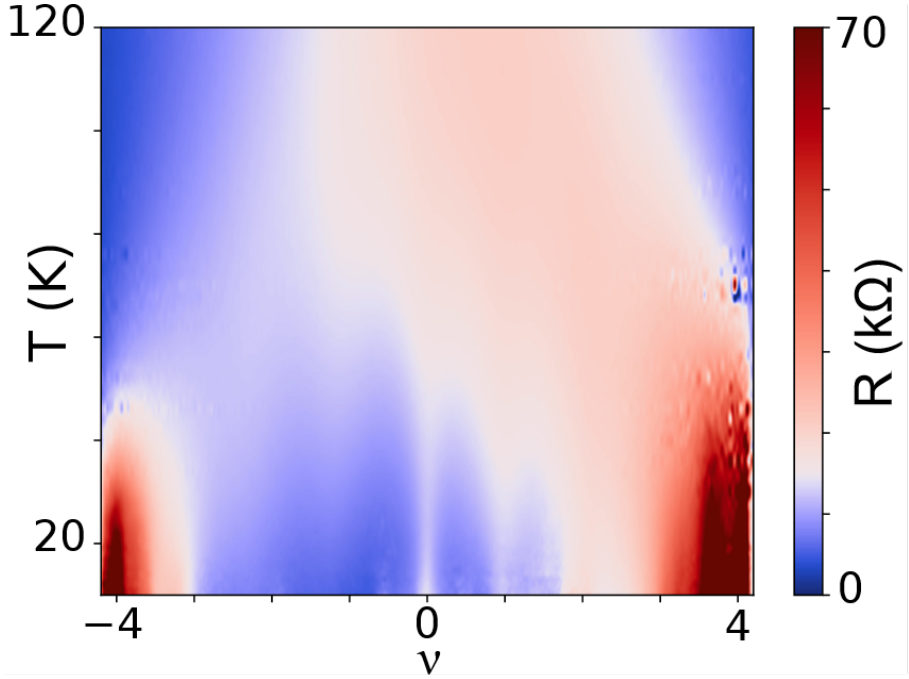

Figure 3.6: Temperature dependence for higher temperatures showing the development of several insulating states; ν denotes the filling factor of the flat band.

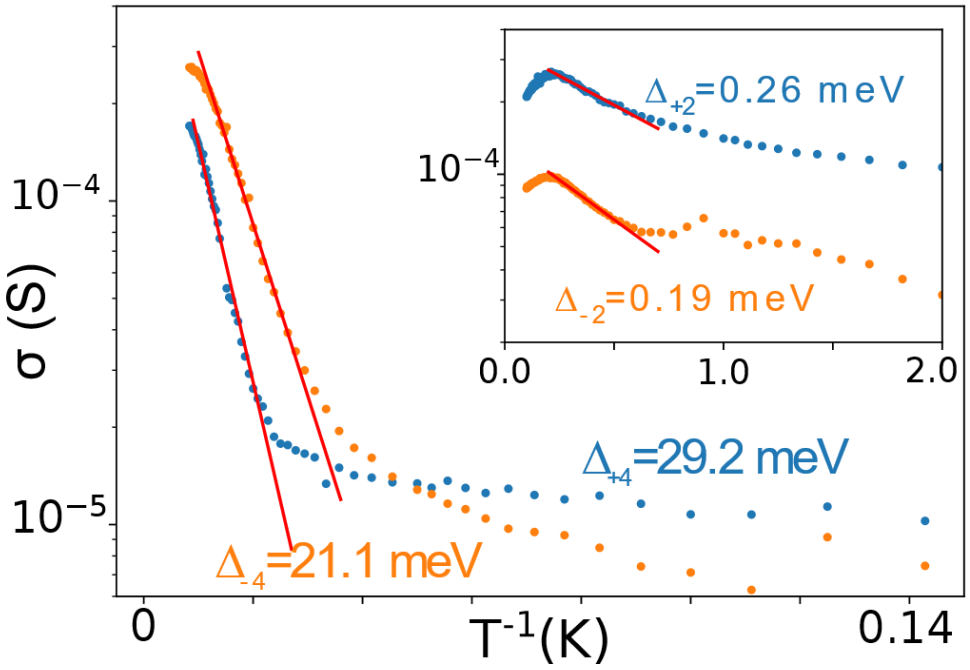

Figure 3.7: Full filling gap extraction for 1.04° (D3). These gaps indicate that the flat bands are isolated from the high energy dispersive bands by 20-30 meV. Inset shows the gap extraction for half filling correlated insulating states (±2).

However, this interpretation is not well established as of now because of the inconsistencies in the shape of these oscillations between different devices (or even pairs of contacts). Depending on where one is located in density space, this oscillatory behavior can be modulated by quite a bit. We emphasize that all our TBG/WSe_2 devices where the resistance goes to zero, show the presence of effect.

3.5 Superconductivity without insulating states

Based on the initial picture described by Cao *et al.* [11], and subsequent measurements by Yankowitz *et al.* [80] and Lu *et al.* [78], the superconducting states in TBG were always accompanied by correlated insulating states (the term "Mott" insulating state in the context of TBG lost credence after in-plane magnetic field measurements were conducted). We did observe superconducting pockets in close proximity to the insulating states for the devices close enough to 1.1°. We then started investigating devices further away from the magic angle.

Upon tuning the twist angle away from the magic angle at θ = 0.97°, a superconducting pocket emerges on the hole side near ν = –2 with a maximal transition

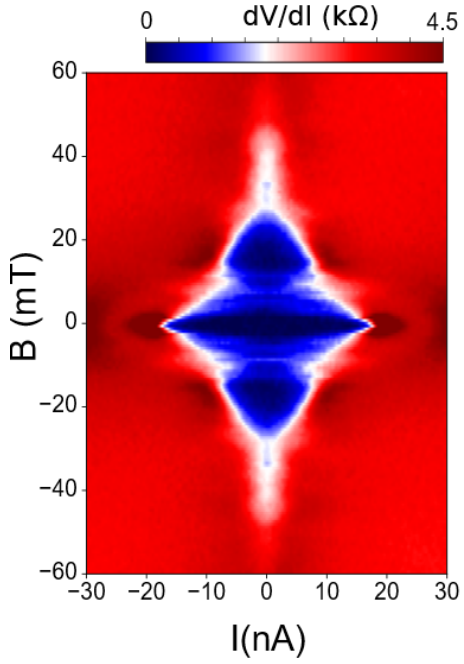

Figure 3.8: Oscillations in magnetic field resembling the phase coherent oscillations for an array of Josephson junctions indicating the percolative nature of superconductivity in TBG.

temperature $T_c \approx 0.8$ K. To our knowledge, this already is the smallest angle for which superconductivity has been reported for hole doping. Careful inspection reveals another weak superconductivity pocket close to $\nu = +2$ (the behavior at low fields is displayed in Fig. 4.1). However, despite the small twist angle falling outside the $\theta_M \pm 0.1°$ range, the observed phase diagram resembles that of regular high-quality magic-angle hBN-TBG-hBN structures [11, 78]. For this angle, correlated insulating states are also observed for filling factors $\nu = +2, +3$ with activation gaps of $\Delta_{+2} = 0.68$ meV and $\Delta_{+3} = 0.08$ meV, whereas at other filling factors correlated states are less developed and do not show insulting behavior (see Fig. 3.11 and Fig. 3.9).

Although superconductivity persists for all three angles, the correlated insulators are quickly suppressed as the twist angle is reduced. This suppression is not surprising, as for angles below θ_M, the bandwidth increases rapidly and, moreover, the characteristic correlation energy scale $e^2/4\pi\epsilon L_m$ also diminishes due to an increase in the moiré periodicity $L_m = a/sin(\theta/2)$ ($a = 0.246$ nm denotes the graphene lattice constant) [72, 12, 95, 71, 96, 97]. For the lower angle of $\theta = 0.87°$, correlated-insulating behavior is heavily suppressed at all filling factors. In

Fig. 3.12 a peak in longitudinal resistance versus density is visible only around ν = +2 above the superconducting transition (T_c = 600–800 mK). Data for a larger temperature range in Fig. 3.14 shows that the resistance peak near ν = +2 survives up to T = 30 K, and also reveals a new peak near ν = +1 in the temperature range 10-35 K. These observations suggest that electron correlations remain strong, though the corresponding states appear to be metallic as the overall resistance increases with temperature. For this angle, we measure activation gaps at full filling (i.e., at ν = ±4) of Δ_{+4} = 8.3 meV and Δ_{-4} = 2.8 meV Fig. 3.17, far smaller than the gaps around θ_M, in line with previous results that report a disappearance of the band gap separating dispersive and flat bands at around θ = 0.8° [98, 99].

At the smallest angle, θ = 0.79°, along with the lack of insulating states at any partial filling, the resistance at full filling is even more reduced as seen in Fig. 3.12 and Fig. 3.15. The relatively low resistances <2 kΩ measured at full filling, which are less than 15% of the resistance at the charge neutrality point (CNP), suggest a semi-metallic band structure around full filling, consistent with theoretical expectations for TBG at θ = 0.79° [98] and the resistivity of a dilute 2D electron gas [100]. Surprisingly, despite the absence of both full-filling band gaps and correlated insulators, the superconducting low-resistance pocket near ν = +2 is clearly resolved in Fig. 3.15.

3.6 What impact does this have on the origin of superconductivity?

Both the disappearance of the correlated insulators and the vanishing gap between flat and dispersive bands for low angles suggest that the additional WSe_2 monolayer does not significantly change the magic angle (on the scale of angles considered here). Since superconductivity survives to much lower angles compared to correlated insulating states, our observations strongly suggest the two phenomena have different origins [101, 102]. Note also that the close proximity of the dispersive bands does not seem to have a major impact on the superconducting phase. While these findings are in contrast with scenarios wherein superconductivity descends from a Mott-like insulating state as in high-T_c superconductors [103], we do emphasize that electron correlations may still prove important for the development of superconductivity. For instance, even for the smallest angle of θ = 0.79°, the superconducting pocket is seemingly pinned to the vicinity of ν = 2. Additionally, as shown in Fig. 3.15, at higher temperatures residual R_{xx} peaks can still appear at certain integer filling factors despite the absence of gapped correlated insulating states. It is thus hard to rule out the possibility that superconductivity arises from

correlated states of metallic nature that may be present at smaller angles and near integer values of ν in analogy to other exotic superconducting systems [104, 105, 106]. However, our findings are also consistent with phonon-only mediated superconductivity [107, 108]. It is thus hard to rule out the possibility that, at smaller angles and near integer values of ν, correlated states of a metallic nature may be present in analogy to, for example, heavy-fermion or organic superconducting systems.

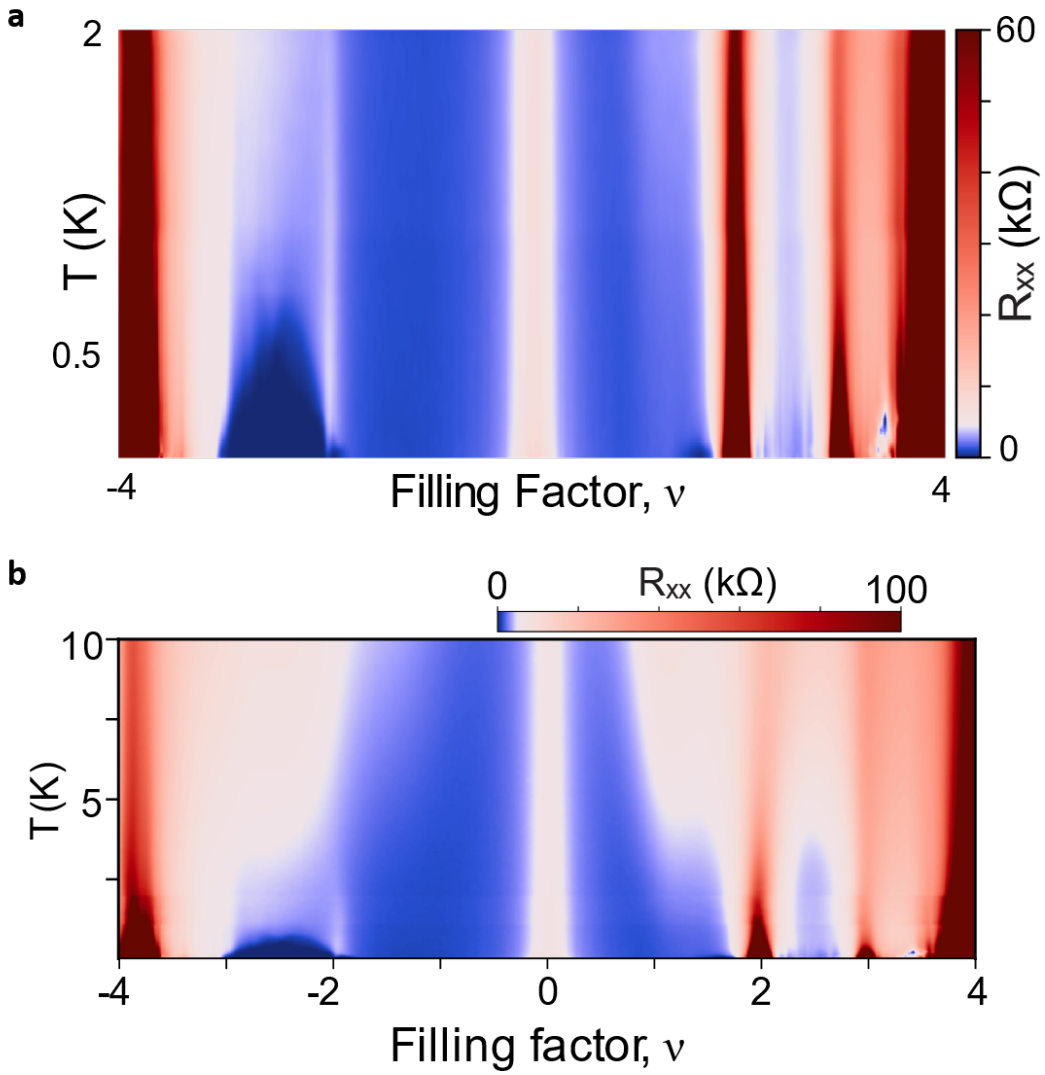

Figure 3.9: Phase diagram for D1 (0.97°). **a)** Up to 2K, a big superconducting pocket exists near -2 filling factor (maximal T_c 800 mK), and a much smaller superconducting pocket exists near +2 filling factor. **b)** Up to 10K. Compared to the 1.04° device, the -2 filling factor (half filling) insulating state is already suppressed.

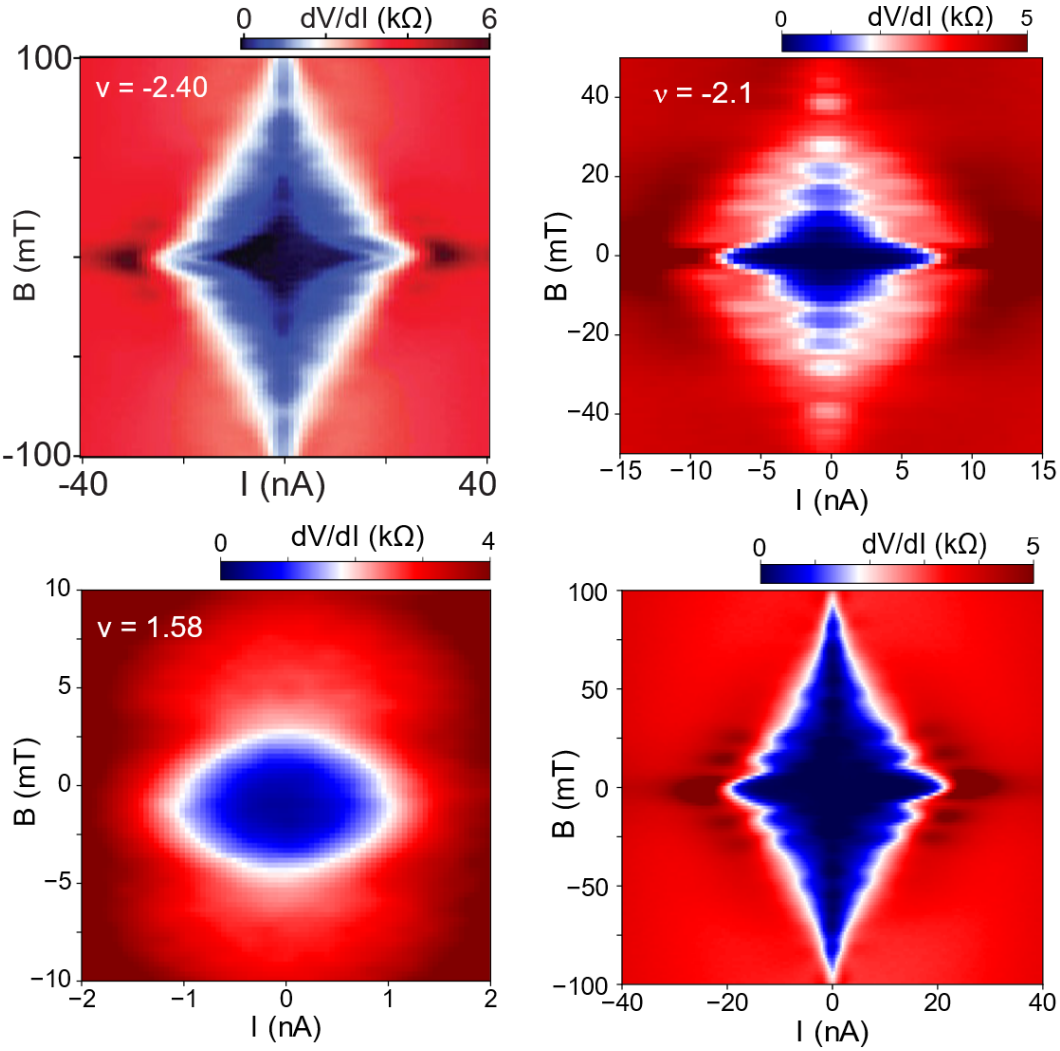

Figure 3.10: Variation of critical current as a function of magnetic field (device D1 0.97°). Different filling factors show different periods of oscillations most likely due to the change in the superconducting area of the device.

3.7 Gap extraction for insulating states

By looking at the temperature dependence of the insulating states on a log scale, it becomes easy to notice that they exhibit a linear activation behavior for a wide temperature which can be usually fit through an Arrehenius gap equation,

$$\sigma \propto e^{-\Delta/(2k_bT)} \tag{3.2}$$

where σ is the longitudinal conductivity and Δ is the desire gap value. At lower temperatures however, the conductivity begins to saturate, indicating that another mechanism of thermal activation is taking over [74], such as variable range hopping

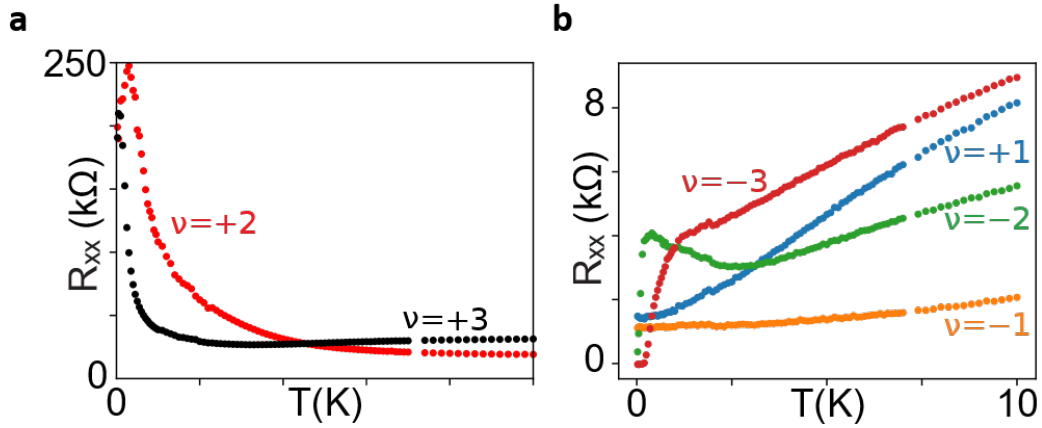

Figure 3.11: Temperature dependence of resistance at partial filling factors for D1 (0.97°). **a)** Correlated insulating behavior seen for +2 and +3 filling factors consistent with previous studies. **b)** Metallic or superconducting behavior is observed for other partial filling factors.

(VRH), and that part fits better to

$$\sigma \propto e^{-(T/T_0)^{1/3}} \tag{3.3}$$

The choice of the exponent (1/3) for the VRH is based on a Mott hopping assumption because the exponent should be 1/(d+1) for a Mott insulator and $d = 2$ for 2 dimensions. If the hopping is assumed to be Efros-Shklovskii VRH, the exponent should be 1/2, and the fit would work fairly well for this value too since there are so many fitting parameters. The important point here is not so much to determine one or the other VRH mechanism but the fact that localization takes over at low temperatures. The entire temperature range can therefore be fit according to

$$\sigma = Ae^{-\Delta/(2k_bT)} + Be^{-(T/T_0)^{1/3}} \tag{3.4}$$

where A,B,Δ, and T_0 are the fit parameters.

3.8 Optimized measurements of resistance near the superconducting pocket

In a ballistic graphene system, it has been seen that resistances can often go to zero and below zero [109] without the system being in a superconducting state. Therefore, it alone is insufficient evidence to claim superconductivity in a system. However measuring a zero resistance is still important to the claim of superconductivity, and that can be particularly challenging in the case of TBG given the extreme range of resistances it exhibits in temperature and density spaces. In Fig. 3.19, we show

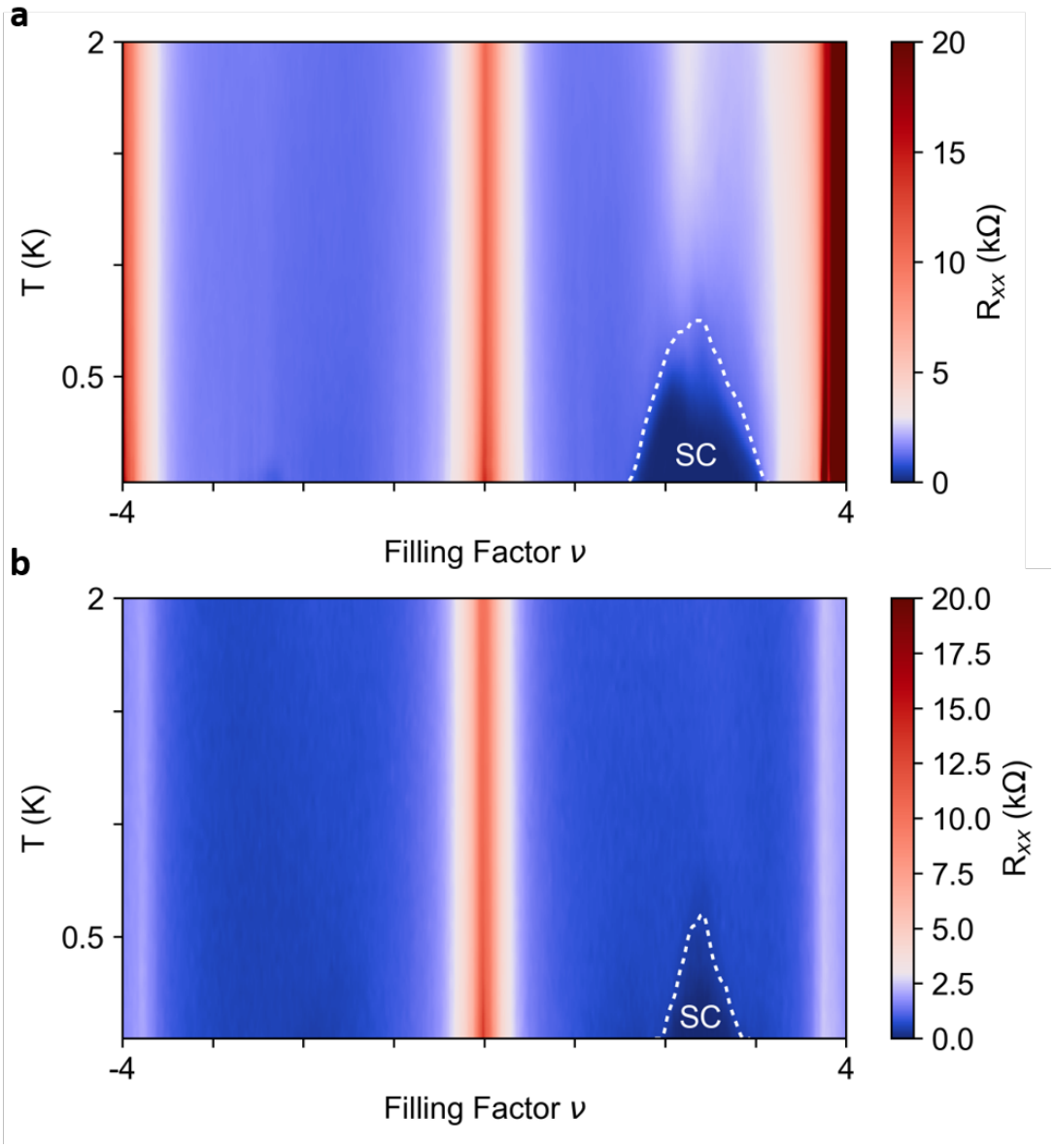

Figure 3.12: Longitudinal resistance R_{xx} vs. temperature and electron density, expressed as a flat-band filling factor in device D2. Superconducting domes (SC) are indicated by a dashed line that delineates half of the resistance measured at 2 K. **a)** For the 0.87° area. **b)** For the 0.79° area.

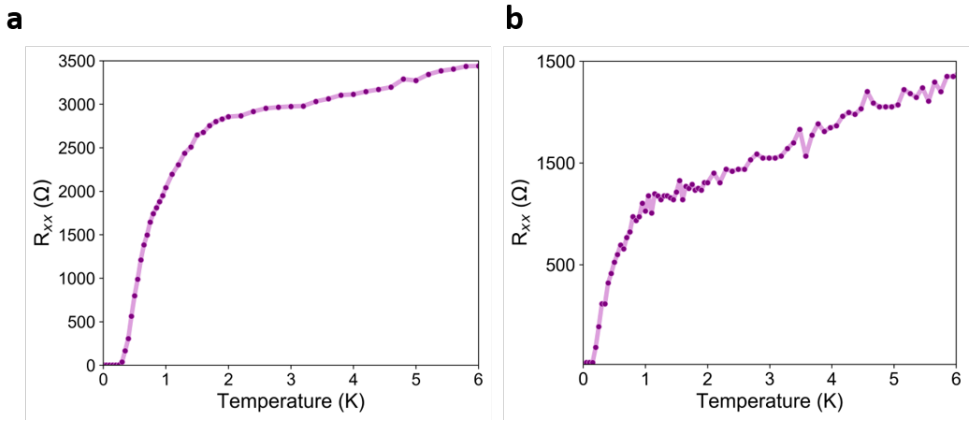

Figure 3.13: Line cuts of resistance vs temperature showing the superconducting transition in device D2. **a)** For the 0.87° area. **b)** For the 0.79° area.

examples of how the measurement of resistance in the superconducting state can be affected by changing the parameters of the lock-in amplifier used.

3.9 Possible mechanisms for stabilizing superconductivity

In our experience with making these devices, it appears that the yield for observing superconductivity is significantly higher than h-BN encapsulated devices. In comparison to previous studies [11, 80, 78, 101, 102], the main difference in our samples originates from the addition of WSe_2 monolayer. There are several possible reasons why this change stabilizes superconductivity at smaller angles. For example, details of the microscopic interface between graphene and h-BN (or WSe_2) differ in friction coefficient, which could play an important role in setting the angle disorder distribution during the fabrication process.

While other details of fabrication have a significant impact, we have observed less angle disorder in the WSe_2 based samples. There could be less disorder on an atomic scale and/or on a domain level where we have larger domains with the same angle. It is also possible that WSe_2 helps provide more integrity to the TBG, making it more likely to have a possible superconducting percolation path based on the very high yield of superconductivity in our devices. Further insight into this will be provided by STM studies from our lab.

Besides, various effects can arise from having different interfaces on the two sides of the TBG due to differences in the moiré patterns or built-in electric fields. More fundamentally, WSe_2 could affect interlayer coupling in TBG and overall electronic band structure and density of states through inducing SOI, the renormalization of

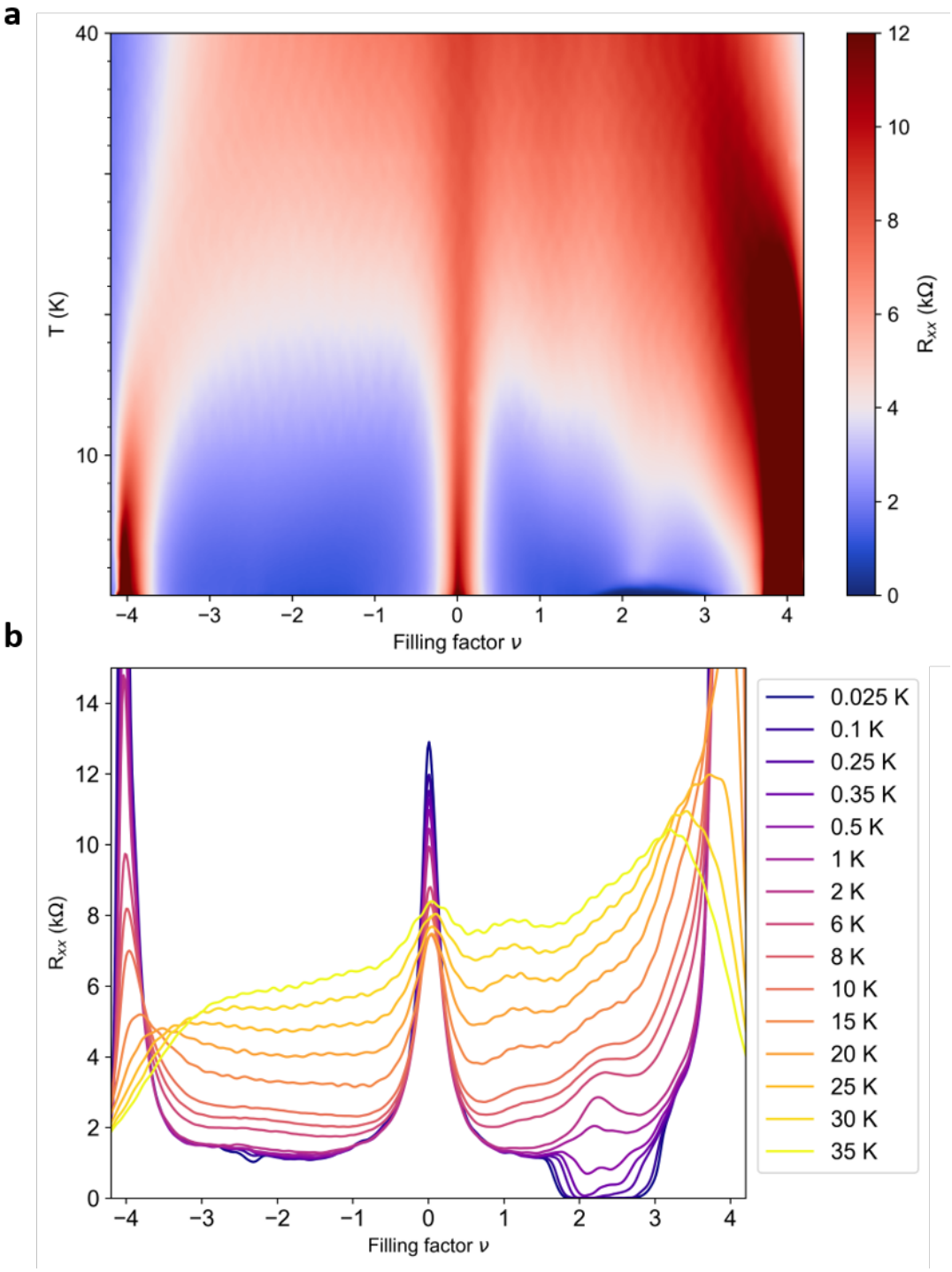

Figure 3.14: **a)** Larger-temperature-range data showing R_{xx} as a function of filling factor for the 0.° area. Note the absence of correlated insulating states. **b)** Line cuts from a) highlighting the developing of the superconducting pocket around +2 filling factor.

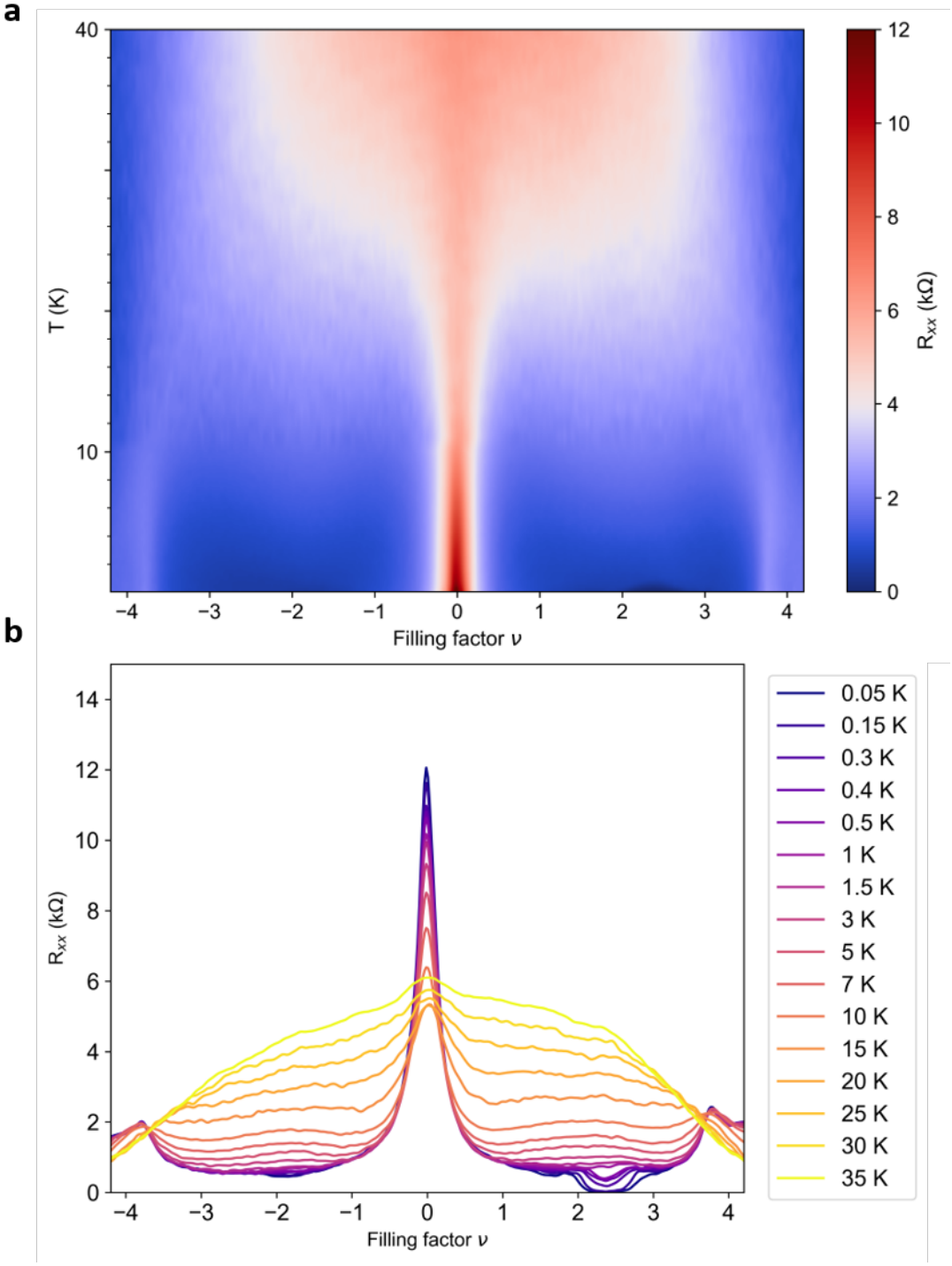

Figure 3.15: **a)** Larger-temperature-range data showing R_{xx} as a function of filling factor for the 0.79° area. Note the complete absence of *any* insulating states. **b)** Line cuts from a) highlighting the developing of the superconducting pocket around +2 filling factor.

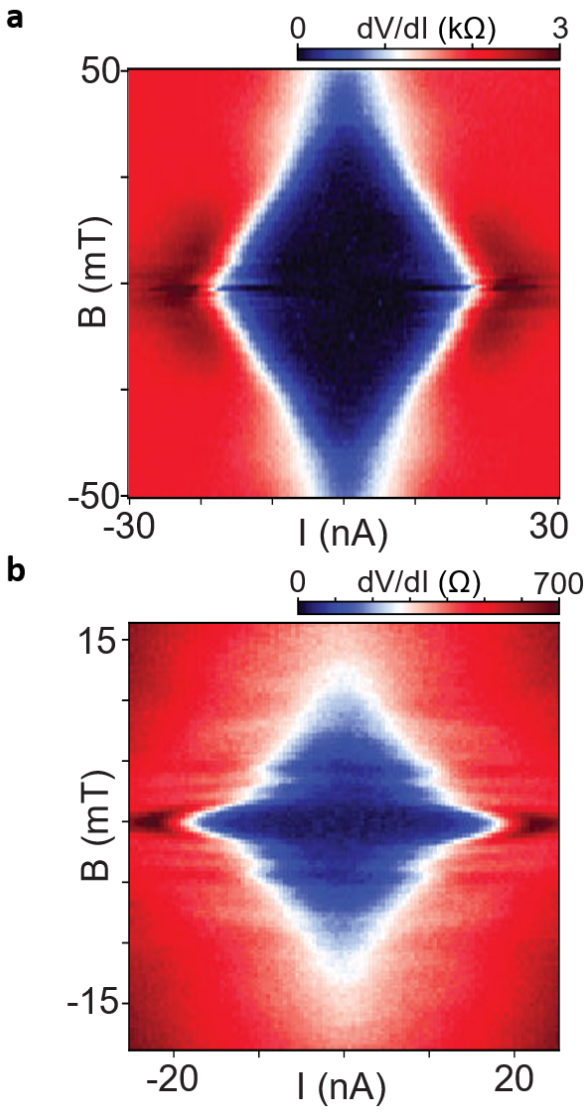

Figure 3.16: Strong evidence for superconductivity in non-magic angle devices, oscillations in magnetic field for low angles. **a)** 0.87° area D2, **b)** 0.79° area D2. The critical field for superconductivity appears to diminish as we go further away from the magic angle value of 1.1°.

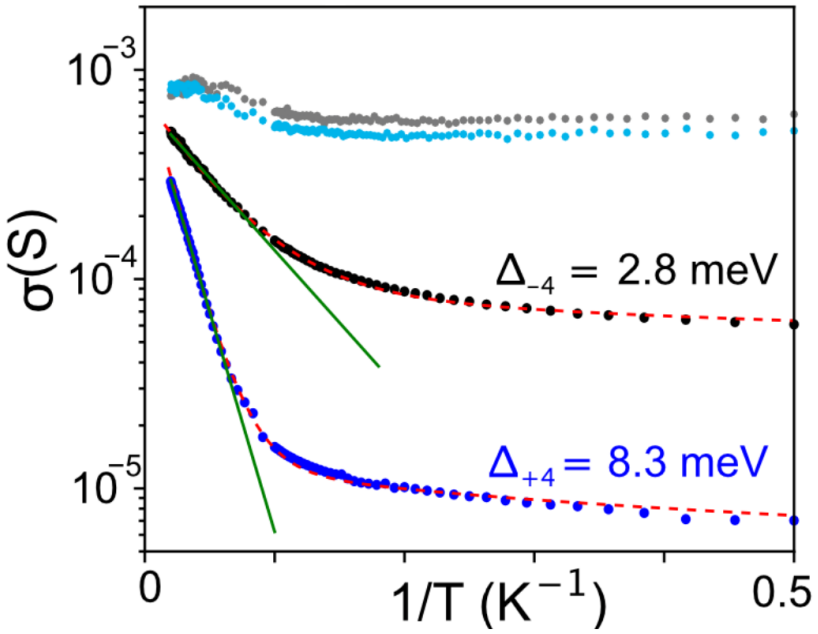

Figure 3.17: Conductance vs. 1/T for full filling $\nu = \pm 4$ extracted for the 0.87° area in blue and black and for the 0.79° area in cyan and gray. Green and red lines are fits for $\theta = 0.87°$, to a model that includes only activation (green) and both activation and variable-range hopping of the form $\exp[-(T_0/T)^{1/3}]$ (red). The gap values shown are extracted from the activation only fits (to the form of $\sigma \propto e^{-\Delta/2k_BT}$); the more complete model gives similar gap values of $\Delta_{+4} = 9.4$ meV and $\Delta_{-4} = 3.7$ meV. The behavior for $\theta = 0.79°$ shows much smaller variation in temperature.

Fermi velocity, and other factors. It is likely that a combination of these band-structure related factors is essential for stabilizing superconductivity.

Based on the current generation of devices, it is difficult to pin down the exact role of spin-orbit coupling in stabilizing superconductivity at very small angles. Dual gated devices (both top and bottom gates present) where spin-orbit coupling can be tuned by the application of a displacement field will help shed more light on this topic. If the superconductivity can be suppressed/enhanced by changing the spin-orbit coupling in situ, it will help establish a strong connection between the two.

3.10 Doubly encapsulated TBG/WSe_2 devices

In addition, to rule out the effects of built-in electric fields or differences in moiré patterns, we started fabricating devices with WSe_2 on both sides of TBG. The fabrication process here was the same as the single sided WSe_2 devices, except we

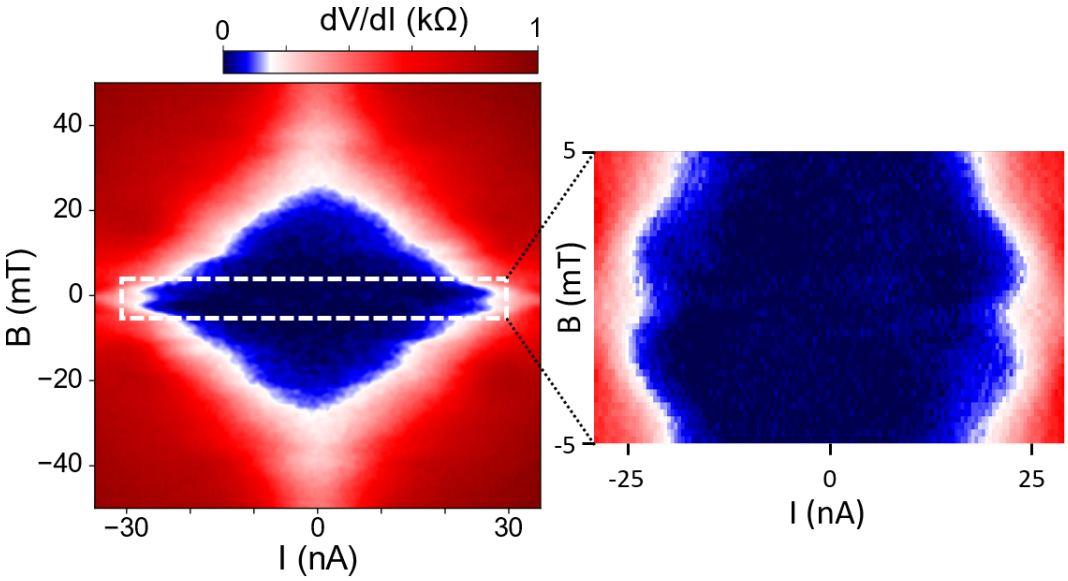

Figure 3.18: Anomalous quantum interference pattern for 0.83° area in magnetic field. The critical current shows a dip at zero field as opposed to a peak. Zoom in shows a better view of the tow lobes around zero, indicating a phase shift consistent with a 0-π Josephson junction.

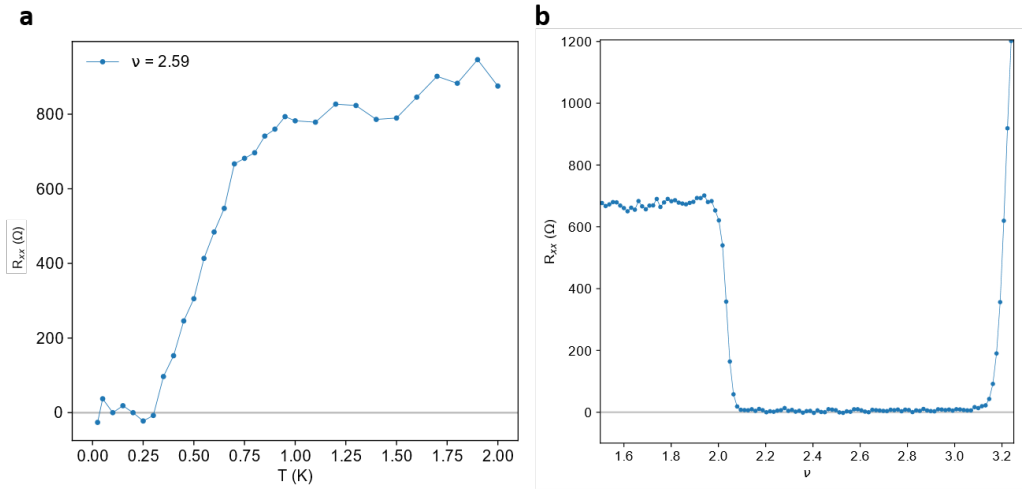

Figure 3.19: Sensitivity of the resistance measured in the superconducting state to the lock-in parameters. **a)** For very low excitation currents used while measuring temperature dependence, resistance can go negative as a result of noise. **b)** Resistance measured near the superconducting pocket as a function of backgate voltage with 5 times higher current provides a much more stable value of resistance near zero.

now picked up another monolayer WSe_2 after picking up the TBG layers. Fig. 3.20 shows the superconductivity data for one such device. The twist angle determined in this device was around 0.8°. The most striking thing about this data is the strong similarity to the device D2 0.79° area where we observed superconductivity in the absence of all insulating states. The confirmation of this behavior is extremely important as it rules out twist angle disorder as source of superconductivity in device D2. Similar to Ref. [11], we were able to extract a BKT transition temperature for our 2-D superconductivity.

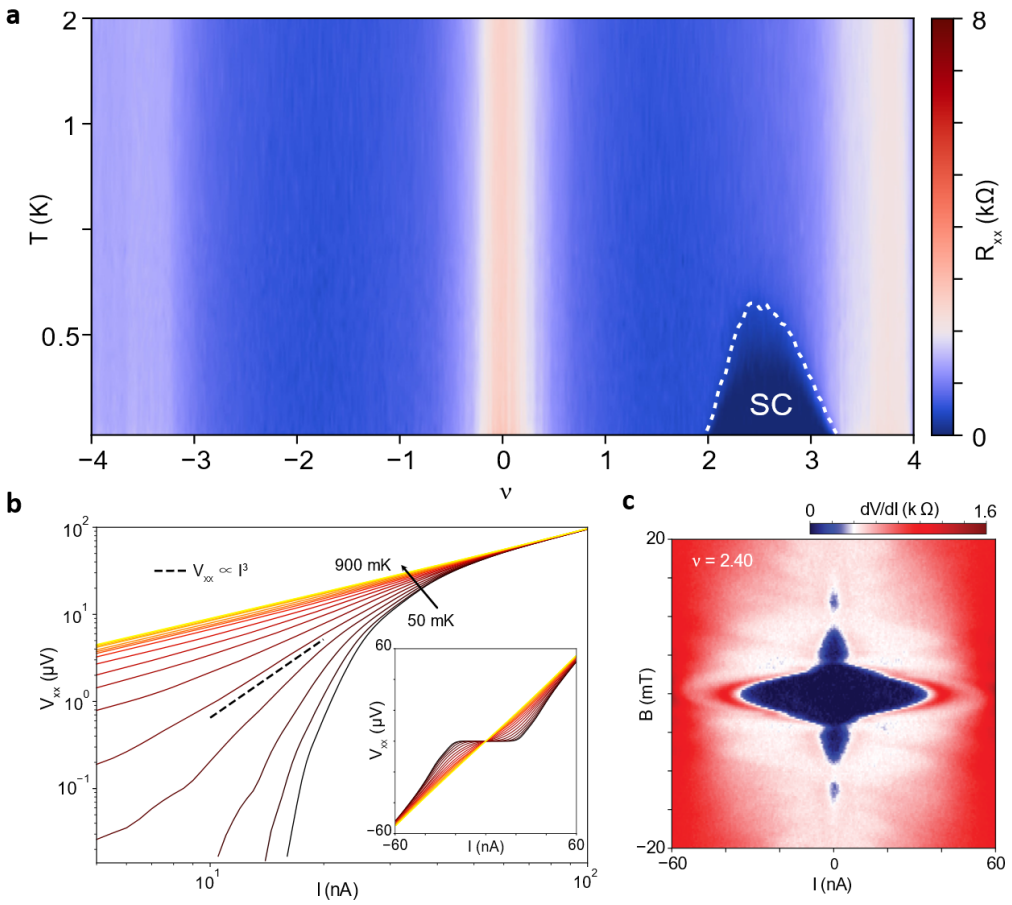

Figure 3.20: Superconductivity data for device D4 (0.80°). D4 was fabricated with monolayer WSe_2 on both the top and bottom of the TBG. **a)**, R_{xx} as a function of ν and temperature to 2 K, revealing a superconducting pocket over the range of $2 < \nu < 3.2$ and resistance at full filling ($\nu = |4|$) less than at the charge neutrality point. **b)** Current vs. voltage at $\nu = 2.79$, at temperatures from 50 mK to 900 mK, in 50 mK steps. The main plot is on the log scale in both axes, revealing a BKT transition temperature near 250 mK. Inset: I-V dependence for the same temperatures. **c)** Fraunhofer-like pattern for D4 at $\nu = 2.40$.

3.11 Constraints imposed on superconductivity

There several theories that are being actively pursued as possible explanations for superconductivity in TBG:

1. Certain theories claim similarities between TBG and cuprates where superconductivity emerges from "Mott" insulating states. Our work rules out these theories based on the fact that no insulating state is observed accompanying superconductivity.

2. In other theories, superconductivity in TBG is driven by electron-phonon coupling in the presence of a large density of states. While our experiment is entirely consistent with this class of theories, the observation of superconductivity down to 0.8° gives an estimate on upper bound for the density of states needed for such a scenario to occur and imposes strict requirements for this type of theory.

3. A variety of other theories proposed mechanisms based on Fermi surface nesting, valley-fluctuations, and/or propose unconventional pairing; for example, Isobe *et al.* [110] and Liu *et al.* [111]. All of these theories assume either the presence of flat bands, having an isolated band structure, or having certain large peaks in the density of states. For each of these theories, our experiment imposes restrictions that could not have been obtained by only studying TBG encapsulated using BN.

However, none of these theories consider the effects of the SOI presence and how it may affect superconducting state. Induced SOI can additionally constrain the nature of the TBG phase diagram. In particular, the SOI acts as an explicit symmetry-breaking field that further promotes instabilities favoring compatible symmetry-breaking patterns while suppressing those that do not. The relative robustness of the $\nu = 2$ correlated insulator in our $\theta = 0.97°$ device suggests that interactions favor re-populating bands [112, 113] in a manner that also satisfies the spin-orbit energy. Furthermore, the survival of superconductivity with SOI constrains the plausible pairing channels, particularly given the dramatic spin-orbit-induced Fermi-surface deformations that occur at $\nu = +2$ (Fig. 3.24). Superconductivity in our low-twist-angle devices, for instance, is consistent with Cooper pairing of time-reversed partners that remain resonant with SOI. Thus, the stability of candidate insulating and superconducting phases to the SOI provides anontrivial constraint for theory [114, 115, 107, 116, 117].

3.12 Theoretical modeling of induced spin-orbit coupling in TBG

Monolayer graphene with induced spin orbit coupling

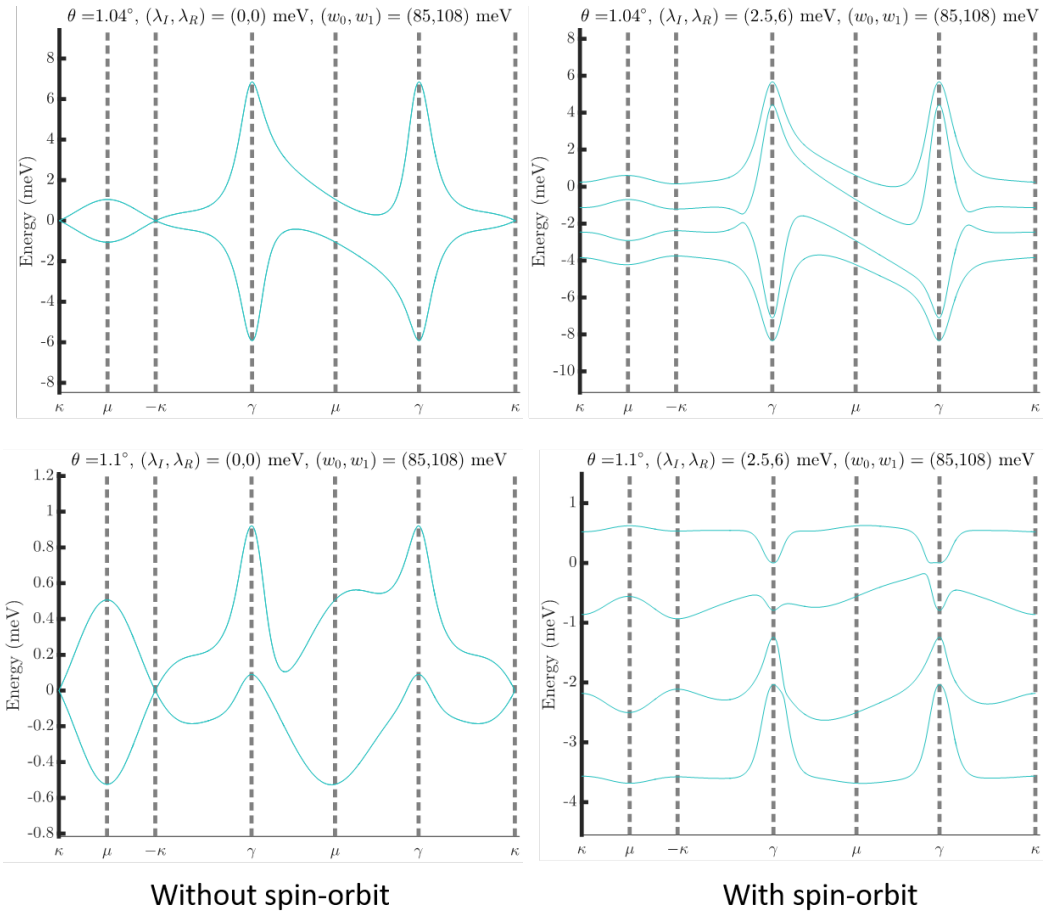

Figure 3.21: Continuum model simulations with and without considering the effects of spin-orbit coupling on the low energy bandstructure of TBG for angles closer to the magic angle value of 1.1°.

We begin by describing the induced spin-orbit felt by monolayer graphene adjacent to a transition metal dichalcogenide (TMD). In the absence of spin-orbit coupling, the low-energy Hamiltonian for the monolayer is

$$H_0 = -v_0 \int_{\boldsymbol{k}} \Psi^\dagger(\boldsymbol{k}) \Big(k_x \sigma^x \tau^z + k_y \sigma^y \Big) \Psi(\boldsymbol{k}), \tag{3.5}$$

where $\Psi(\boldsymbol{k})$ is an eight component spinor with sublattice, valley, and spin indices. The Pauli matrices $\sigma^{x,y,z}$ act on sublattice indices of the spinor, while $\tau^{x,y,z}$ act on the valley indices. The Fermi velocity is approximately $v_0 \sim 10^6$ m/s [118]. The

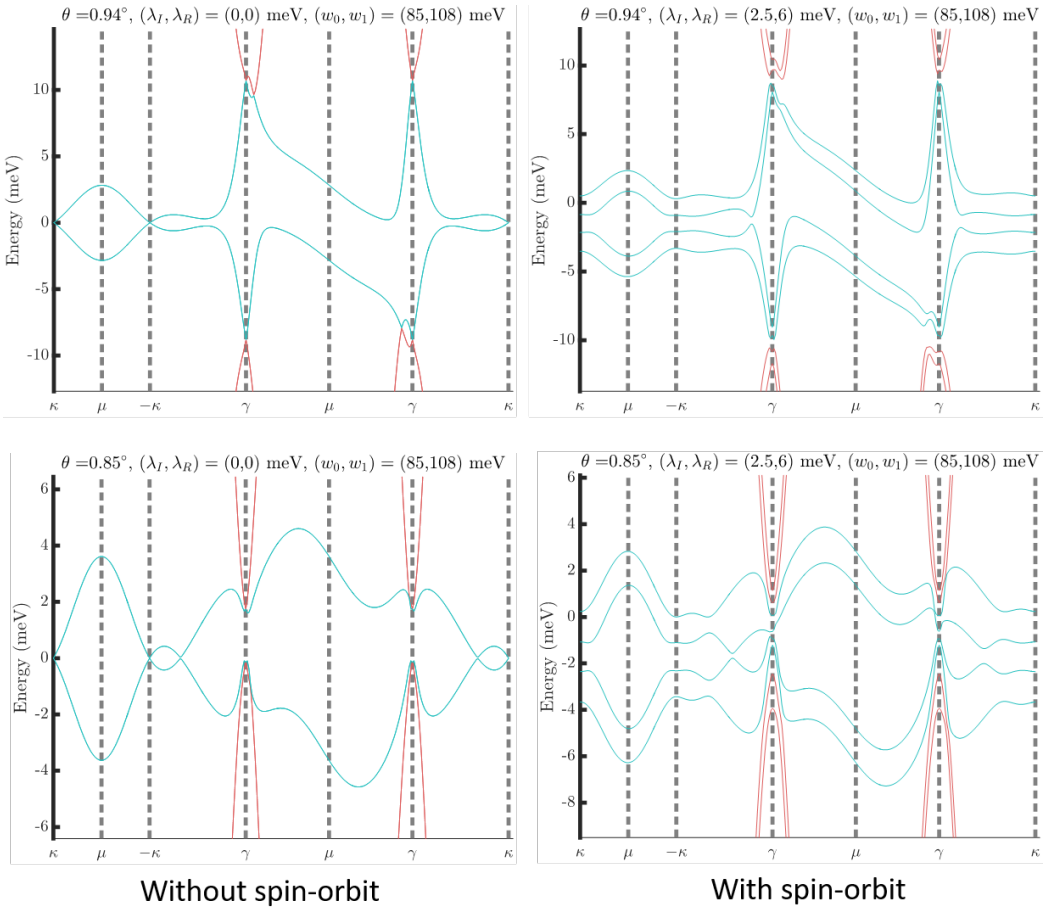

Figure 3.22: Continuum model simulations with and without considering the effects of spin-orbit coupling on the low energy bandstructure of TBG for angles further away from the magic angle value of 1.1°.

proximate TMD induces both Ising and Rashba terms, which may be included by taking $H_0 \rightarrow H_0 + H_{\mathrm{SO}}$, where [119, 120]

$$H_{\mathrm{SO}} = \int_{\boldsymbol{k}} \Psi^{\dagger}(\boldsymbol{k}) \left(\frac{\lambda_I}{2} \tau^z s^z + \frac{\lambda_R}{2} \left(\tau^z \sigma^x s^y - \sigma^y s^x \right) + \frac{1}{2} m \sigma^z \right) \Psi(\boldsymbol{k}). \tag{3.6}$$

Here, $s^{x,y,z}$ act on the spin indices. The parameters λ_I and λ_R quantify the strength of the Ising and Rashba terms respectively, while m represents a mass. Their values, as expected from density functional theory calculations, vary widely: $m \sim 0 - 1$ meV, $\lambda_I \sim 1 - 5$ meV, and $\lambda_R \sim 1 - 15$ meV [119, 121].

A Kane-Mele mass [122] may also be induced, but in practice this term is expected to be negligibly small relative to the others [123, 124, 125], and so we neglect it

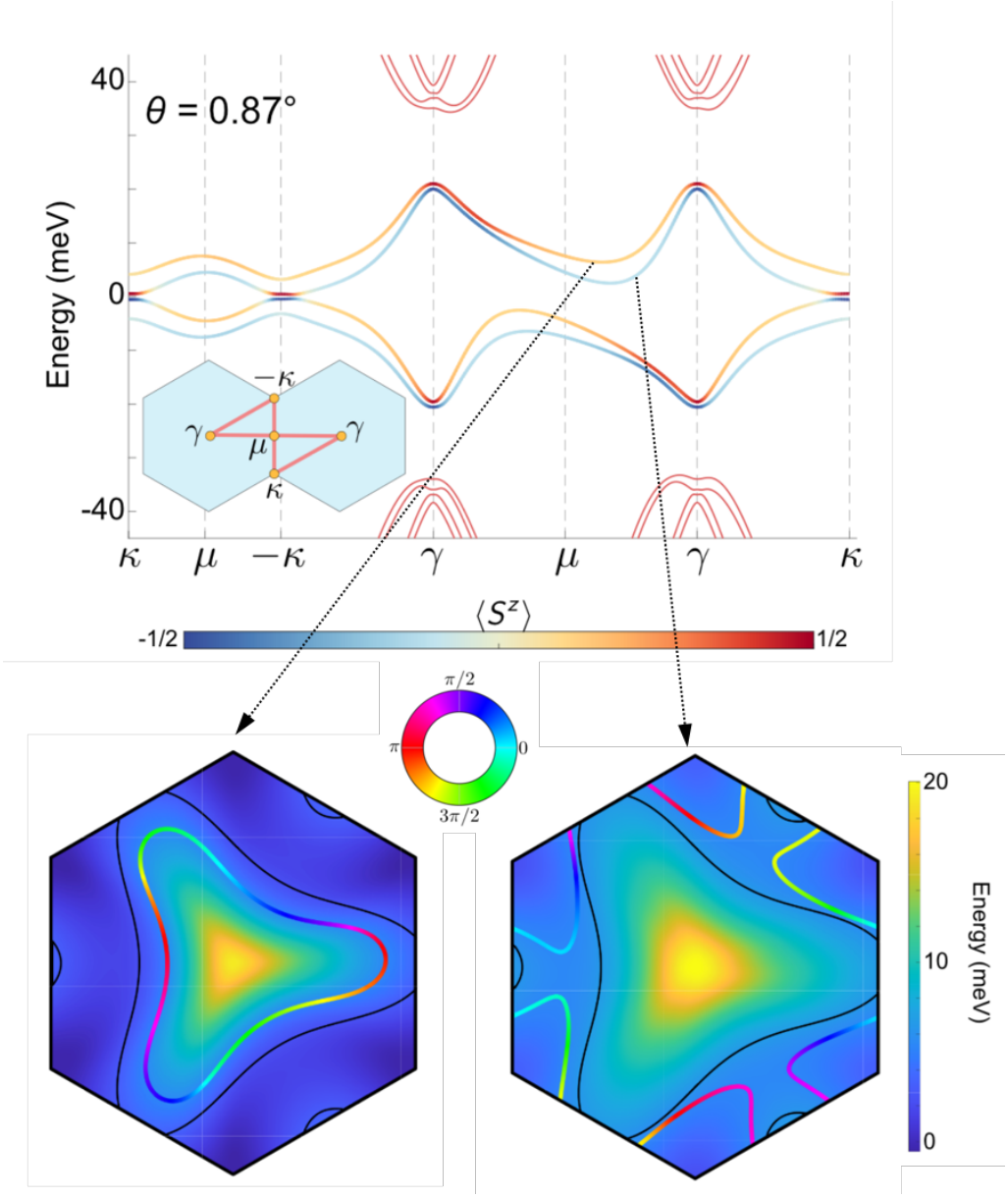

Figure 3.23: Continuum model simulations with and without considering the effects of spin-orbit coupling on the low energy bandstructure of TBG.

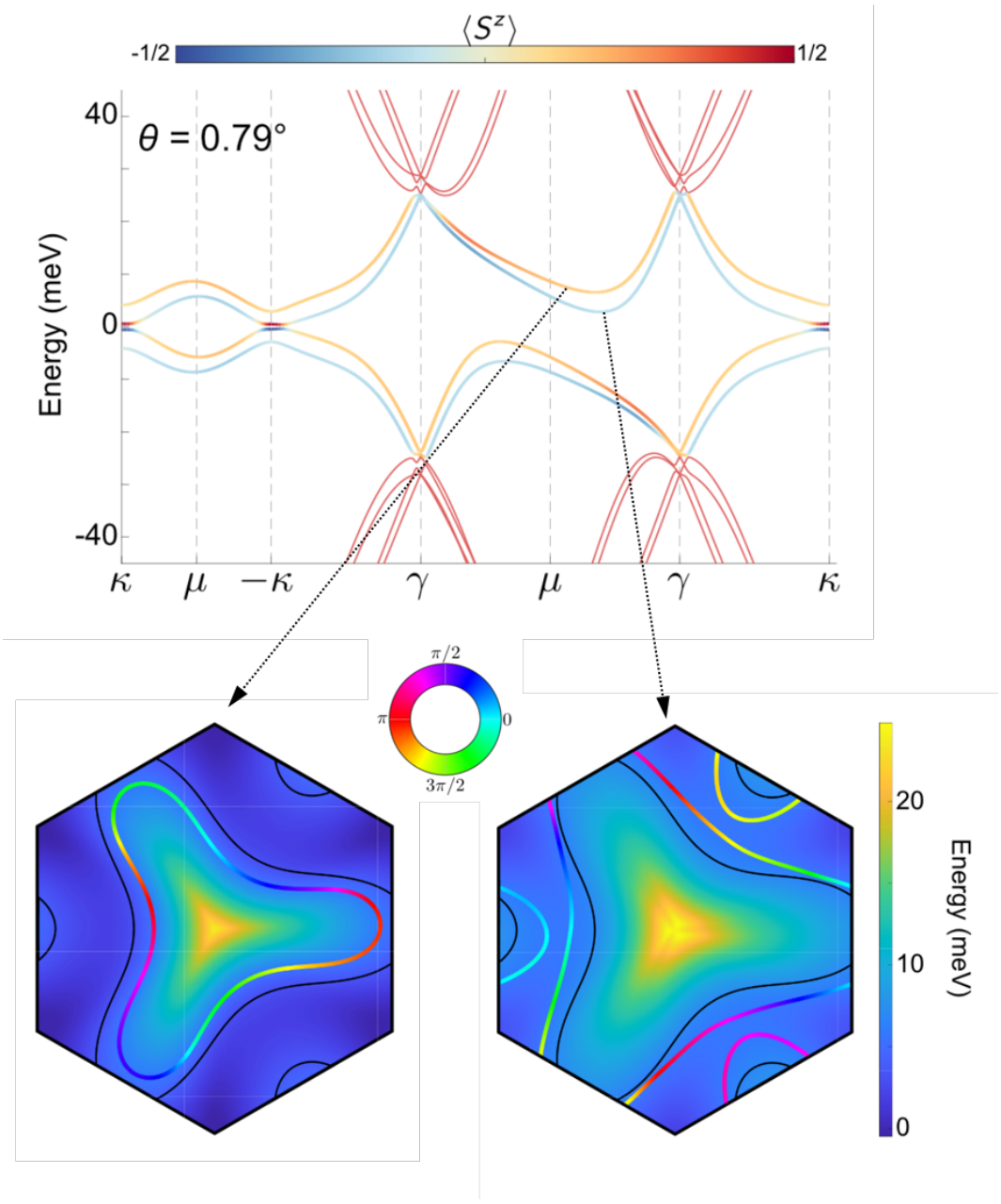

Figure 3.24: Continuum model simulations with and without considering the effects of spin-orbit coupling on the low energy bandstructure of TBG.

here.

Twisted bilayer graphene without spin orbit coupling

We briefly turn away from the question of spin orbit to provide a short overview of the continuum model [125, 72] of twisted bilayer graphene with twist angle θ. It is sufficient to specify to states proximate to the $+\boldsymbol{K}$ valley (*i.e.* $\tau^z = +1$). We let ψ_t (ψ_b) represent the electron annihilation operator of top (bottom) layer. The model Hamiltonian may be expressed as

$$H_{\text{cont}} = H_t + H_b + H_{\text{tun}}. \tag{3.7}$$

The first two terms on the left-hand side respectively denote the Dirac Hamiltonian of the top and bottom layers in the absence of tunnelling:

$$H_{t/b} = \int_{\boldsymbol{k}} \psi^\dagger_{t/b}(\boldsymbol{k}) h_{t/b}(\boldsymbol{k}) \psi_{t/b}(\boldsymbol{k}), \tag{3.8}$$

where

$$h_t(\boldsymbol{k}) = -v_0 e^{i\theta\sigma^z/4} \boldsymbol{k}\cdot\boldsymbol{\sigma} e^{-i\theta\sigma^z/4}, \qquad h_b(\boldsymbol{k}) = -v_0 e^{-i\theta\sigma^z/4} \boldsymbol{k}\cdot\boldsymbol{\sigma} e^{i\theta\sigma^z/4}. \tag{3.9}$$

As in Eq. (3.5), v_0 is the Fermi velocity of graphene. The layers tunnel through

$$H_{\text{tun}} = \sum_{\ell=1,2,3} \int_{\boldsymbol{k}} \psi^\dagger_t(\boldsymbol{k}) T_\ell \psi_b(\boldsymbol{k} + \boldsymbol{q}_\ell) + h.c., \tag{3.10}$$

where

$$\boldsymbol{q}_\ell = k_\theta \left(-\sin\left[\frac{2\pi}{3}(\ell-1)\right] \hat{\boldsymbol{x}} + \cos\left[\frac{2\pi}{3}(\ell-1)\right] \hat{\boldsymbol{y}} \right), \quad k_\theta = \frac{4\pi}{3a} 2\sin(\theta/2), \tag{3.11}$$

and

$$T_\ell = w_0 + w_1 \left(e^{-2\pi(\ell-1)i/3}\sigma^+ + e^{2\pi i(\ell-1)/3}\sigma^- \right). \tag{3.12}$$

Twisted bilayer graphene with induced spin orbit coupling

We now consider what occurs when a TMD is placed adjacent to one of the graphene monolayers that compose twisted bilayer graphene. Without loss of generality, we assume that the TMD touches the top layer. The sole modification to the continuum model presented in Eq. (3.7) occurs in H_t:

$$H_t = \int_{\boldsymbol{k}} \psi_t^\dagger(\boldsymbol{k}) \left(h_t(\boldsymbol{k}) + h_{t,\mathrm{SO}}\right) \psi_t(\boldsymbol{k}). \tag{3.13}$$

Here, $h_{t,\mathrm{SO}}$ represents the appropriately rotated projection of H_{SO} (Eq. (3.6)) onto the $+\boldsymbol{K}$ valley:

$$h_{t,\mathrm{SO}} = e^{i\theta\sigma^z/4}\left(\frac{\lambda_I}{2}s^z + \frac{\lambda_R}{2}\left(\sigma^x s^y - \sigma^y s^x\right) + \frac{1}{2}m\sigma^z\right)e^{-i\theta\sigma^z/4}. \tag{3.14}$$

Given the interfacial nature of the induced spin orbit effect, we do not expect the Hamiltonian of the bottom monolayer to be substantially altered (when TMD is only placed on one side).

Choice of model parameters and inter-layer hopping

The model calculations in Fig. 3.23 and Fig. 3.24 have been done using the following parameters: $(w_0, w_1) = (55, 105)\,\mathrm{meV}$; $(\lambda_I, \lambda_R) = (2, 10)\,\mathrm{meV}$; and $m = 0\,\mathrm{meV}$. The velocity of the graphene monolayers is left unaltered from the value provided above: $v_0 \sim 10^6\,\mathrm{m/s}$. This set of parameters both returns magic-angle values of $\theta = 1^\circ - 1.1^\circ$ and quantitatively reproduces the twist angle dependence of the gap on the electron side (within $30 - 50\%$). Our choice of w_0 deviates slightly from those reported in the literature [72, 126, 127, 128], but does not alter the magic angle value substantially, which is primarily controlled through w_1. The relative weakness of the w_0 used here compared to the values found in the literature may be ascribed to the greater importance of lattice relaxation at smaller twist angles. The values of Ising and Rashba spin-orbit coupling chosen here are in line with the existing literature [119, 121].

The choice to leave v_0 (t), w_1, and, as a result, the magic angle relatively unchanged compared to hBN-encapsulated TBG systems has been made for simplicity. In principle, the TMD could alter these parameters. For instance, Ref. [121] finds

that the nearest neighbor hopping energy t of the top graphene monolayer should be reduced to 2.5 eV from 2.6 eV (implying a reduction in v_0 on the top layer). Similarly, the presence of WSe_2 may also change the interlayer tunnelling parameters, w_0 and w_1. As the magic angle [72] is largely controlled through the parameter,

$$\alpha = w_1/(v_0 k_\theta) \propto w_1/(v_0\theta) \tag{3.15}$$

such modifications could shift the location of the magic angle. However, experimentally, we have observed correlated insulating states to be pronounced around 0.97°-1.04°, similar to the previous work [12] indicating that the magic-angle condition is not changed substantially. We note that screening effects which may be different due to WSe_2 may play a role in suppressing correlated insulating states [129, 130]. Also, we emphasize that the calculations displayed in Fig. 3.23 and Fig. 3.24 are phenomenological and that other effects such as TBG reconstruction may be important.

Chapter 4

NORMAL STATE CHARACTERIZATION AND MAGNETISM IN TBG/WSe_2 HETERO-STRUCTURES

We saw in the previous chapter how TBG behaves as a function of temperature and low field. Studying different phases in TBG under the application of perpendicular magnetic field provides a lot of information about the nature of symmetries involved and their breaking. We also saw in Chapter 2, how conductance can become quantized in 2D electron gases in high magnetic fields. We have observed quantized hall conductance in several devices which is remarkable, given that the angle disorder in TBG devices usually tends to wash out the quantization. To understand why this happens, let's try to re-frame the twist angle disorder as charge disorder. Around the magic angle value of 1.1°, the full filling carrier density value $n_{\text{full-1.1}} \approx 3\text{x}10^{12}/\text{cm}^{-2}$. The carrier density goes as square of the twist angle, so a twist angle of 1° results in $n_{\text{full-1}} \approx 2.48\text{x}10^{12}/\text{cm}^{-2}$. Therefore, for a usual TBG device with a twist angle disorder ≈ 0.1°, the difference in filling factors across the sample,

$$\nu_\delta = \frac{(n_{\text{full-1.1}} - n_{\text{full-1}})}{n_{\text{full-1.1}}} \approx 17\%$$

which is huge! The Quantum Hall phase is insensitive to the geometry of the device, and different Landau levels can be separated by energy gaps (0.1 meV to few meV at very high fields). If the variation of filling factors in the device is 17%, it means that the energy gaps separating the Landau levels need to be large (few meV) in order to experimentally observe quantization.

4.1 Behavior in high magnetic field and spin-orbit coupling

Measurements performed on longitudinal and transverse resistances in the presence of finite magnetic field reveal a lot of insights into the physics of TBG-WSe_2 structures. Surprisingly, for most of the devices fabricated and the ones shown here, we find that even at modest magnetic fields, above B = 1 T, gaps between Landau levels are well-resolved, showing a fan diagram that diverges from the charge neutrality (CNP). The slopes of the dominant sequence of R_{xx} minima correspond to even-integer Landau level fillings ±2, ±4, ±6, etc., indicating broken four-fold (spin and/or valley flavor) symmetry. By contrast, the majority of previous transport experiments [11, 80, 78, 131, 132, 102, 101] near the magic angle report a

Landau-fan sequence ±4, ±8, ±12 at the CNP, with broken-symmetry states being only occasionally observed at the lowest Landau level (corresponding to the ±2 sequence) [13, 78, 131]. Note also that for the smallest angle ($\theta = 0.79°$), we do not observe obvious signatures of correlated insulating states near $\nu = 2$ up to $B = 4$T.

The observation of additional Landau levels is consistent with a scenario in which the TBG band structure is modified by the spin-orbit interaction (SOI) inherited from the WSe_2 monolayer. Previous works established that WSe_2 can induce large SOI of both Ising and Rashba type into monolayer and bilayer graphene [15, 46], and it is therefore reasonable to assume that the same type of SOI is similarly generated in the upper (proximitized) layer of TBG. The presence of SOI can be independently verified in our devices by the observation of a conductance peak at B = 0 mT, indicative of weak anti-localization [47] and consequently the presence of strong SOI (see Fig. 4.12 and Fig. 4.13. Continuum-model calculations (Fig. 3.21) taking into account this effect show that the SOI lifts the degeneracy of both flat and dispersive bands, thereby breaking four-fold spin-valley symmetry. In a finite magnetic field, the resulting Landau levels then descend from Kramer's states that are only two-fold degenerate. We emphasize that the fan diagram has been reproduced in multiple samples; including a device with WSe_2 on both the top and bottom (D4, 0.80°, Fig. 4.8, which also shows a very similar temperature dependence to the 0.79° area in D2). The latter observation indicates that mirror symmetry breaking by WSe_2 placed on only one side of the TBG does not account for the observed degeneracy lifting. Odd steps, which are not generated by the SOI, are occasionally observed for low angles.

We attribute these steps to additional symmetry breaking, possibly due to correlation effects originating either from flat-band physics or simply a magnetic-field-induced effect (due to, for example, the Zeeman effect or exchange interaction) at low electronic densities. Full explanation of the odd Landau levels and the apparent recurrence of 4-fold degeneracy for large Chern number, ν_{LL}, (±14, ±18, ±22, which are still offset from the usual sequence: ±16, ±20, ±24; Fig. 4.2, Fig. 4.3 and Fig. 4.1) require further study. However, the mechanism of SOI-induced degeneracy breaking remains the simplest explanation for the observation of the additional even Landau levels (see corresponding discussion in section on Landau level calculations and Fig. 3.22).

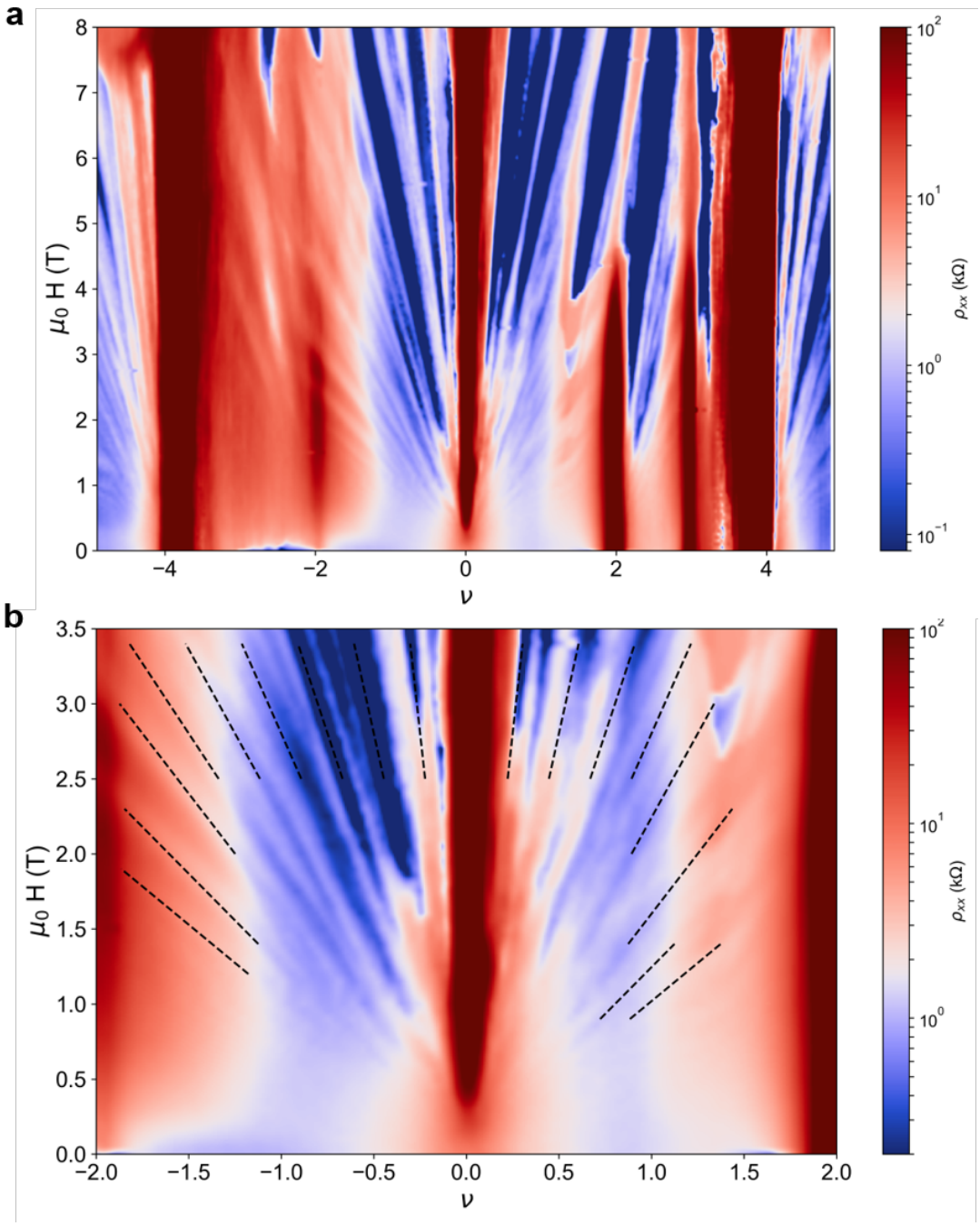

Figure 4.1: Longitudinal resistance (R_{xx}) as a function of field for device D1 (0.97°). **a)** Full Landau fan up to 8T exhibiting Landau levels emanating from different filling factors +1,±2,+3. **b)** Zoom-in around the Charge Neutrality Point (CNP), dotted lines are drawn from the charge neutrality point according to the sequence ν_{LL} = ±2, ±4, ±6, ±8, ±10, ±12, ±14, ±18, ±22.

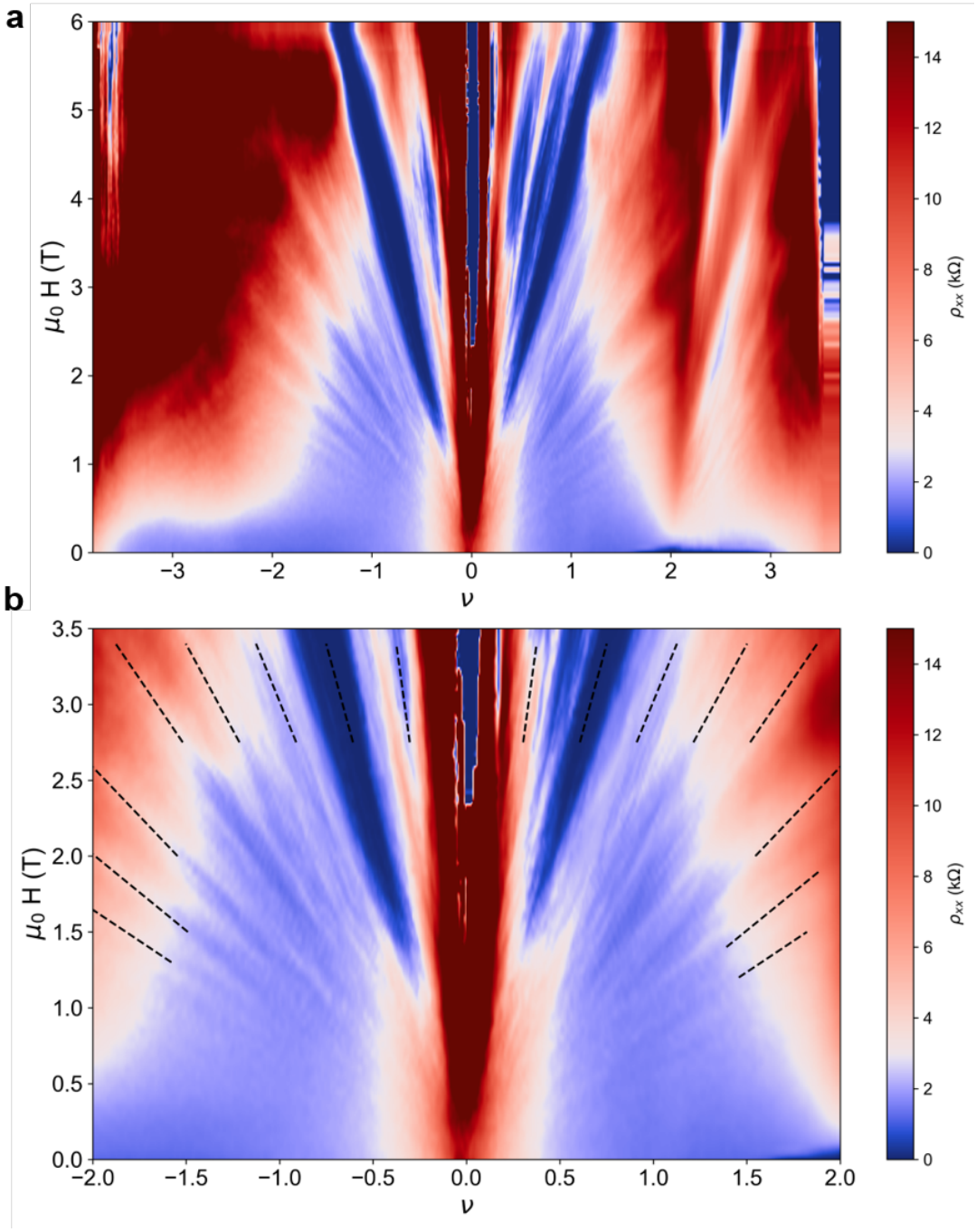

Figure 4.2: Longitudinal resistance (R_{xx}) as a function of field for device D2 0.87° area. **a)** Full Landau fan up to 6T exhibiting Landau levels emanating from Charge Neutrality Point (CNP) and half-filling (+2). **b)** Zoom-in around CNP, dotted lines are drawn from the charge neutrality point according to the sequence ν_{LL} = ±2, ±4, ±6, ±8, ±10, ±12, ±14, ±18, ±22.

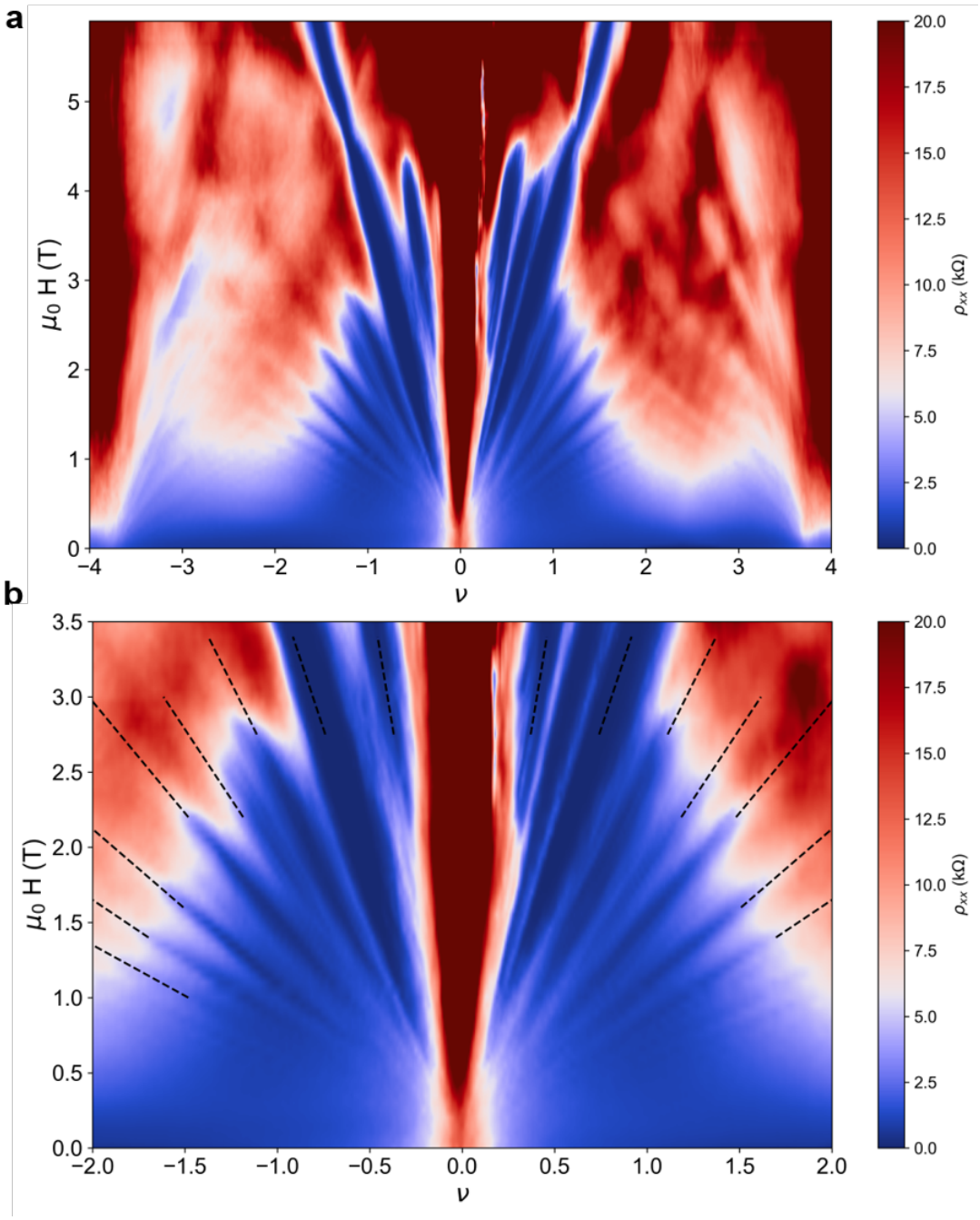

Figure 4.3: Longitudinal resistance (R_{xx}) as a function of field for device D2 0.79° area. **a)** Full Landau fan up to 6T, note the complete absence of any correlated insulating states around half-filling. **b)** Zoom-in around Charge Neutrality Point (CNP), dotted lines are drawn from the charge neutrality point according to the sequence ν_{LL} = ±2, ±4, ±6, ±8, ±10, ±12, ±14, ±18, ±22.

4.2 Quantized Landau Levels

In addition to R_{xx} minima corresponding to the gaps between Landau levels, we also measured quantized Hall conductance plateaux, further corroborating the two-fold symmetry in our TBG/WSe_2 devices. Interestingly, the conductance plateaux emerge at fairly low fields of 1-1.25T and are consistently visible in multiple devices. Even the most uniform devices reported in literature [78] (based on twist angle uniformity) do not show this feature, which could indicate higher twist angle uniformity on a microscopic scale in our devices. It is also unclear if spin-orbit plays any role in this and would be interesting to study further.

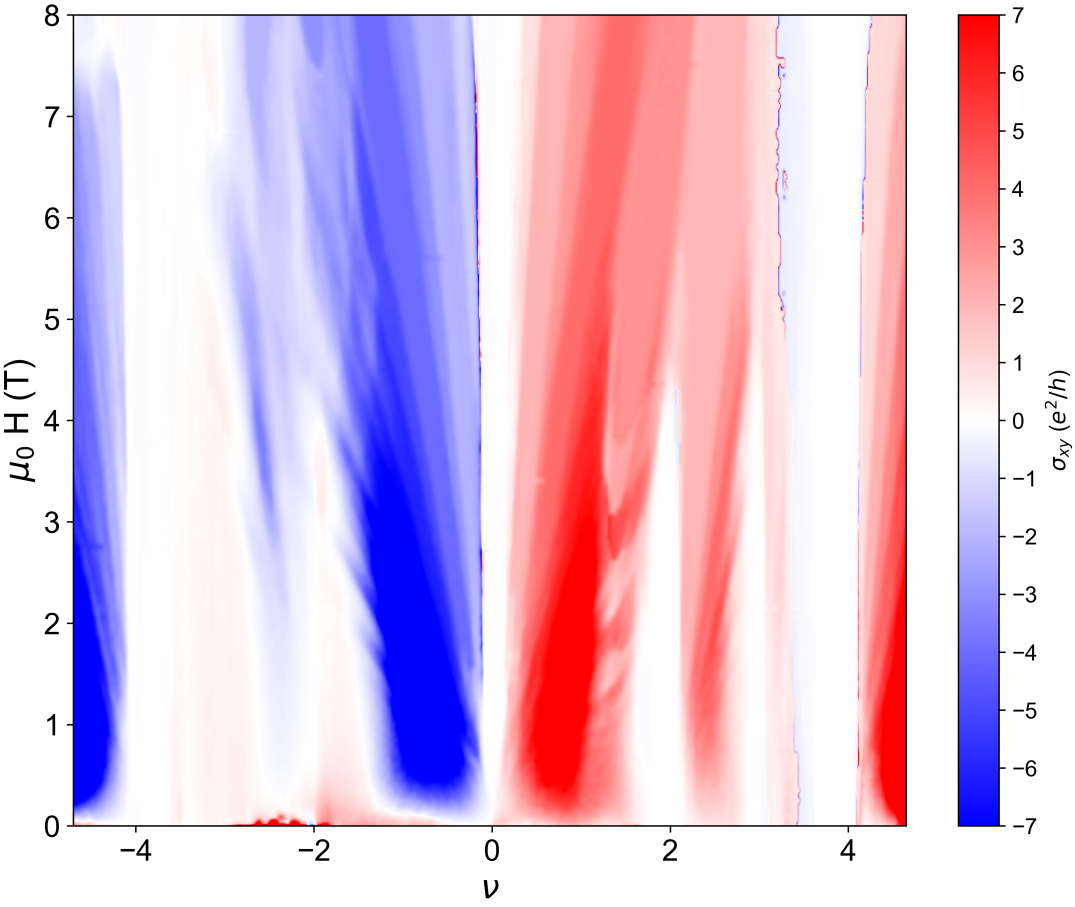

Figure 4.4: Transverse conductance (for device D1, 0.97°) (σ_{xy}) as a function of field up to 8T showing conductance plateaux as a result of the Quantum Hall effect. At high fields, the conductance follows and unconventional sequence of e^2/h, $e^2/2h$, $e^2/3h$, $e^2/4h$, $e^2/3h$, $e^2/2h$, e^2/h.

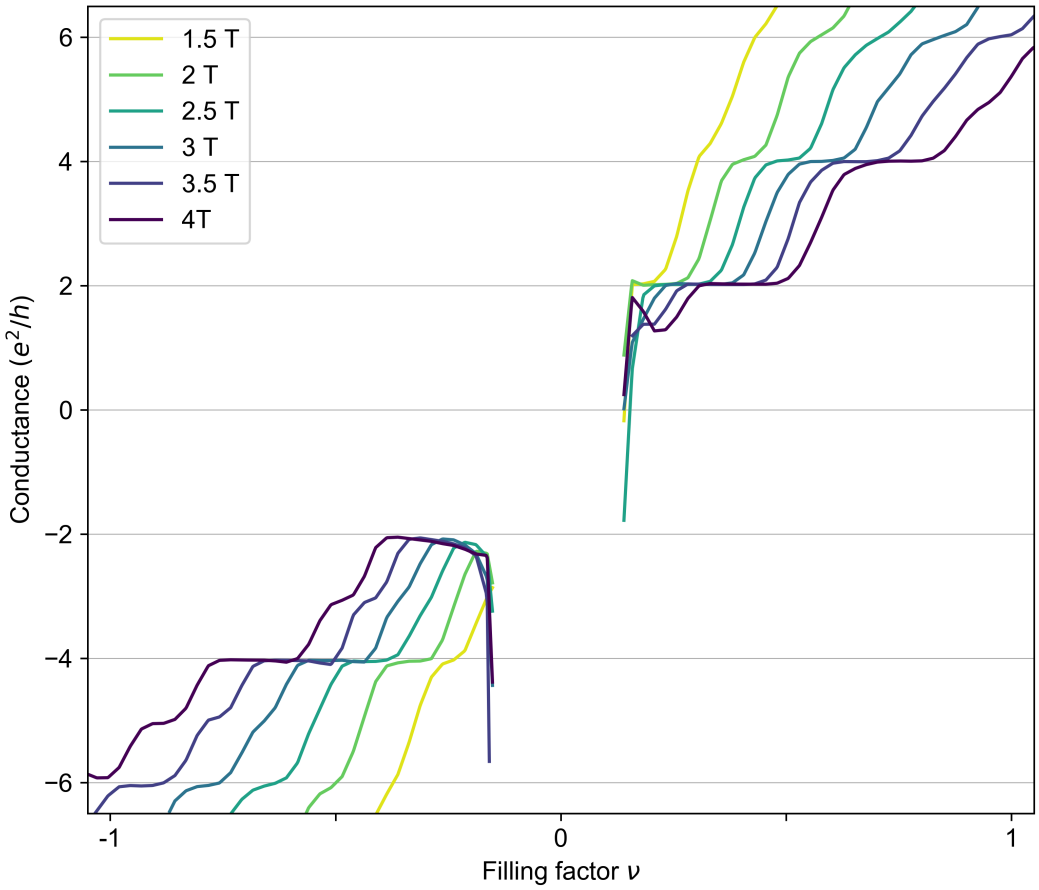

Figure 4.5: Line cuts (for device D1) around charge neutrality point showing the 4-fold symmetry breaking with pronounced steps for $e^2/2h$, $e^2/4h$, $e^2/6h$ due to induced spin-orbit interaction. The occasional odd step is most likely due to further symmetry breaking by electronic correlations.

4.3 Determination of twist angle

Since a lot of the physics described in this thesis depends on the definition of the angle of rotation between the two graphene layers, it is important to talk about how we determine the twist angle in our devices. The most common way of determining the angle is by using the Landau Fan diagram (the R_{xx} component specifically). As a first step, we locate the R_{xx} minima. By extrapolating multiple Landau level minima around charge neutrality to a point in a gate space where they all intersect, we obtain the backgate voltage. A similar procedure gives us the half- or full-filling voltage. Using this, and the fact that the slope of the Landau fan is directly proportional to the capacitance, the electron density at full filling (n_{full}) can be obtained. From the

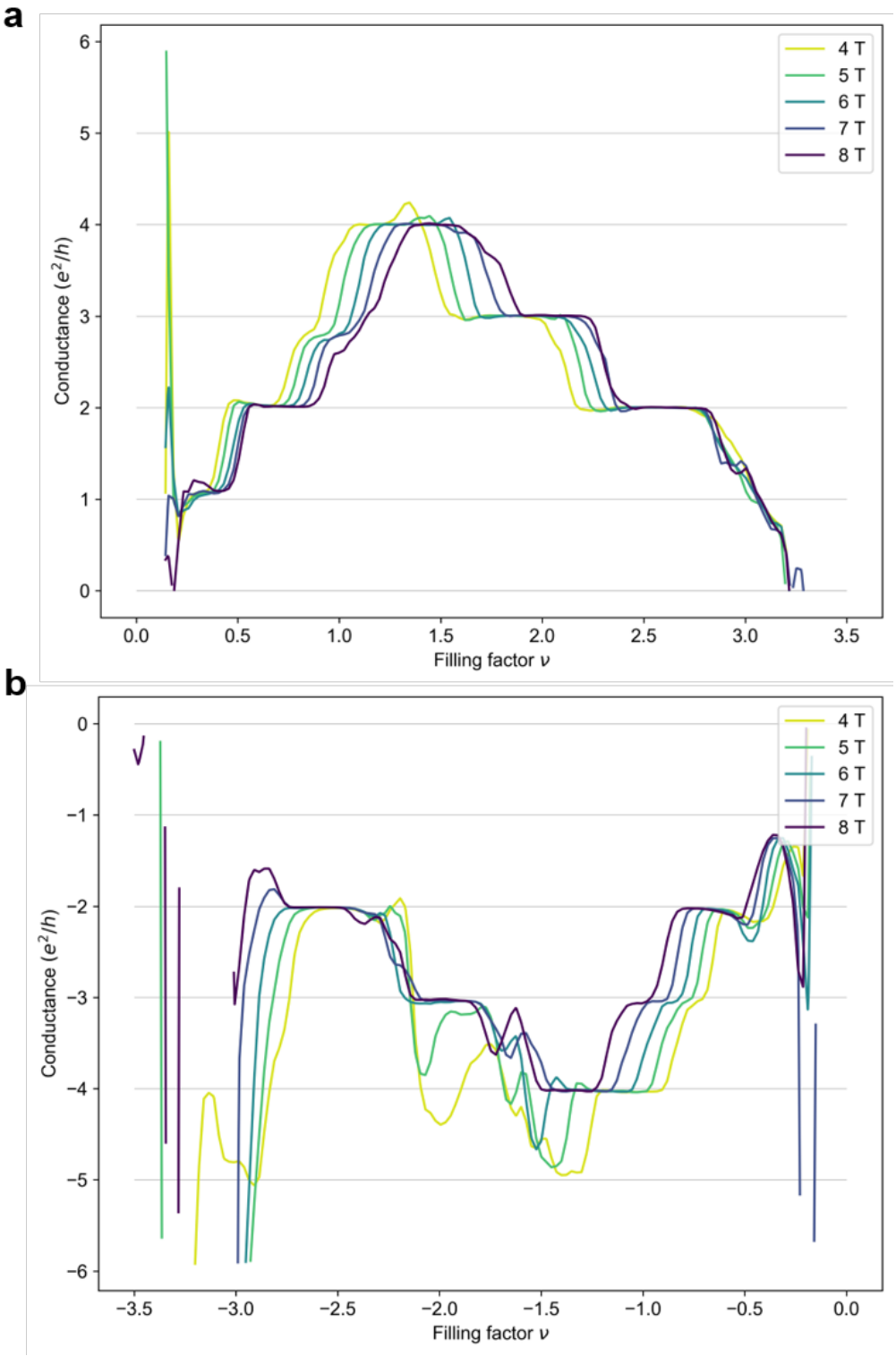

Figure 4.6: Line cuts (for device D1) showing quantization of σ_{xy} at high fields **a)** for electrons **b)** for holes. It is clear from these cuts that the conductance follows an unconventional sequence of $+(-)e^2/h$, $+(-)e^2/2h$, $+(-)e^2/3h$, $+(-)e^2/4h$, $+(-)e^2/3h$, $+(-)e^2/2h$, $+(-)e^2/h$ for electrons(holes).

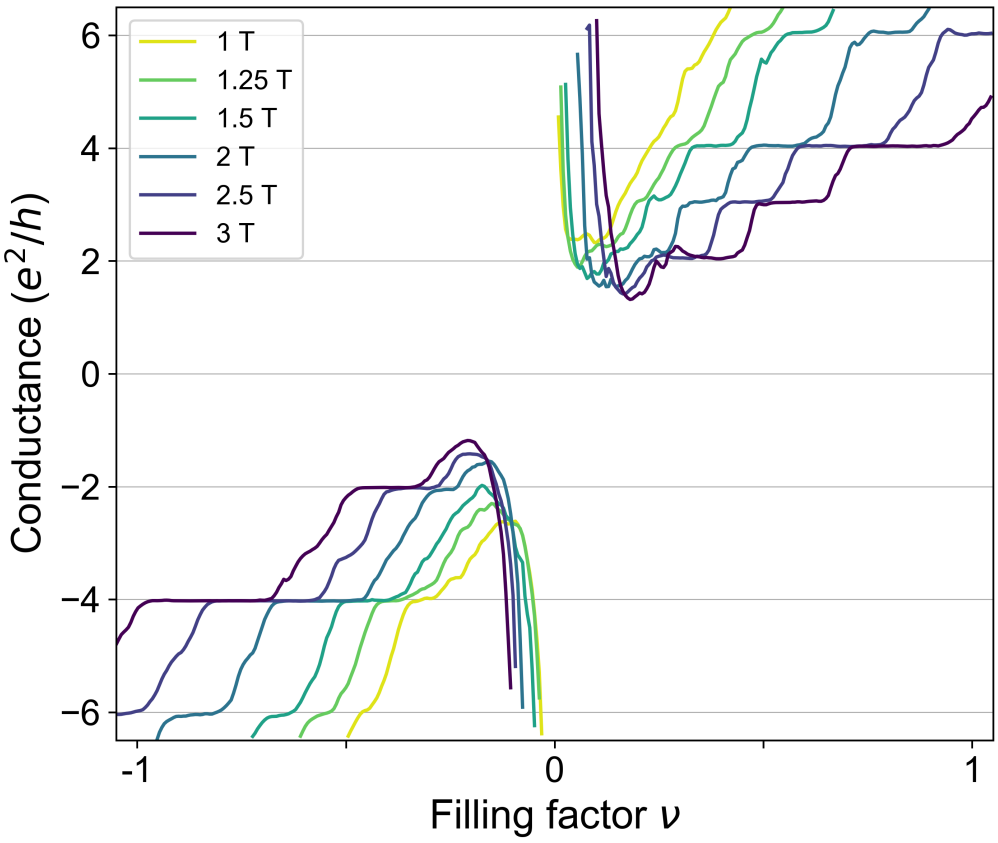

Figure 4.7: Line cuts (for device D2, 0.79°) around charge neutrality point showing the 4-fold symmetry breaking with pronounced steps for $e^2/2h$, $e^2/4h$, $e^2/6h$ due to induced spin-orbit interaction. The occasional odd step is most likely due to further symmetry breaking by electronic correlations.

density, the twist angle is calculated using the low-angle approximation,

$$\theta^2 \approx \sqrt{3}a^2 n_{\text{full}}/8 \tag{4.1}$$

where $a = 0.246$ nm is the lattice constant of graphene [12]. The conversion from backgate voltage to filling factor ν (or electrons per Moiré unit cell) is then a linear transformation, where the electron(hole) full filling voltage corresponds to $\nu = +(-)4$. The twist angle determination using this method is accurate to ±0.01°.

Another independent method to crosscheck the angle is to the use Hofstadter butterfly physics, which highlights what happens to electrons subjected to a perpendicular magnetic field in a periodic spatial potential. In this model, Landau levels originating from different filling factors intersect periodically in the fan diagram, giving rise to a recursive structure of Landau levels at high fields (butterfly structure). Experimentally, this can also lead to distinctly periodic horizontal features in the

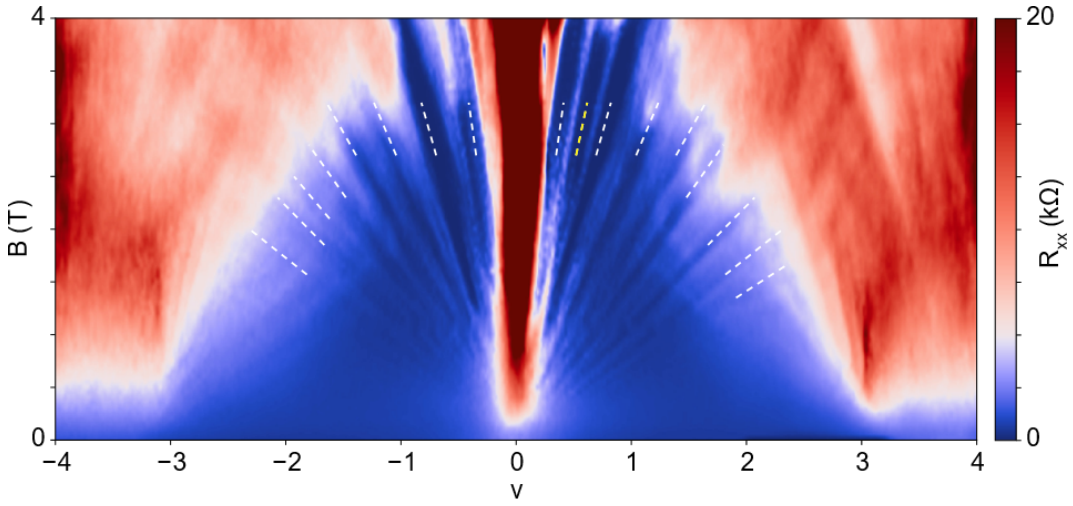

Figure 4.8: Data for device D4. Dotted lines are drawn from the charge neutrality point according to the sequence $\nu_{LL} = \pm 2, +3, \pm 4, \pm 6, \pm 8, \pm 10, -12, \pm 14$, etc., with the odd level (+3) marked in yellow.

fan diagram [37] as represented in Fig 4.9. The periodicity of these features corresponds to the magnetic fields where an integer number of flux thread through each moiré unit cell. Assuming the area of the moire superlattice unit cell is A and the flux quantum is $\phi_0 = h/e$ [133], features should appear at fields that correspond to B_{full}/n and n*B_{full} where n is an integer. By observing horizontal lines, we can estimate B_{full} by finding the least common integer multiple of the fields at which the lines emerge. The moiré wavelength can then be obtained as follows:

$$\phi_0 = B_{\text{full}} \times A = B_{\text{full}} \times \frac{\sqrt{3}\lambda^2}{2} \tag{4.2}$$

where λ is the superlattice unit length. For the case of Fig. 4.9, because lines appear at approximately 4.1625T, 3.33T, 2.775T and so on, and the least common integer multiple is found to be 16.65T. Therefore,

$$2.0625 \times 10^{-15} = 16.65 \times \frac{\sqrt{3}\lambda^2}{2} \tag{4.3}$$

giving us a λ of 16.9 nm which means,

$$cos^{-1}(\theta) = 1 - 0.5 \times (16.9^2/0.246^2) \tag{4.4}$$

confirming our angle of 0.834° obtained by finding the full filling in gate space.

It is important to point out here that we don't observe the Zak-type oscillations for most of the pairs of contacts/devices that we measure. It is unclear why this feature,

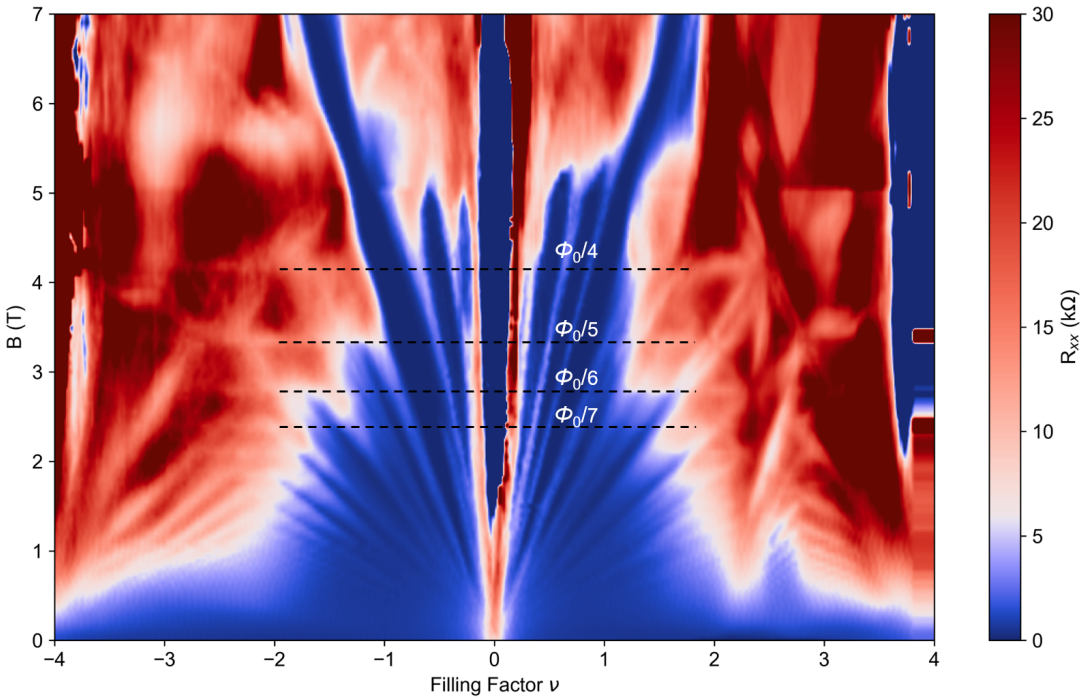

Figure 4.9: Hofstadter's butterfly and Zak-type oscillations in the 0.83° area of device M20, measured at 50mK. B_{full} is approximately 16.65T in this case.

which is present without any correlations in h-BN graphene superlattices is present only in this area (given that we have measured angles both smaller and larger than this). As we saw earlier, this is the same pair of contacts (the only one we have seen this effect in) that shows a 0-π junction behavior which suggests that they could be linked somehow. It is possible that a combination of moiré wavelength at this angle (0.83°) and doping at the contacts is responsible for this effect.

4.4 Evidence for induced spin-orbit coupling in TBG

As we mentioned in Chapter 2, Weak Anti-Localization (WAL) has been used as a proof of induced spin-orbit coupling in graphene. Here, we will discuss WAL measurements that we've done in our system of TBG to independently establish the existence of spin-orbit coupling (in addition to four-fold symmetry breaking near charge neutrality in the Landau fan diagram). Because the modeling of induced spin-orbit in TBG is much more complex than induced spin-orbit coupling in graphene, we will discuss some nuances associated with fitting the WAL peak for our data.

Weak Localization (WL)

To understand the role of spin-orbit coupling in weak anti-localization, we need to first take a look at the physics of weak localization, both of which are phase coherent processes that are a manifestation of the wavelike nature of electrons. In the presence of disorder at very low temperatures, electrons can experience enhanced backscattering, leading to a increase in resistivity compared to the one calculated using the classical Drude model. When the disorder is high enough, the system can become an insulator as pointed out in a seminal work by Anderson [134].

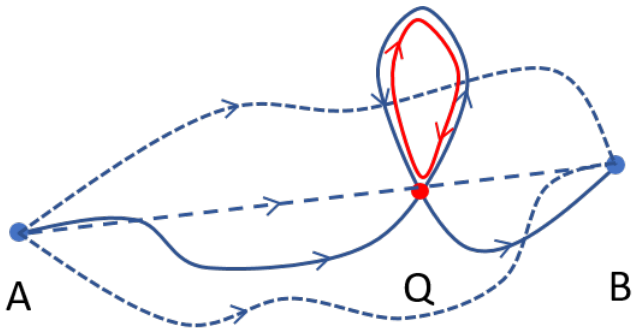

Figure 4.10: Path of an electron going from point A to B. Weak localization stems from the quantum mechanical treatment of the probability of the electron returning to some point Q.

Considering an electron traveling from point A to point B (as shown in Fig. 4.10), with several possible paths, the probability that it reaches B starting at A is given by

$$P_{AB} = |\sum_i A_i|^2 = \sum |A_i|^2 + \sum_{ij} |A_i A_j| \tag{4.5}$$

The first term corresponds to the classical contribution, and the second term is a quantum interference term arising purely due to a quantum mechanical origin. For the case of two different points (A and B),

$$< \sum_{ij} |A_i A_j| >= 0$$

due to disorder averaging; this, however, is not valid for the case of time-reversed paths. To simplify, we look at two paths of returning to the same point Q in the middle. At zero magnetic field, time reversal symmetry requires

$$A_1 = A_2 = A_0$$

$$P_{AB} = |A_1|^2 + |A_2|^2 + 2Re|A_1A_2| = 4|A_0^2| \tag{4.6}$$

This increased probability of returning to the same point (localization) *increases* the resistivity of the material. Notably, the quantum correction is exactly equal to the classical contribution and doubles the expected resistivity. This is the correction induced due to Weak Localization(WL). Why is it weak? Because as we will see soon, it is extremely susceptible to magnetic field.

Since the quantum correction is exactly equal to the classical contribution, we can simplify the quantum correction using a classical model as described in Ref. [135]. The quantum correction can be written as,

$$\frac{\Delta\sigma}{\sigma} = -\frac{1}{k_f l_e} ln \frac{\tau_\phi}{\tau_e} \tag{4.7}$$

where τ_ϕ is the decoherence time for the phase of the electron, τ_e is the elastic scattering time, k_f is the Fermi wavevector, and l_e is the elastic scattering length. The decoherence time (τ_ϕ) for two dimensions depends on temperature with a power law

$$\tau_\phi \propto \frac{\hbar}{k_B T^p} \tag{4.8}$$

Therefore, assuming the elastic scattering time (τ_e) doesn't change too much with temperature, the contribution due to Weak Localization decreases on increasing the temperature, which has been observed experimentally for several 2-D systems [136, 137, 138]. This effect totally disappears when $\tau_\varphi \approx \tau_e$ making it difficult to observe in ballistic systems with ultra-high mobilities and long τ_e.

Dependence of WL on magnetic field

While the red and black loops around point Q in Fig. 4.10 interfere constructively in the absence of a magnetic field, they become unequal in the presence of magnetic flux piercing the loop because the Aharonov-Bohm phase given by

$$\varphi_{AB} = 2\pi \frac{BS}{h/e} \tag{4.9}$$

where S is the area of the two loops. This phase modifies the wavefunctions accordingly,

$$A_{1,2}(AB) = A_0 e^{\pm i\varphi_{AB}} \tag{4.10}$$

Eq. 4.6 then becomes,

$$|A_1 + A_2|^2 = 2|A_0|^2 + 2|A_0|^2 \cos 4\pi \frac{BS}{h/e} \tag{4.11}$$

This would imply a $h/2e$ modulation of the quantum correction to the scattering probability. Considering many different scatterers and several different time-reversed paths, this modulation should average out to zero. For the special case of $B = 0$ however, the contribution remains +1 regardless of the area of the different time-reversed paths; all of the paths have the same phase very close to zero field. Therefore, the resistance should be a maximum at zero field and should decrease gradually in positive or negative field as depicted in Fig. 4.11.

Weak Anti-Localization (WAL)

In systems with strong spin-orbit coupling, the spin of a electron is locked to the momentum – such that when an electron is scattered, its spin is also altered. The timescale which governs the complete randomization of spin due to such scattering events in a spin-obit coupled system is denoted by τ_{SO}. When $t << \tau_{SO}$, the initial direction of the spin is preserved, wheareas for $t >> \tau_{SO}$, the spin is completely randomized. This leads to an interesting change in the WL quantum correction as shown by Hikami *et al.* [139] and Bergmann *et al.* [140] Here we show a few key steps from the excellent qualitative treatment described in Ref. [135]. We begin by a spinor term $|s\rangle$ to the initial wavevector and look at its evolution with scattering. If the electron rotates clockwise, its new spin (on the Bloch sphere) can be written as,

$$|s'\rangle = R\,|s\rangle \tag{4.12}$$

and for the counterclockwise rotation,

$$|s''\rangle = R'\,|s\rangle \tag{4.13}$$

where R and R' are rotation operators which can be described by using Euler angles (α, β, γ) as,

$$R(\alpha,\beta,\gamma) = \begin{pmatrix} \cos\frac{\alpha}{2}e^{i(\beta+\gamma)/2} & i\sin\frac{\alpha}{2}e^{-i(\beta-\gamma)/2} \\ i\sin\frac{\alpha}{2}e^{i(\beta-\gamma)/2} & \cos\frac{\alpha}{2}e^{-i(\beta+\gamma)/2} \end{pmatrix} \tag{4.14}$$

In general, the matrix rotation operator has to be unitary and is comprised of infinitesimal unitary rotation matrices. Therefore, for two time-reversed paths, we can write the interference contribution as

$$(\langle s'| + \langle s''|)(|s'\rangle + |s''\rangle) = 2 + \langle s'|s''\rangle + \langle s''|s'\rangle \tag{4.15}$$

The first term (2) again is the classical contribution, and the second one is the quantum correction. The second term can be simplified as,

$$\langle s'|s''\rangle = \langle Rs|R's\rangle = \langle s|R^2|s\rangle \tag{4.16}$$

Now if the spin-orbit coupling is strong enough that the spin fully forgets its initial state after a few scattering events, then we need to calculate the average expectation value for R^2 to determine the quantum correction. Assuming that $|s\rangle$ is a two component vector, (a,b),

$$\langle s|R^2|s\rangle = (a,b)R^2(a,b)^T = \cos^2\frac{\alpha}{2}(e^{i(\beta+\gamma)|a|^2} + e^{-i(\beta+\gamma)|b|^2}) - \sin^2\frac{\alpha}{2} + \frac{i}{2}\sin\alpha(ab^*(e^{-i\beta} + e^{i\gamma}) + a^*b(e^{i\beta} + e^{-i\gamma})).$$

If we average this expression over several scattering events, the only term that survives is $-\sin^2\frac{\alpha}{2}$ with an expectation value of -1/2. Therefore, the quantum correction in total is $-1/2 + -1/2 = -1$ which is exactly half the magnitude of the weak localization correction with an opposite sign. Here we see that the quantum correction causes a decrease in resistivity and an increase in conductance, which is opposite to the case of WL.

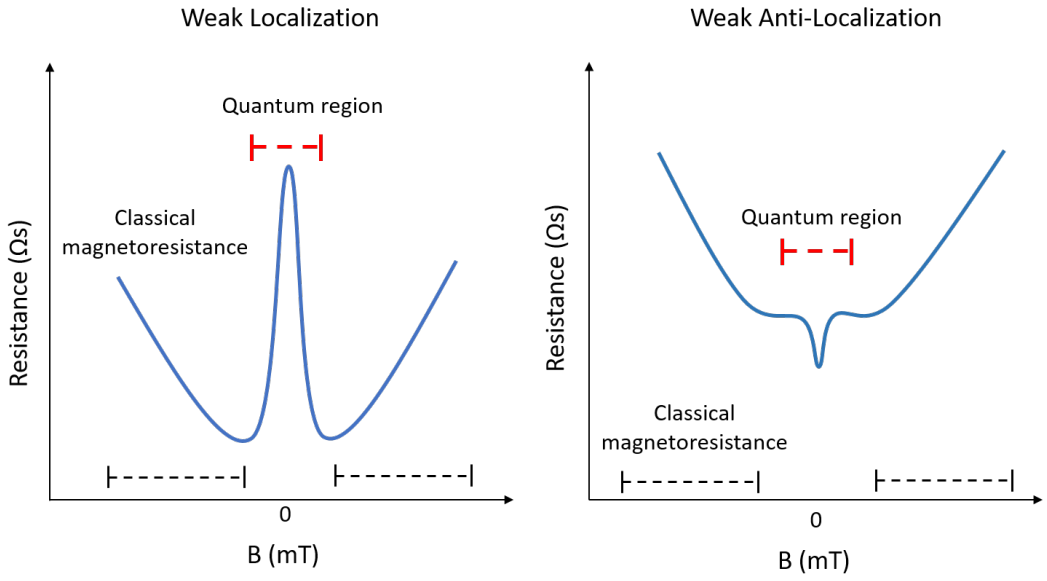

Figure 4.11: Comparison between weak localization (WL) and weak anti-localization (WAL). WL shows a peak (dip) in resistance (conductance) at zero magnetic field, and WAL shows a dip (peak) in resistance (conductance) at zero magnetic field.

Weak Anti-Localization measurements in TBG

Tikhonenko *et al.*[141] provide a good overview of weak anti-localization for graphene before the transition to h-BN as a substrate (i.e. more disorder from SiO_2 but possibly similar physics). They mention a theory paper Ref. [142] that

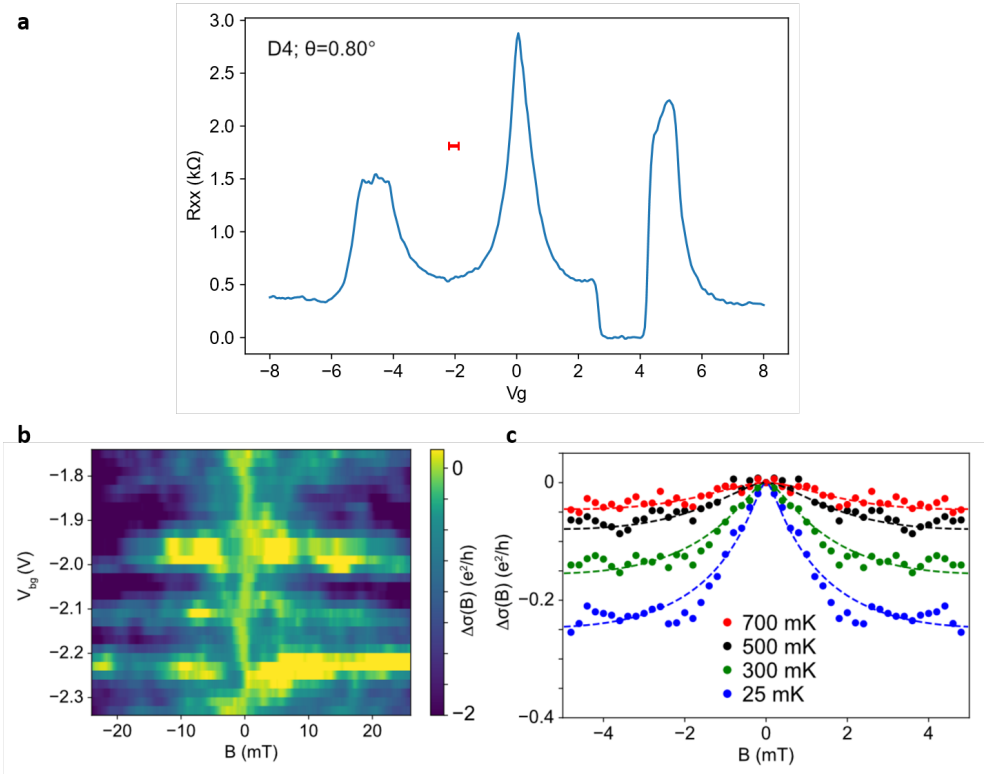

Figure 4.12: Weak Anti-Localization measurements in the flat band. **a)** Resistance as a function of gate voltage for device D4 (0.80° angle) the gate voltages where the data was taken marked in red.

suggests graphene should support WAL because of the chiral nature of the Dirac electrons. However, weak localization returns due to inter-valley scattering and atomically sharp scatterers such as edges and impurities. In SiO_0, weak localization was largely the observation. However, WAL was observed by [141] by increasing the temperature and lowering the carrier density (just near the Dirac point). In our case, the WAL gets stronger as we go lower in temperature, so we can rule this explanation out.

For good papers on the strong spin-orbit coupling induced in graphene by proximity to TMDCs (version of WAL theory), it is instructive to look at Refs. [49] and [45] (they provide more information on interesting things you can pull out from data). Their original theory is from Maccann and Fal'ko [143].

The parameters of the model used for fitting the WAL peak are D, the diffusion coefficient (for ML graphene, this comes from $v_F^2\tau/2$, where the elastic scattering time τ is calculated from mobility, and v_F is the graphene Fermi velocity $\sim 10^6$ m/s in ML graphene); τ_ϕ, the dephasing (inelastic scattering) time; and two elastic

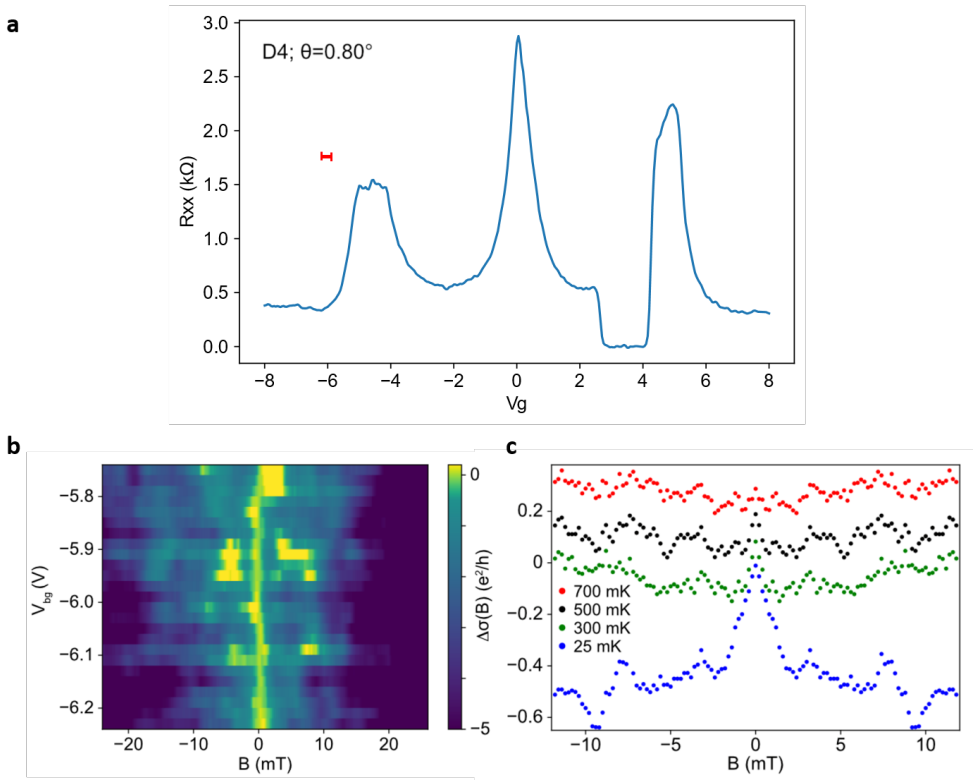

Figure 4.13: Weak Anti-Localization measurements in the dispersive band. **a)** Resistance as a function of gate voltage for device D4 (0.80° angle) the gate voltages where the data was taken marked in red.

scattering times: τ_{asy}, which seems to be related to either intervalley scattering or scattering that results from breaking z $\rightarrow$ -z symmetry and τ_{so}, which combines asymmetric and symmetric scattering ($\tau_{so}^{-1} = \tau_{asy}^{-}1 + \tau_{sym}^{-1}$, where the τ_{asy} and τ_{sym}. The τ_{so} and τ_{asy} terms come from Ref. [49], where the authors describe them as being the total SOC scattering and the asymmetric scattering due to breaking the plane symmetry.

The equation,

$$\Delta\sigma(B) = -\frac{e^2}{2\pi h}\left[F\left(\frac{\tau_B^{-1}}{\tau_\phi^{-1}}\right) - F\left(\frac{\tau_B^{-1}}{\tau_\phi^{-1} + 2\tau_{asy}^{-1}}\right) - 2F\left(\frac{\tau_B^{-1}}{\tau_\phi^{-1} + \tau_{so}^{-1}}\right)\right] \tag{4.17}$$

where $F(x) = ln(x) + \psi(0.5 + x)$, ψ is the Digamma function, and $\tau_B^{-1} = 4eDB/\hbar$ (The factor of 1/2 out front is not there in Ref. [49], but it's likely a typo. This is the original expression and is in Refs. [143, 144]). Another consistency check in our data is that the magnitude of WAL is about half the magnitude of WL based on

the derivation in Ref. [135].

This equation looks very similar to that used by Tikhonenko *et al.* [141], where they were looking at a weak-localization-dominant picture, with different scattering times: τ_i is the inter-valley scattering time, which apparently can result from scatterers that also break time-reversal symmetry (according to Ref. [145] on graphene/hBN, where they use the same equation), and τ_*, which is the intra-valley scattering parameter. (For the equation above, it is suggested in Ref. [45] that it is only relevant when the inter-valley scattering is stronger than the phase coherence relaxation rate.)

$$\Delta\sigma(B) = \frac{e^2}{\pi h}\left[F\left(\frac{\tau_B^{-1}}{\tau_\phi^{-1}}\right) - F\left(\frac{\tau_B^{-1}}{\tau_\phi^{-1}+2\tau_i^{-1}}\right) - 2F\left(\frac{\tau_B^{-1}}{\tau_\phi^{-1}+\tau_i^{-1}+\tau_*^{-1}}\right)\right] \tag{4.18}$$

The only difference in this equation is the positive sign out front and the factor of 1/2 is not present. It appears that whether it's weak localization or weak anti-localization, it's a very similar spin relaxation mechanism, but obviously the scattering times vary between being related to spin-orbit scattering and other forms of scattering. In our case, we use the equation with a negative sign out front. The second equation here describes the situation when there is not strong spin-orbit coupling (though it can describe weak forms of both WL and WAL, which is a bit complicated for graphene when you consider different temperatures and proximity to Dirac cones, as seen in Ref. [146])

For some intuition, the work of Tikhonenko *et al.* [141] gives us this (just remember that when their scattering parameters give them stronger WL, the scattering parameters in similar spots in our equation give us stronger WAL), : in the case of very low inter and intra-valley scattering ($\tau_*, \tau_i \rightarrow \infty$), the final term is the strongest. When the inter and intra-valley scattering is large, then the second and third terms get small, and the first term dominates, corresponding to localization. The reason Tikhonenko *et al.* were able to see WAL was because they raised the temperature (decreasing τ_ϕ) and lowered the carrier density (increasing τ_i), and the overall bonus of this was decreasing the ratios τ_ϕ/τ_i and τ_ϕ/τ_*. This picture can be further intuited by realizing that, for low z, $F(z) \approx z^2/24$. (Note that for the SOC case, the signs flip on these intuitive pictures.)

However, we're seeing WAL at the lowest temperatures, similar to papers where SOC is induced in ML graphene by proximity to TMDCs.

The other parameters used for the fit are the diffusion constant (D) and the momentum scattering (τ, or sometimes in papers τ_p):

$$D = \frac{v_F^2 \tau}{2} \tag{4.19}$$

This is taken to be T-independent, and in our case, v_F differs from ML graphene and is somewhere in the range of 10^5, approximately 10 times lower (according to our theoretical continuum models, and this looks a little larger than what was in Ref. [147] for magic-angle devices, so it seems consistent). However, we must consider that the flat bands can perhaps have a varying Fermi velocity depending on density, and that other models don't agree on the flatness of the bands. Using $v_F = \hbar k_F / m^* \rightarrow m^* = \hbar\sqrt{\pi|n|}/v_F$ and the standard Drude model, we can derive the momentum scattering time:

$$\sigma = \frac{ne^2\tau}{m^*} \tag{4.20}$$

$$\mu = \frac{\sigma}{ne} = \frac{e\tau}{m^*} = \frac{e\tau v_F}{\hbar\sqrt{\pi|n|}} \tag{4.21}$$

$$\tau = \frac{\mu\hbar\sqrt{\pi|n|}}{v_F e} = \frac{\hbar\sigma}{v_F e^2}\sqrt{\frac{\pi}{|n|}} \tag{4.22}$$

Using $\mu = \sigma/ne$ allows for τ to vary over the range of density, which is used in some papers. One perhaps difficult point for us is that the lower v_F in TBG leads to larger τ, and the standard picture of WAL and WL suggests that several scattering events happen before the phase coherence time τ_ϕ (though it can be similar to τ_{so}, which perhaps depends on the mechanism of spin-orbit coupling).

4.5 Landau level model calculations

The Landau level spectrum observed near the CNP in TBG encapsulated in BN sufficiently far from the magic angle is usually 8-fold symmetric [69, 148]. Closer to the magic-angle value, this 8-fold degeneracy is lifted, resulting in a 4-fold symmetric spectrum [12, 80]. In both cases, SOI effects do not play a dominant role. Here, we show that the Landau levels are heavily modified by SOI using a simple, low-energy model.

In the absence of a magnetic field and SOI, the spectrum obtained via the continuum model above contains two Dirac cones per **K**-valley per spin at the $+\kappa$ and $-\kappa$

points in the moiré Brillouin zone (see the inset of Fig. 3.21**a**). At low enough energies, the system may be described in terms of eight Dirac cones taking the same form as in Eq. (3.5) save that (i) the Pauli matrices $\sigma^{x,y,z}$ now act on the band indices of the operators Ψ ($\tau^{x,y,z}$ and $s^{x,y,z}$ still act on the **K** and spin flavor indices, respectively); (ii) there is an additional flavor index given by the moiré valley, $\pm\kappa$; and (iii) the Fermi velocity has been substantially renormalized from the value found in monolayer graphene. Numerically, we find that the renormalized velocity is $v_F \approx 8.8 \times 10^4$ m/s at $\theta = 0.87°$ and $v_F \approx 1.1 \times 10^5$ m/s at $\theta = 0.79°$ for the model parameters described above.

Provided it is small enough that the Dirac description of TBG remains valid, the SOI may be included in a manner directly analogous to the approach we took above with monolayer graphene (i.e. H_{SO} defined in Eq. (3.6)). We note, however, that the spin-orbit parameters (λ_I, λ_R, m) are not prohibited from taking different values at the $\pm\kappa$ Dirac cones (the parameters at $\pm\mathbf{K}$ are related by time reversal). Nevertheless, we assume for simplicity that any differences in the effective parameters between κ-valleys is unimportant.

Without loss of generality, we therefore begin by considering the Dirac cone at $+\kappa$ with valley flavor $+\mathbf{K}$. According to the our approximations, this solution is equally valid for valley flavor $+\mathbf{K}$ at $-\kappa$. The Hamiltonian takes the form

$$H = -v_F(i\partial_x\sigma^x + i\partial_y\sigma^y) + \frac{\tilde{\lambda}_R}{2}(\sigma^x s^y - \sigma^y s^x) + \frac{\tilde{\lambda}_I}{2}s^z. \tag{4.23}$$

Note that we have added tildes to both the Ising and Rashba spin orbit parameters, as compared with previous sections. We do this to emphasize that $\tilde{\lambda}_I$ and $\tilde{\lambda}_R$ describe the *effective* SOI relevant to the moiré Dirac cones, and that they are not expected to be the same as the SOI induced by the TMD on monolayer graphene. We have again set m to zero.

The magnetic field may now be included in a straightforward manner by taking $-i\partial \rightarrow -i\partial + e\mathbf{A}$, where e is the electronic charge and $\mathbf{A}$ is the vector potential corresponding to a magnetic field of strength B (the Zeeman splitting is negligible at the energy scales considered). We work in the Landau gauge, setting $\mathbf{A} = B(-y, 0)$, and write the wavefunction as $\Phi(x, y) = e^{ikx}\phi(y)$, $\phi(y) = (\phi_{1\uparrow}(y), \phi_{2\downarrow}(y), \phi_{2\uparrow}(y), \phi_{2\downarrow}(y))^T$, where $1, 2$ denote the band indices (acted on by $\sigma^{x,y,z}$) and $\uparrow, \downarrow$ denote the spin (acted on by $s^{x,y,z}$). The eigenvalue equation may be

expressed as [149],

$$E\phi(y) = \begin{pmatrix} \tilde{\lambda}_I/2 & 0 & \omega_c A & 0 \\ 0 & -\tilde{\lambda}_I/2 & i\tilde{\lambda}_R & \omega_c A \\ \omega_c A^\dagger & -i\tilde{\lambda}_R & \tilde{\lambda}_I/2 & 0 \\ 0 & \omega_c A^\dagger & 0 & -\tilde{\lambda}_I/2 \end{pmatrix} \phi(y) \tag{4.24}$$

where E is the energy to be obtained, and $\omega_c = \sqrt{2}v_F/\ell_B$ is the cyclotron frequency, with $\ell_B = 1/\sqrt{eB}$ the magnetic length. The operator $A = -\ell_B\partial_y + \ell_B k - y/\ell_B$ is an annihilation operator, while $A^\dagger = \ell_B\partial_y + \ell_B k - y/\ell_B$ is a creation operator. They satisfy $[A, A^\dagger] = 1$. It follows that the functions $\phi_{i\alpha}(y)$ are superpositions of solutions to the $1d$ simple Harmonic oscillator. Further, each solution $\phi(y)$ with energy E corresponds to an extensively large set of degenerate states labelled by k. With this information, it is straightforward to show that the energies E must satisfy

$$0 = \left((n-1)\omega_c^2 - \left(\frac{\tilde{\lambda}_I}{2} - E\right)^2\right)\left(n\omega_c^2 - \left(\frac{\tilde{\lambda}_I}{2} + E\right)^2\right) + \tilde{\lambda}_R^2\left(\frac{\tilde{\lambda}_I}{2} - E\right)\left(\frac{\tilde{\lambda}_I}{2} + E\right) \tag{4.25}$$

for $n = 1, 2, 3, \ldots$. We denote these energies by $E_{n,\mu}$, $\mu = 1 - 4$. It is then straightforward to show that the Landau level spectrum corresponding to a Dirac cone of the opposite chirality may be obtained directly by taking the *negative* of the solutions to Eq. (4.25). Equivalently, the energies from the $-\mathbf{K}$ valley must satisfy

$$0 = \left((n-1)\omega_c^2 - \left(\frac{\tilde{\lambda}_I}{2} + E\right)^2\right)\left(n\omega_c^2 - \left(\frac{\tilde{\lambda}_I}{2} - E\right)^2\right) + \tilde{\lambda}_R^2\left(\frac{\tilde{\lambda}_I}{2} + E\right)\left(\frac{\tilde{\lambda}_I}{2} - E\right). \tag{4.26}$$

We present in Fig. 4.14b solutions to Eqs. (4.25) and (4.26) for $n \leq 30$. Since the density of a Dirac cone is proportional to the energy squared, we plot the magnetic field against the energy *squared*. The parameters chosen are $(\tilde{\lambda}_I, \tilde{\lambda}_R) = (3, 4)$ meV with $v_F \approx 8.8 \times 10^4$ m/s, as appropriate for $\theta = 0.87°$.

In the physical sample, the Landau levels are not actually expected to be infinitely degenerate, but rather possess some finite width. We model this effect through a phenomenological broadening of the density of states $D(E, B)$:

$$D(E, B) = 2 \cdot \frac{eB}{2\pi} \sum_{n=1}^{\infty} \sum_{\mu=1}^{4} \sum_{\eta=\pm} \frac{1}{\sqrt{2\pi}\Gamma} \exp\left[-\frac{(\eta E_{n,\mu} - E)^2}{2\Gamma^2}\right]. \tag{4.27}$$

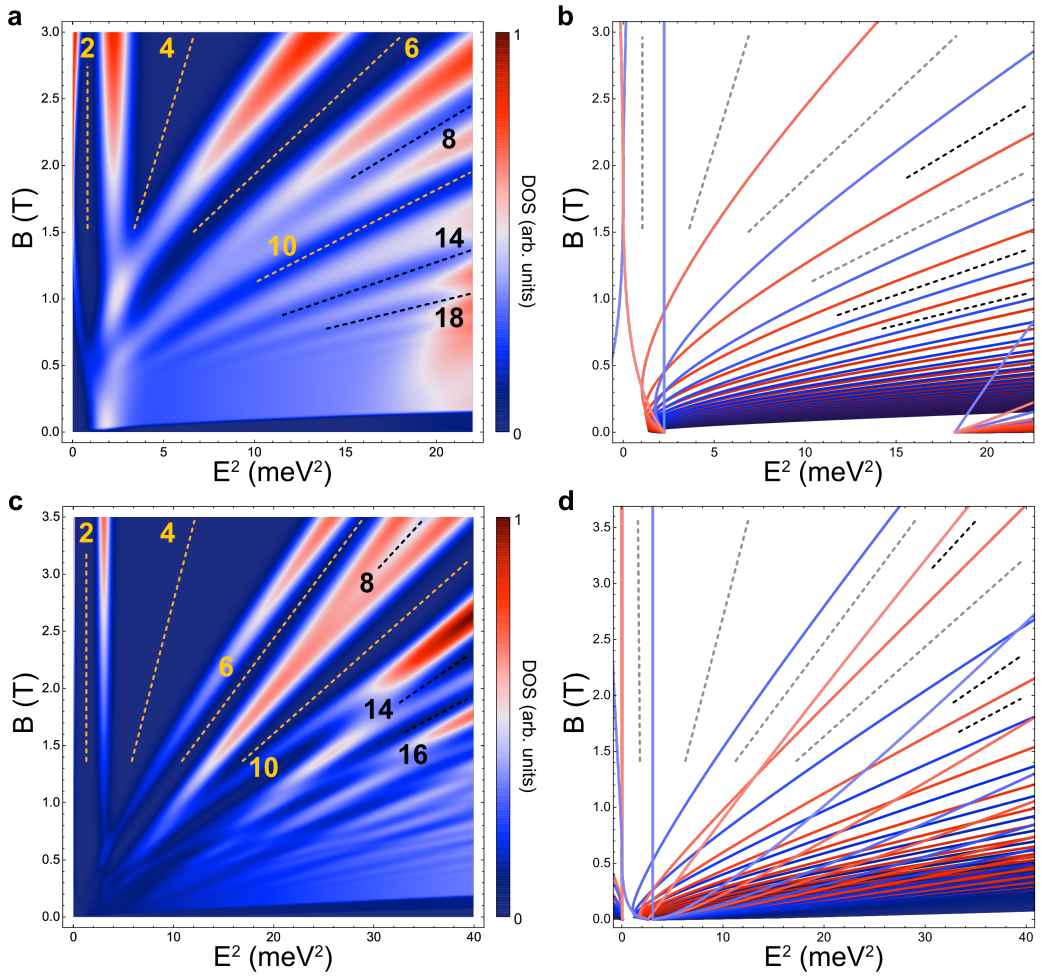

Figure 4.14: **Theoretical Landau-level spectrum** (**a**, **c**) Color plot of the phenomenologically broadened density of states (Eq. 4.27) as a function of energy squared in $(\text{meV})^2$ (roughly equivalent to the electron density that is gate-tuned in the experiment) and the magnetic field in Tesla. (**b**, **d**) The spectrum without taking broadening effects into account. Blue and red lines correspond to levels originating proximate to the $+\mathbf{K}$ and $-\mathbf{K}$ valleys respectively. The parameters considered are $(\tilde{\lambda}_I, \tilde{\lambda}_R, \tilde{\lambda}_{\text{KM}}) = (3, 4, 0)\,\text{meV}$ with a broadening $\Gamma = 0.22\,\text{meV}$ and (**a**, **b**) and $(\tilde{\lambda}_I, \tilde{\lambda}_R, \tilde{\lambda}_{\text{KM}}) = (1.5, 2.5, 2)\,\text{meV}$ with a broadening $\Gamma = 0.15\,\text{meV}$ (**c**, **d**). The velocity in both is $v_F \approx 10^5\,\text{m/s}$, as appropriate for $\theta \approx 0.8^\circ - 0.9^\circ$. We note that the Landau level sequence and energy levels on the hole-doped side are identical to those shown here for **a** and **b**. When both $\tilde{\lambda}_I$ and $\tilde{\lambda}_{\text{KM}}$ are nonzero, as in **c** and **d**, a slightly different Landau-level sequence is generically obtained at negative energies relative to the CNP.

the coefficient out front, $2 \cdot eB/(2\pi)$, gives the degeneracy of each Landau level, $eB/(2\pi)$ times the number of Dirac cones within each of the **K** valleys. The sum over $\eta = \pm$ then accounts for the two valley flavours $\pm\mathbf{K}$. We present a color density plot of this function in Fig. 4.14a as a function of the magnetic field and E^2 using the same SOI parameters as above with a broadening $\Gamma = 0.22\,\text{meV}$. The sum over n is evaluated up to $n = 30$. Notably, this simple model is able to reproduce several key features of the Landau level sequence shown in Fig. 4.3. For instance, at the higher fields shown, a sequence 2,4,6,8,10,... is observed. By contrast, at lower fields, we instead find 4,6,10,14,....

4.6 Search for magnetism

As we discussed towards the end of Chapter 2, TBG, when aligned with one of the encapsulating h-BN layers, can become a Quantized Anomalous Hall (QAH) insulator, where the bulk is insulating but the edges host a chiral conducting mode. The devices reported in literature [13, 39] (two, as of the writing of this thesis) that show this effect do not show any signatures of superconductivity. The breaking of C_2 symmetry achieved by aligning h-BN with graphene appears to be essential for ferromagnetism [150], but does the superconducting state need it to be preserved? It is not clear if these two states can co-exist within the same device or not because of the low statistics on ferromagnetic TBG devices.

To understand this relationship better, we tried to use the fact that our devices show a superior yield of superconductivity to fabricate a TBG/WSe_2 device where the TBG edge was optically aligned with the h-BN edge on purpose. This optical alignment however, does not offer any guarantees that the graphene edges will remain aligned with the h-BN edge at the end of the fabrication process. And if it does remain aligned by the end, there is a 50% chance that it will be the correct edge since graphene and h-BN have two types of edges (armchair and zig-zag). Fig. 4.15 shows the optical images of device D5 at different stages.

On cooling this device, the first hint that this could be magnetic was provided by the insulating behavior at the Charge Neutrality Point (CNP). We could fit the temperature dependence of the CNP resistance to a Arrhenius-like gap with a value of 5.55 meV or 64K, as shown in Fig. 4.16 which is consistent with a gap opening induced by h-BN alignment [39]. The angle for the TBG sheets measured on this device is about 1.15°. Unfortunately, only 4 electrodes were working on this device, two in the middle which denote the angle in (Fig. 4.15 b), and two current sourcing

electrodes, which meant that we could not get a reliable R_{xy} measurement. The device showed well-developed full filling insulating states as well as features at partial filling factors.

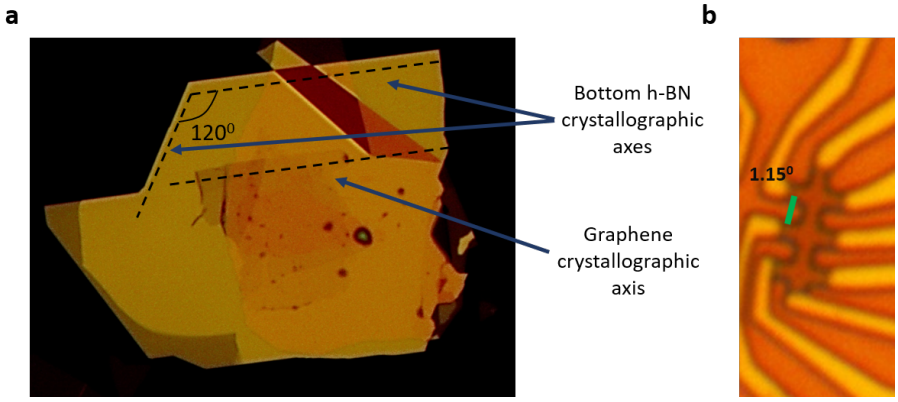

Figure 4.15: **a)** Optical image of assembled heterostructure on PC (polymer) for device D5. To observe magnetism, it is extremely important to align the crystallographic axes of h-BN and TBG in addition to maintaining a twist angle of $\approx 1.^{\circ}$ in the TBG. **b)** Finished device depicting the electrodes of interest.

Fig. 4.17 shows the dependence of the longitudinal resistance R_{xx} on the sweep direction of the magnetic field taken at the +3 filling factor (where one would expect to see ferromagnetism). The data clearly shows a hysteretic behavior with large jumps (few kΩs) in line with a magnetic behavior. This hysteretic feature disappears along with increasing temperature and is totally suppressed around 3K. Superconductivity is notably absent from this device. While the R_{xy} measurement is absent due to bad contacts, the R_{xx} measurement strongly suggests a magnetic feature in this device. It therefore appears that WSe_2 does help with maintaining the intended twist angle. Utilizing this fact, the next step would be to investigate a more uniform TBG device that shows magnetism in several contacts to fully understand the interplay between magnetism and superconductivity in TBG.

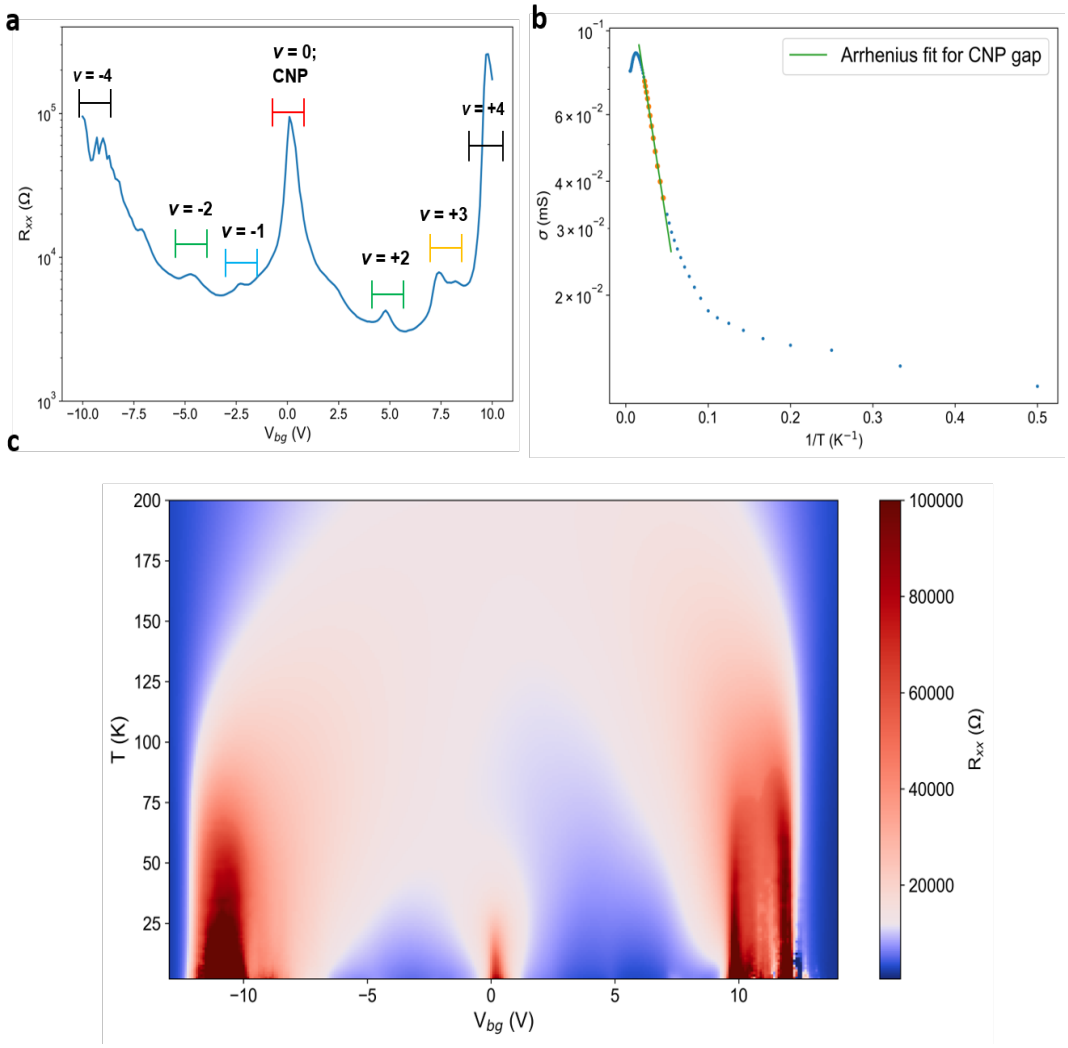

Figure 4.16: **a)** Resistance as a function of backgate voltage (or carrier density) taken at 2K. Color bars denote the location of the various filling factors. **b)** Temperature dependence of the resistance value at the Charge Neutrality Point (CNP). A thermally activated gap value of 64K can be extracted from an Arrhenius fit. **c)** Full temperature dependence of resistance as a function of backgate voltage showing the evolution of insulating states at different filling factors.

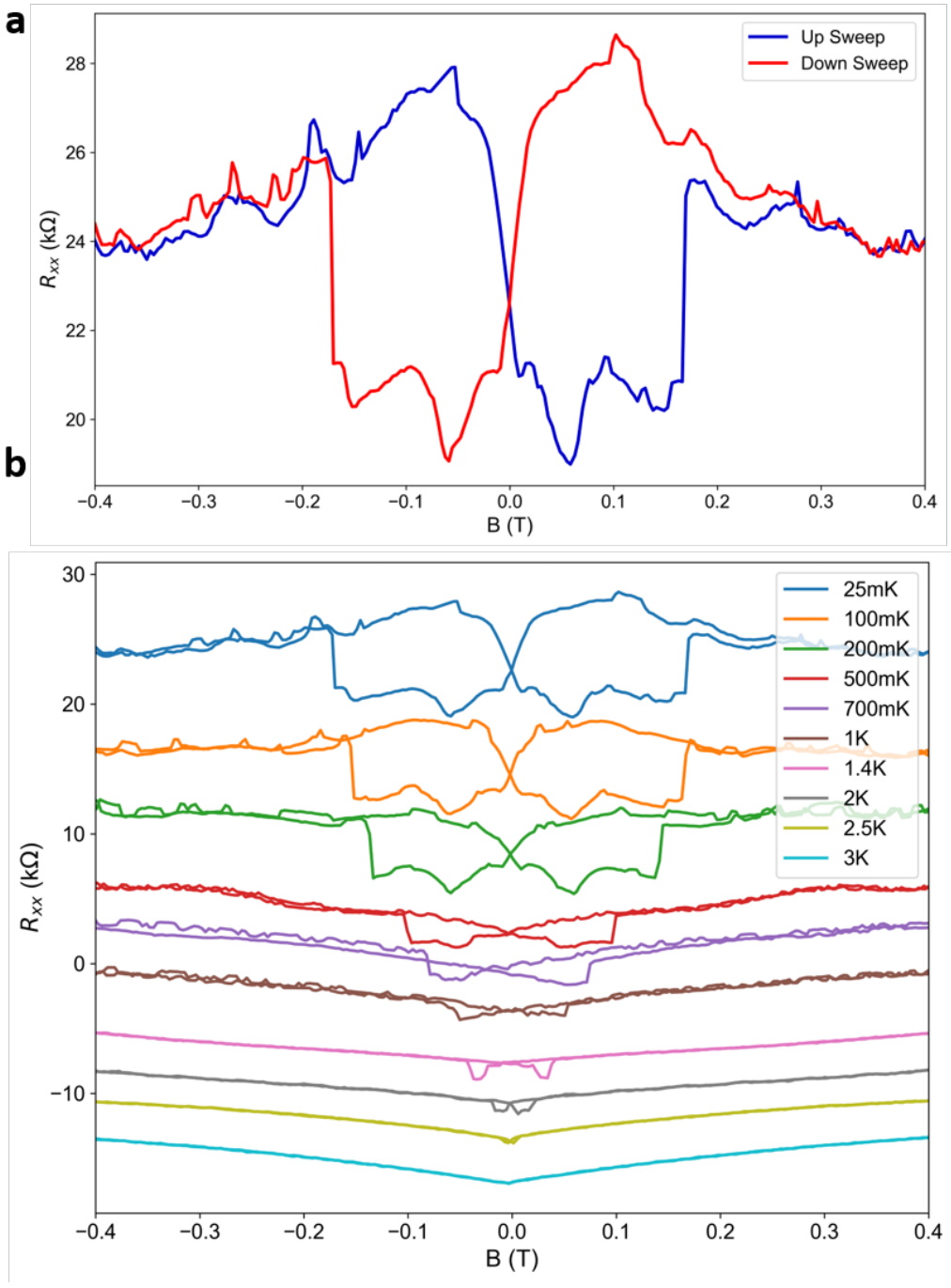

Figure 4.17: **a)** Hysteretic behavior around +3/4 filling factor in device D5 (1.15°) showing jumps in resistance of the order of few kΩs suggestive of magnetism in this device. **b)** Temperature dependence of this hysteretic behavior which disappears around 2.5K. Curves are offset from each other by 1-5kΩs for clarity.

Chapter 5

CONTINUOUS THERMOMETRY IN GRAPHENE

5.1 Introduction

In the previous chapters, we investigated TBG using electronic transport measurements at low temperatures and high magnetic fields. Apart from features that can be studied by these measurements, exotic electronic phases can also have interesting thermal signatures, as demonstrated by Banerjee *et al.* for the case of the 5/2 fractional quantum hall state in GaAs–AlGaAs heterostructures [151, 152]. In these experiments, the authors showed that the magnitude of the thermal Hall conductance for the 5/2 state was $2.5k_0$ (where k_0 is the universal quantum of thermal conductance [153]), and their observation confirmed the topological nature of this state.

In the context of TBG, its thermal properties and in particular, the strength of its electron-phonon coupling remain a complete mystery. Thermal measurements can also be valuable when electronic measurements have difficulty in probing the physics of certain phases, such as the correlated insulating phase in TBG. So, it would be of great interest to explore TBG thermally, however these measurements can be very challenging as shown by Banerjee *et al.* and need a complex setup. With this in mind, it made sense to us to first thermally investigate a system that we understand really well, to dot all the i's and cross all the t's with respect to the measurement setup. Single layer graphene provides an ideal test bed for these measurements, which is what we decided to pursue.

Josephson effect in graphene

While monolayer graphene has not yet shown intrinsic superconductivity, it can be easily coupled to a conventional superconductor, which induces superconductivity into the graphene sheet via the Josephson effect. For the case of graphene encapsulated in h-BN, the Josephson effect has been seen for micron scale junction lengths due to the ballistic nature of graphene [154, 155]. The supercurrent in this proximitized layer can be manipulated by a gate electrode. Importantly, the supercurrent induced in the graphene sheet is strongly dependent on temperature. As we will see, this provides an inductive element that can be tuned in situ, which can be very useful in establishing coherent control of microwave circuits [156]. In this chapter,

we use an inductive resonator based readout technique that integrates graphene into a superconducting microwave circuit and try to fill the gaps in knowledge about graphene's thermal behavior at milliKelvin temperatures. We measure, for the first time, thermal conductivity in graphene for both electron and hole doping, which seem to thermalize differently.

Graphene at high frequencies

van der Waals (vdW) materials and superconducting circuits have evolved over the last decade into mature fields without any significant overlap. Their intersection is very promising in the context of quantum computing due to the extreme tunability of vdW materials. Also, while graphene has been studied extensively using DC transport measurements, very few studies exist (comparatively speaking) studying its behavior at higher frequencies, which is a necessary prerequisite for applications in quantum information science. Therefore, even though in this chapter we don't necessarily focus on qubits based on graphene and other 2-D materials, it is important to emphasize that the knowledge developed in performing these measurements will be useful and crucial for the development of any infrastructure that relies on graphene based qubits.

Graphene as a heat element

From an applications standpoint, graphene is also very interesting for applications like calorimeters and bolometers relying on thermal effects as shown in Fig. 5.1. For a calorimeter, the highest sensitivity is achieved by minimizing the energy resolution, which is given by:

$$\Delta E_{rms} \geq \alpha\sqrt{k_B T^2 C} \tag{5.1}$$

In the case of a bolometer, the highest sensitivity is achieved by minimizing the Noise Equivalent Power (NEP). The minimum threshold for the NEP is given by:

$$NEP \geq \sqrt{4k_B T^2 G} \tag{5.2}$$

where G and C are the thermal conductance to the heat sink and the heat capacity respectively. Here, one can define a thermal time constant (τ) as $\tau = C/G$. Due to the 2-D nature of graphene and its low carrier density (around 10^{11} carriers/cm^2), graphene has an extremely small heat capacity (of the order of 10^{-21}J/(Kμm^2)). The heat conductance of the electron gas in graphene can also be minimized by optimizing for area, contacts, and substrate. Because of the extreme tunability of its

thermal time constant (from μs [157] to picoseconds [158]), graphene is a promising material for engineering bolometric and calorimetric devices.

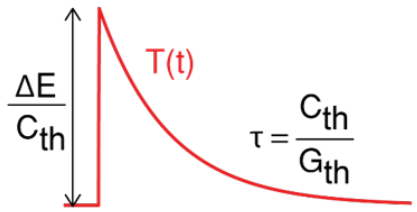

Figure 5.1: Increase in temperature caused by a heat pulse and subsequent relaxation.

5.2 Real time thermometry with superconducting circuits

An avenue that we ended up pursuing (at least for now that is) used superconducting resonators for doing ultra-fast temperature readout, making thermal measurements much easier. In graphene-based systems, the electron temperature readout has relied either on (i) resistance based thermometry, (ii) Johnson noise thermometry, or (iii) temperature dependence of critical current of proximitized graphene Josephson junctions. We will take a quick look at these methods and how they have been employed so far.

Resistance-based thermometry

An easy quantity that can be used to understand graphene's thermal conductance is the change in resistance as a function of temperature. While this can provide important insights into its superior thermal properties at room temperature, for high quality graphene at low temperatures (<30K), there is hardly any change in resistance with temperature. Another method that was used widely in the early days of graphene relied on the change in its Raman spectrum with temperature [6, 159], but it faced the same issues at low temperatures. So, there was a need for other schemes of measuring its thermal response at low temperatures.

Johnson noise thermometry

Fong *et al.* [160] performed the first measurements of heat capacity and thermal conductance on graphene using Johnson noise thermometry at microwave frequencies and cryogenic temperatures. The graphene they measured was resting on a SiO_2 substrate and was in the diffusive regime. By making the device length longer than

the electron scattering, they were able to rule out issues caused by electronic shot noise. Setting up Johnson noise thermometry at milliKelvin temperatures can be very challenging though. Also, for ballistic graphene, the mean free path of charge carriers can be several micrometers (as big as the graphene flake essentially). This is where supercurrent-based thermometry comes into the picture.

Supercurrent-based thermometry

The maximum amount of supercurrent that can be supported by a Josephson junction (its critical current) depends strongly on the temperature: lowering the temperature increases the critical current value. This fact can be used to extract the thermal conductance by first extracting the dependence of the critical current on the stage temperature of the cryostat. Then by applying Joule heating, one can determine the temperature rise in the electron gas by looking at the value of the critical current. For a two-dimensional electron gas, there are three modes of coupling to the environment thermally:

1. G_{WF} - coupling to the electrical leads through electron diffusion,
2. G_{ep} - coupling to the lattice phonons,
3. G_{rad} - coupling to the electromagnetic environment.

The total thermal conductance G_{tot} is the sum of all the three mechanisms. For graphene, the blackbody radiation loss is of the order of 10^{-15} pW/K and is usually neglected in comparison to G_{WF} and G_{ep}. An advantage of using this method is that by using superconducting electrodes, diffusion into the electrodes can ideally be suppressed because of the existence of the superconducting gap. This can allow us the isolate the thermal conductance due to electron-phonon coupling (G_{ep}), which is of particular interest in exotic material systems like TBG. One can go a step beyond the simple method of measuring the critical current. By incorporating the system of interest into a superconducting resonator circuit, we can measure the "true value" of the supercurrent without having to switch out of the superconducting state. This method is the one we chose to follow for our measurements.

5.3 Characterization of graphene - aluminum Josephson junctions

As a first step towards integrating graphene into superconducting circuits, it was important to establish the quality of the superconducting contacts that we can make to graphene. Fig. 5.2 shows the data from a graphene-aluminum Josephson junction

we fabricated. A good indicator of contact transparency is the multiple Andreev reflection (MAR) [53, 161], where an electron (hole) that has energy less than what is required to overcome the superconducting barrier gets reflected successively before diffusing into the contact. In our junctions, we can observe at least up to 4th order MAR steps suggestive of very high transparency between graphene and aluminum.

We also obtain high I_cR_n products of the order of 0.5Δ (Δ is the superconducting gap of aluminum), comparable to the best reported devices in literature. Consistent with observations from other groups, we observe that the charge neutrality point (CNP) is shifted to negative gate voltages indicating n-type doping due to the aluminum contacts. As a result, when the graphene is p-doped (holes as the majority carrier), a p-n junction is formed, which causes the induced superconductivity to be weaker on the hole side.

5.4 Device design and measurement setup

The ideal graphene-based bolometer would have a temperature dependent supercurrent with inductive readout and an isolated heater electrode to avoid disturbing the resonant area with a DC current. The resonator area would be used for temperature readout, the heater port would heat up the graphene flake, and the only way these two regions would "talk" with each other would be through hot electrons near the heater equilibrating the entire graphene flake to a certain temperature. See Fig. 5.3 for a schematic depicting this, along with a zoomed in optical image of an actual device. To come up with a design, we wanted to create a circuit with the highest resonant frequency detectable in our setup, because that would give us the fastest readout. The biggest restriction was the cutoff frequency of the cryoamplifier, which was around 2.2 Ghz. So, we had to reverse engineer the superconducting resonator with that restriction.

According to the Resistively and Capacitively Shunted Josephson junction (RCSJ) model, any Josephson junction can be represented as an electrical circuit via a combination of resistors, capacitors, and inductors (strongly dependent on the critical current). A $\lambda/4$ transmission line (co-planar waveguide) resonator circuit was the simplest one to work with. If we just think of a transmission line resonator of length "l" and forget about the graphene, a resonance condition occurs when the wavelength λ of the voltage across the transmission line is equal to 4xl. Adding a graphene element just adds to the length "l" of the transmission line (which decreases the resonant frequency). The higher the critical current, the lesser the effect of the

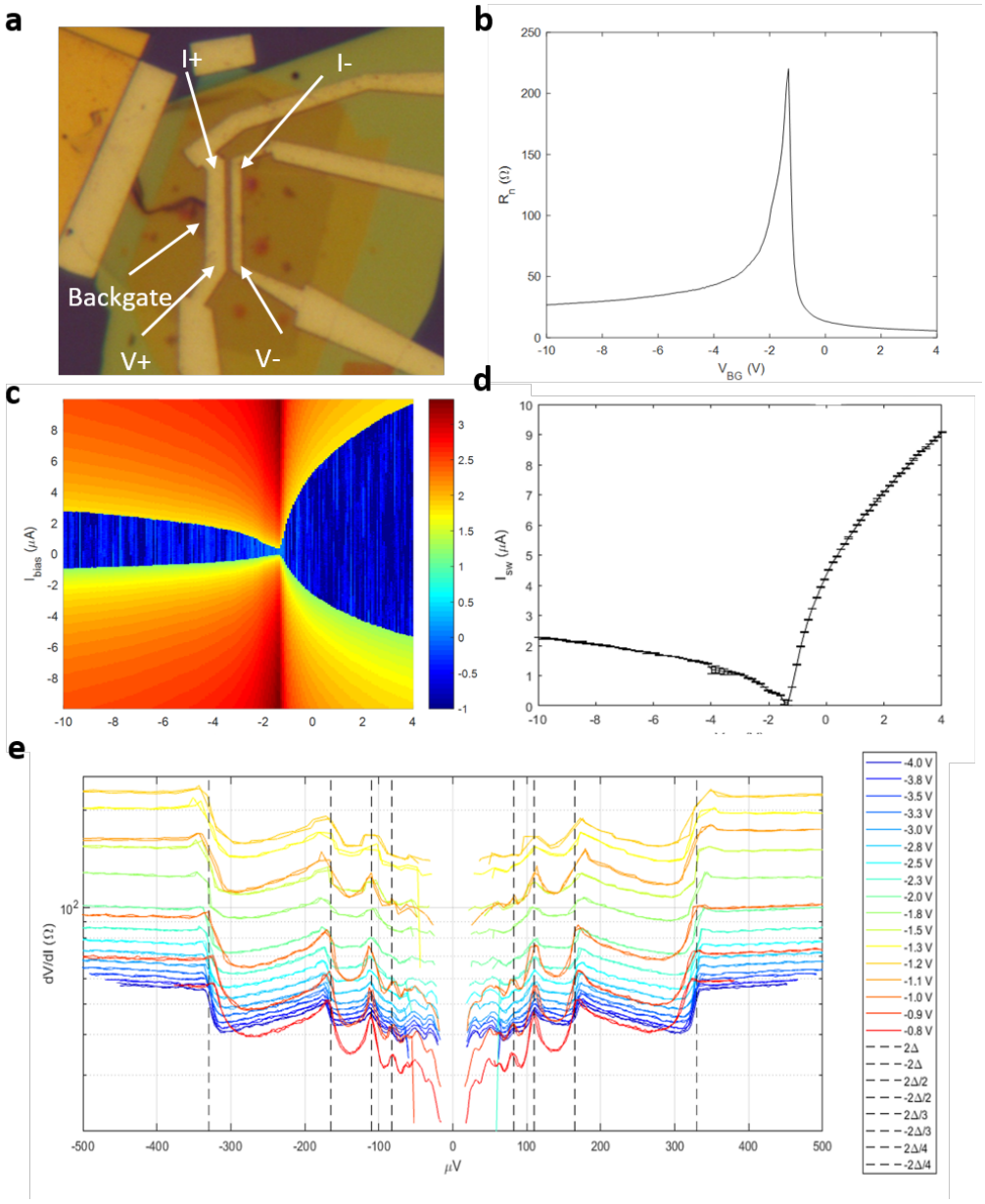

Figure 5.2: **a)** Optical image of a graphene Josephson junction with aluminum superconducting electrodes. **b)** Resistance as a function of backgate voltage at 4K (above the superconducting transition temperature of aluminum. **c)** 2-D plot of resistance as a function of applied current and backgate voltage, the blue area represents the superconducting region. **d)** Line cut depicting the temperature dependence of the supercurrent vs the backgate voltage. **e)** Evidence of fourth order Multiple Andreev Reflection (MAR) in the graphene junction demonstrating the high quality of contacts.

graphene on the length of the transmission line. Therefore, as the critical current decreases, the resonant frequency should shift downward. We aimed to have the resonance occur slightly below 1Ghz, in case we wanted to access higher harmonics. Values for the CPW design were chosen after electromagnetic simulations in the commercially available software Sonnet. We model the combination of a CPW, a coupling capacitor, and a Josephson junction to arrive at the the dependence of a resonant feature as a function of critical current. The simulation is done in a software known as "Microwave Office" provided by National Instruments. An example of the calculation performed is shown in part a of Fig. 5.6

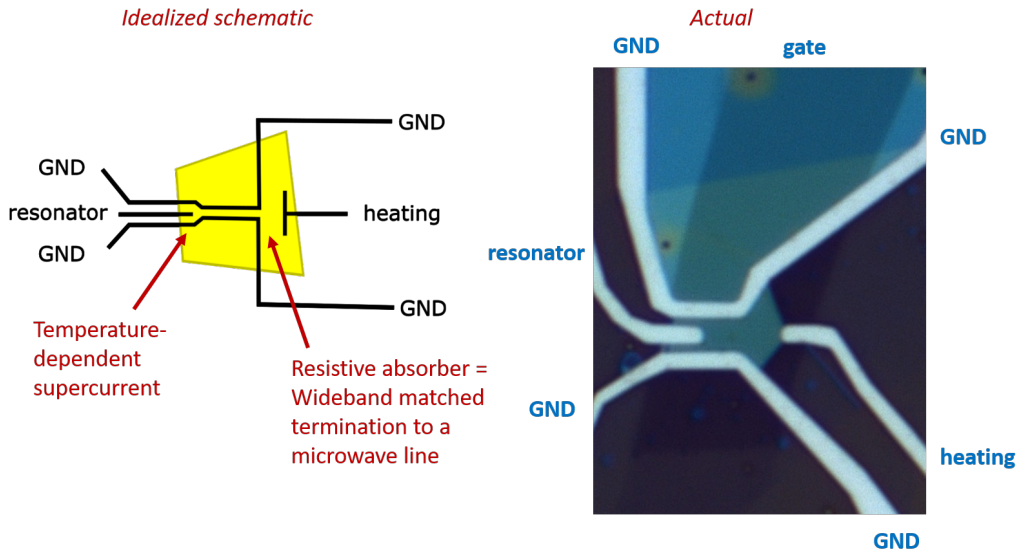

Figure 5.3: Graphene-based bolometer idealized schematic vs actual device active area.

5.5 Backgate modulation of resonance

As a sanity check, we also simulated the modulation of the resonant frequency based on expected critical currents in graphene (we estimated a peak critical current density of 1μA per μm of junction length for 500 nm separation, in accordance with the DC Josephson junction shown in Fig. 5.2). Assuming small excitations, the current-phase relationship in the Josephson junction should be sinusoidal. The Josephson inductance (L_j) depends on the critical current as:

$$L_j = \frac{\phi_0}{2\pi I_c.} \tag{5.3}$$

As can be seen from Fig. 5.6, the simulation matches really well with the experimental observed resonance behavior, solidifying our belief in the impedance

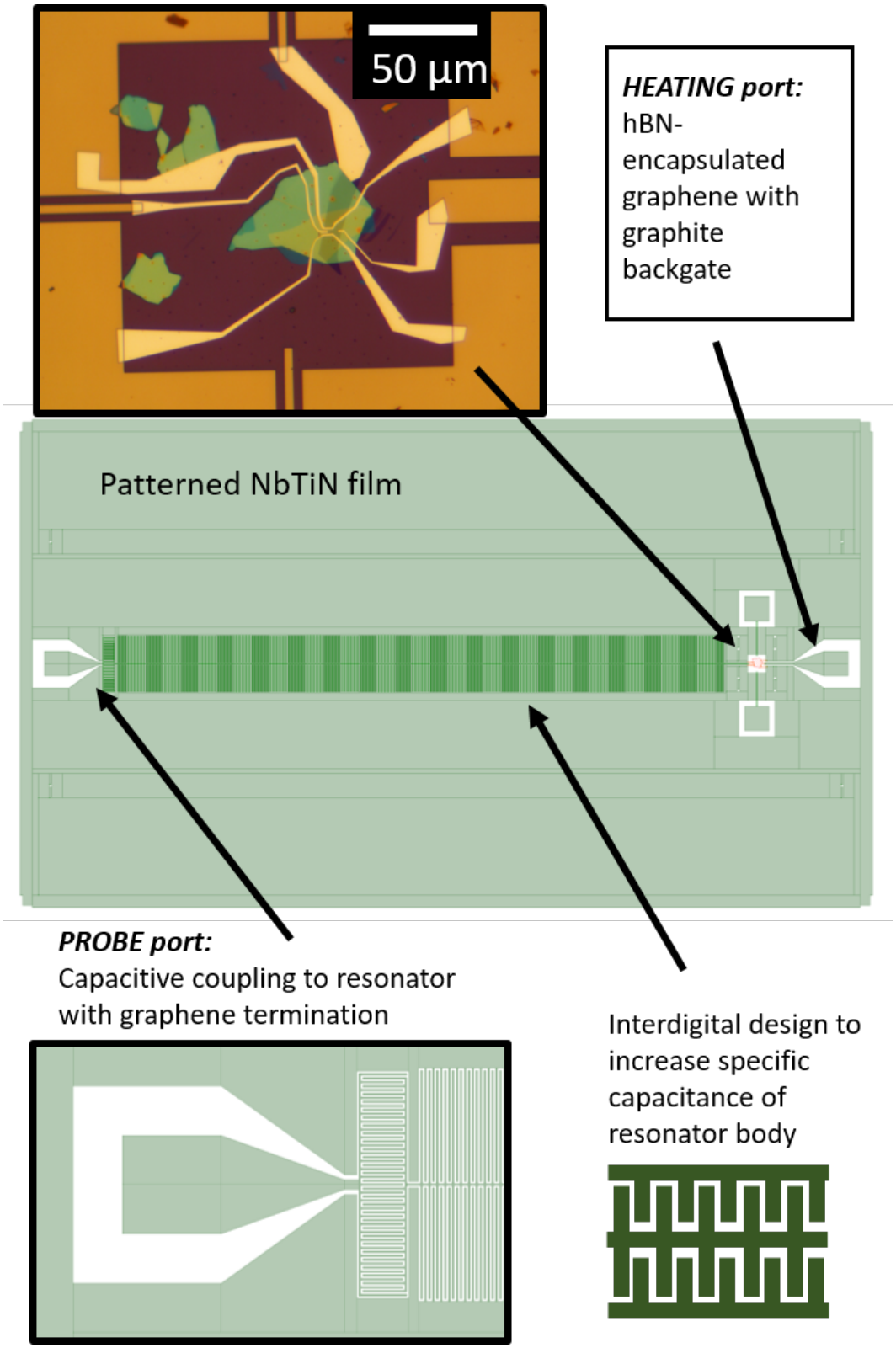

Figure 5.4: Full device design indicating the important aspects considered.

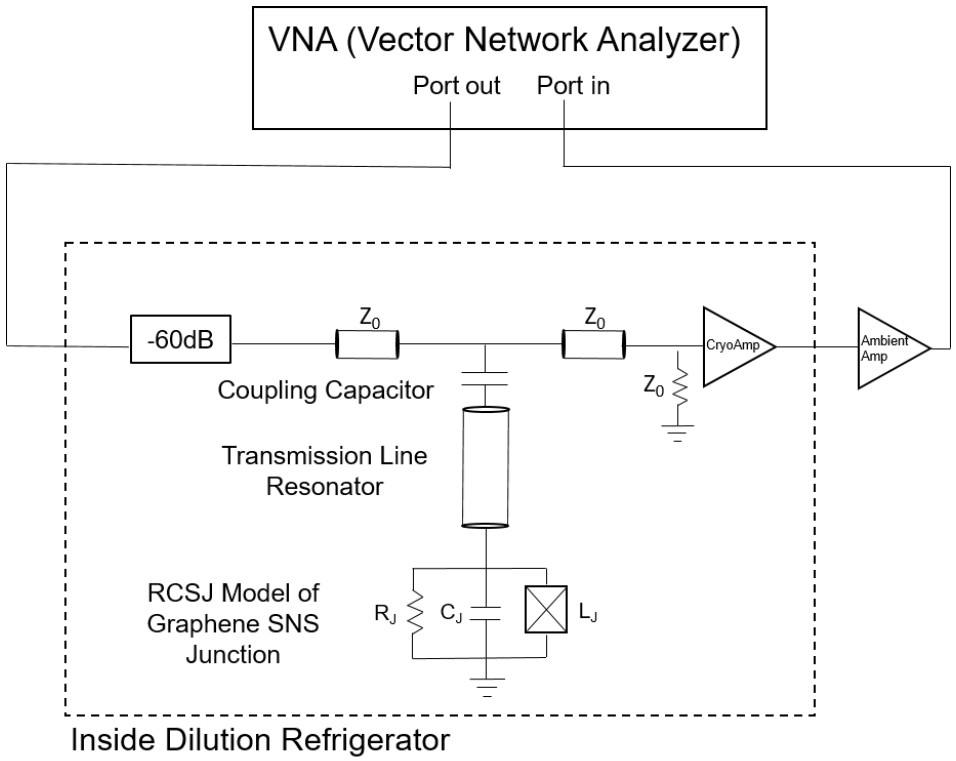

Figure 5.5: Measurement setup Graphene Josephson junction.

model we have created for the graphene junction. The first demonstration of this in situ modulation was done by Schmidt *et al.* [162] with a similar circuit with the exception of the heater electrode.

What do we expect to happen to the resonance as the backgate voltage changes? By changing the backgate voltage, we are effectively changing the carrier density in the graphene sheet. As we move further away from the Dirac point or the Charge Neutrality Point (CNP) in either direction, we are providing more charge carriers to the superconducting phase. Therefore, the critical current increases as we move away from the CNP. This means that the resonant frequency also increases on doping the graphene, the CNP is where the minimum of the resonant frequency occurs. Additionally, when the graphene is p-doped (holes), Fabry-Perot like oscillations can be seen in the gate sweep. These oscillations arise due the p-n junctions formed near the contacts and serve as a signature of ballistic transport in graphene [162].

5.6 Heater response

The heating contact shown in Fig. 5.3 is basically a superconducting contact that's far enough away from the other superconducting electrodes so that there is no

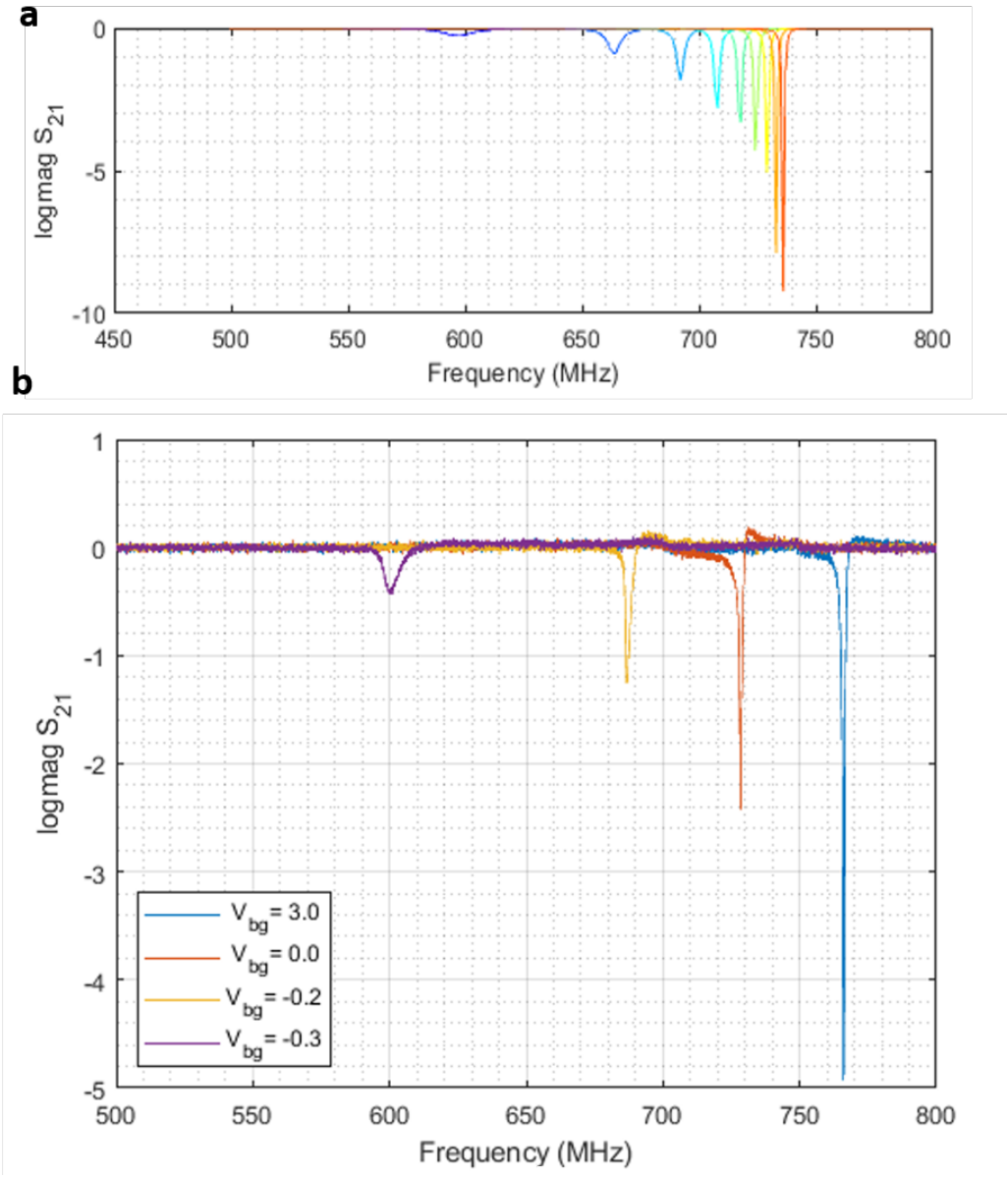

Figure 5.6: **a)** Simulation of the change in resonant frequency vs changing critical current. **b)** Experimentally obtained change in resonant frequency as a result of changing critical current controlled by tuning the carrier density. With decreasing critical current, the resonance shifts downward in frequency.

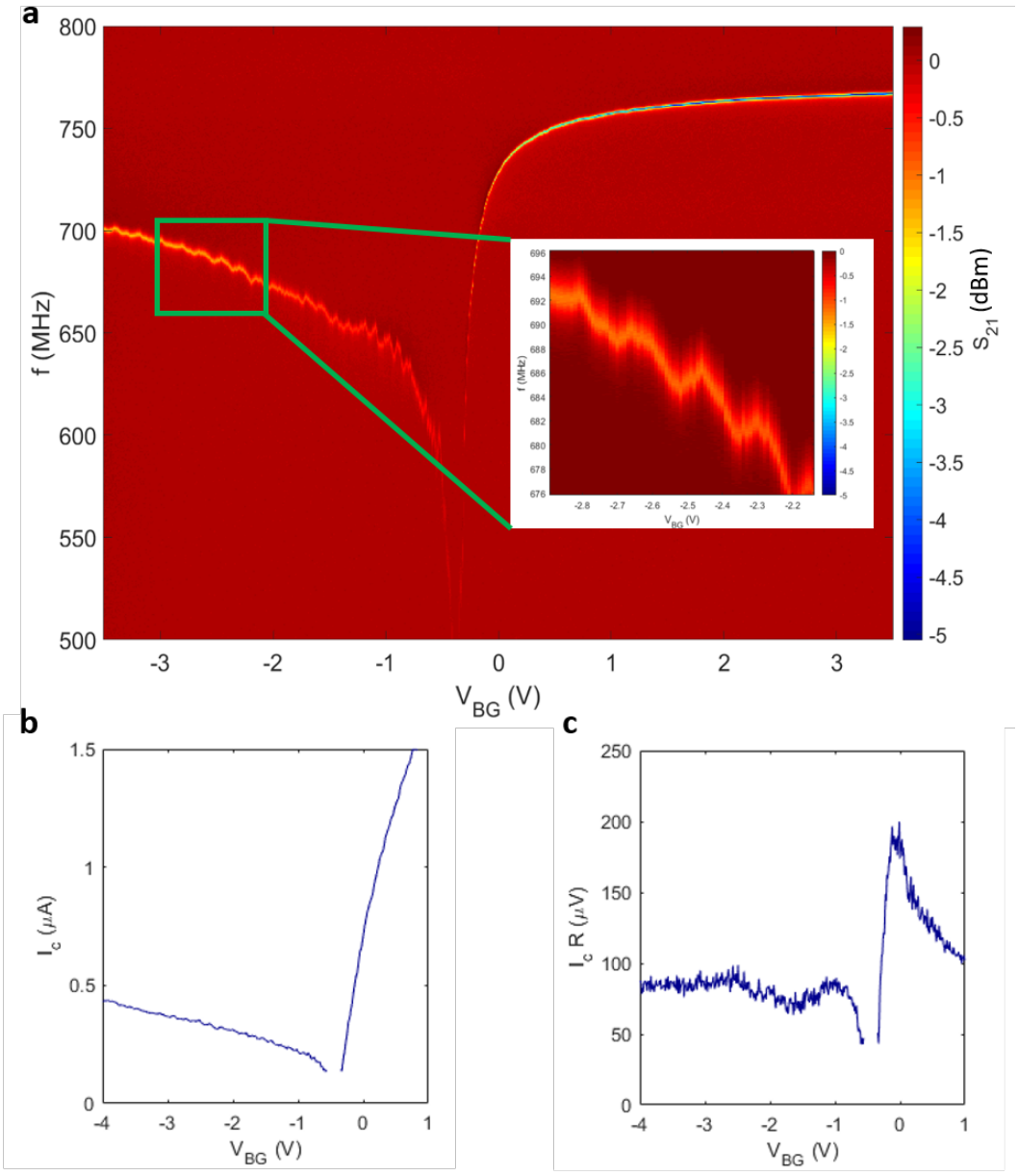

Figure 5.7: **a)** Modulation of resonant frequency as a function of backgate voltage (background subtracted). By changing the carrier density through the backgate voltage, the supercurrent in graphene is modulated, which affects the resonant frequency. The resonance can be tuned about 250 MHz in situ by this mechanism. Inset shows Fabry-Perot like oscillations when the graphene is p-doped (holes). These oscillations arise due the p-n junctions formed near the contacts and serve as a signature of ballistic transport in graphene. **b)** and **c)** Extracted values for critical current (I_c) and I_cR_n product based on the RCSJ model parameters shown in Fig. F.1 of the Appendix. The I_cR_n product shows qualitatively very similar behavior to the DC Josephson junction.

supercurrent between the heating contact and other electrodes. This enables us to heat the graphene sheet via Joule heating (I^2R) upon passing a current through the flake. The ideal contact for this heating element is a purely ohmic contact because it is easy to extract the power sent through to the flake for an ohmic contact. If the heating is applied through a pulse then after an initial rise, the temperature decays according to the thermal time constant as shown in Fig. 5.1. However, for continuously applied DC heating, the temperature of the electron gas equilibrates to a certain temperature where incoming power equals the heat loss to the environment.

$$C\frac{dT}{dt} = P_{in} - G(T - T_0) \tag{5.4}$$

Fig. 5.8 shows examples of what happens to the resonance feature when a DC heating current is applied. For higher DC current, the temperature of the graphene increases, causing the critical current in the junction to decrease. This makes the resonance move downward in frequency. We utilize this movement of the resonance in response to applied DC heating power to extract useful thermal parameters for our graphene flake.

5.7 Inductive readout of temperature

Perhaps the most critical step in the process of doing thermal measurements on graphene is the ability to relate the electron temperature to a quickly measurable quantity, which, in this case, is the position of the resonance in the frequency space. To establish a calibration of the resonance with temperature, we set the mixing chamber to the lowest temperature. Then, we can do one of two things, (i) do a backgate vs resonant frequency at several temperatures and then apply heater pulses at base temperature, or (ii) fix the gate voltage and sweep the mixing chamber temperature while applying Joule heating. We chose to use the second method for our measurements as it reduces the effect of charge noise caused by residual charges in the backgate dielectric.

Instead of switching the system out of the superconducting state to measure the critical current and hence the temperature, in the inductive readout method, the temperature can simply be extracted by tracing the movement of the resonant feature. The beauty of this method is that the resonance feature (and therefore the electron temperature) can be continuously monitored with minimal disturbance to the graphene flake. If we try to conduct this experiment on materials with fragile electronic states, this method of detection can be extremely helpful.

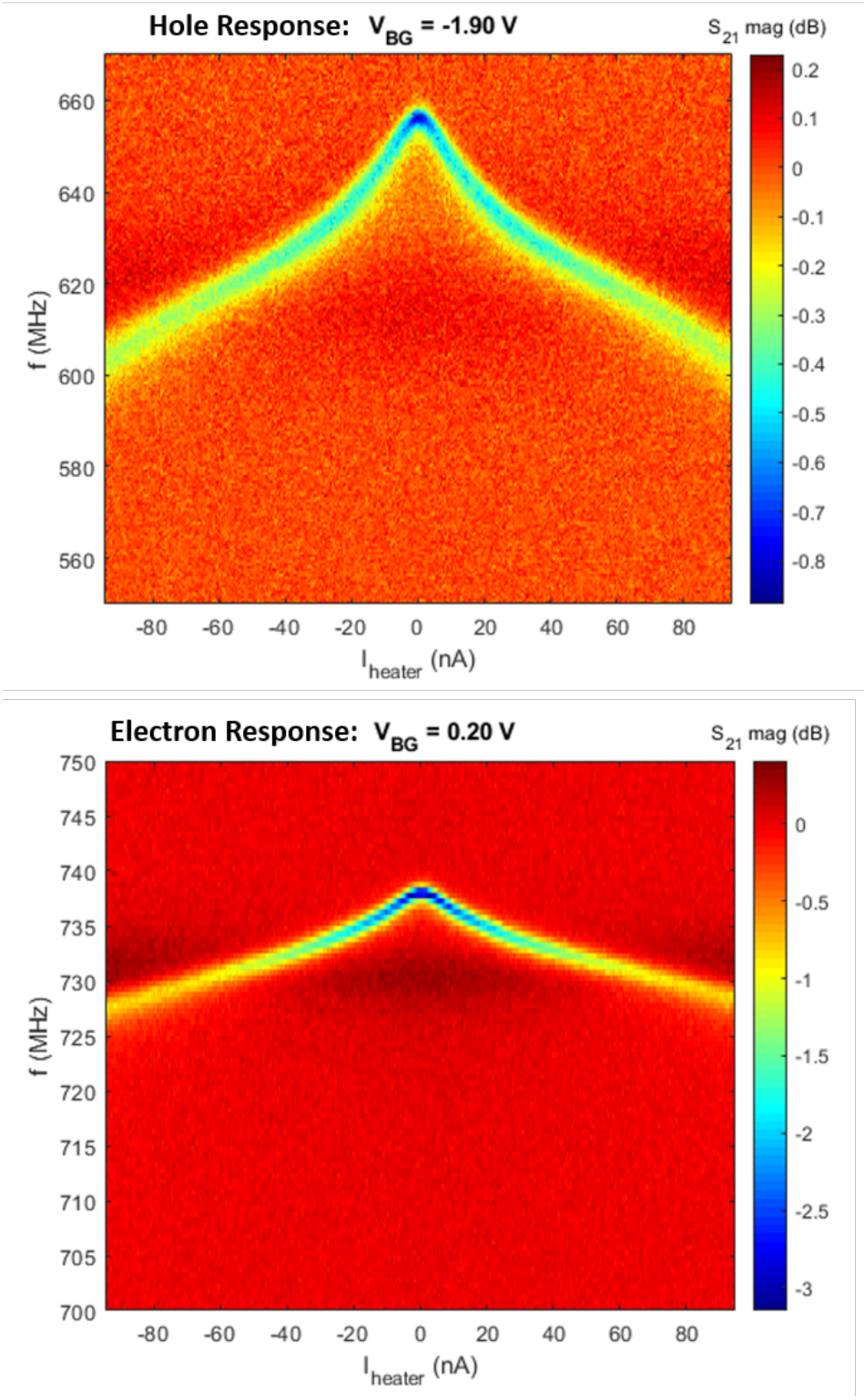

Figure 5.8: Modulation of resonant frequency as a function of heater current. The electron and hole response look very different qualitatively. The electron doped graphene appears to need higher powers for a small rise in temperature, indicating that the cooling of electrons is much more efficient than the holes.

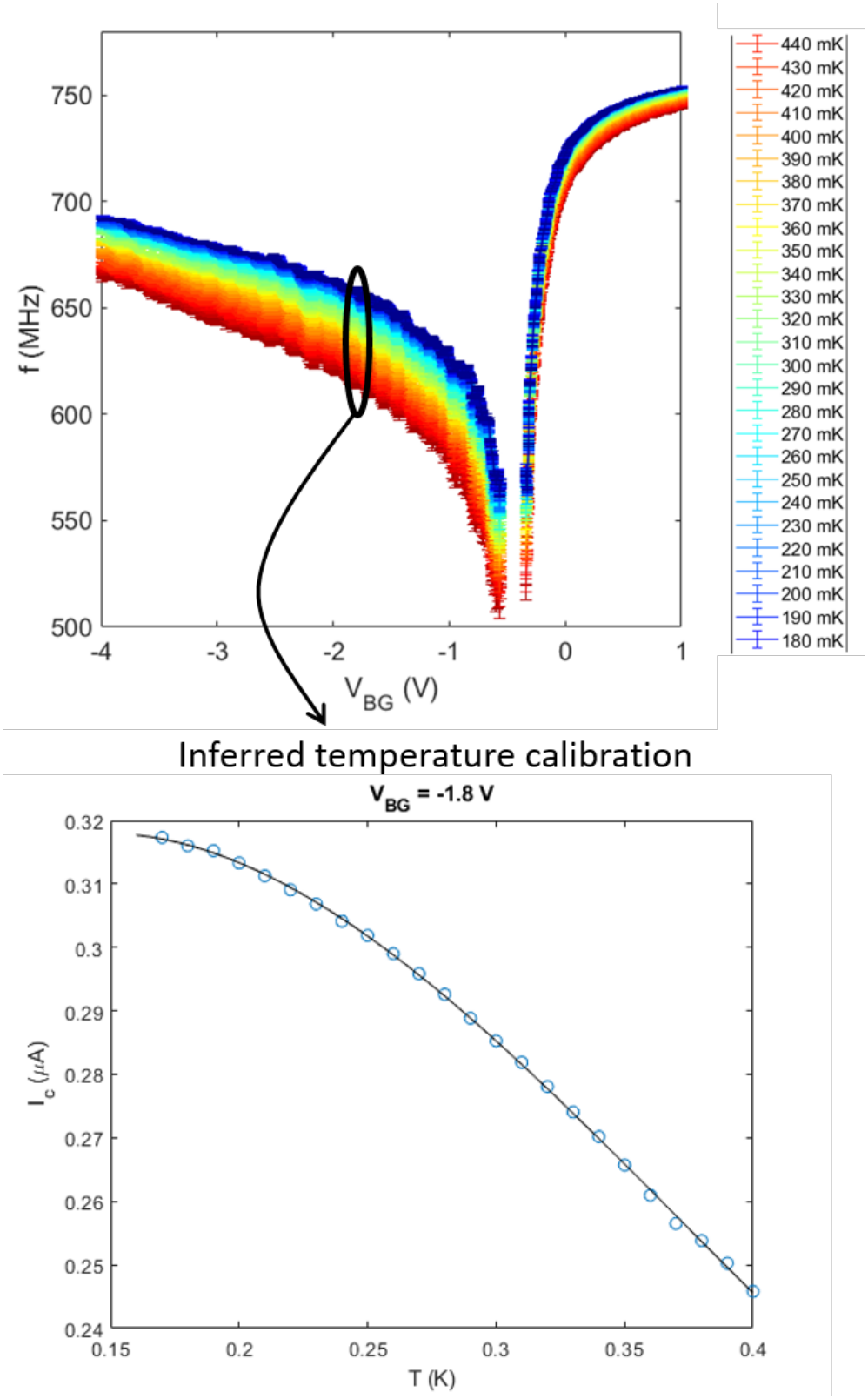

Figure 5.9: Modulation of resonant frequency as a function of temperature. For every backgate voltage, the dependence of the critical current on temperature can be extracted from the movement of the resonant frequency based on the RCSJ model.

5.8 Power law extraction and associated physics

When we are Joule heating the graphene flake, we can calculate exactly how much power we are sending in (because we can measure the resistance R across the heater and the ground along with the exact DC current we are applying, giving us the Joule heating I^2R) while simultaneously monitoring its temperature. It is useful to plot the power applied as a function of temperature. This is because the power dissipated through electron-phonon cooling scales as:

$$P = \Sigma(T_e^{\delta} - T^{\delta}) \tag{5.5}$$

where Σ is the electron phonon coupling constant integrated over the area of the device, T_e is the temperature of the electron gas, and T is the phonon bath temperature, which we assume to be the temperature of the mixing chamber of the fridge. Σ and δ can provide us a lot of insight into the physics of thermalization. Before we dive into the fitting done for our data, it is useful to look at a summary of the extracted parameters reported in literature. As is obvious from Table 5.1, unfortunately, the electron-phonon coupling constant varies wildly between studies (by several orders of magnitude) making it difficult to obtain clarity about the microscopic processes involved in thermalization.

Study, Year	System	Limit	Exponent	Coupling Constant
Ref. 160, 2012	Graphene on SiO_2	Dirty	$T^{2.7\pm0.3}$	$0.07 W/m^2K^3$
Ref. 169, 2012	Graphene on hBN	Dirty	T^4	$0.002 W/m^2K^4$
Ref. 170, 2013	Graphene on hBN	Clean	T^3	$1\text{-}3 W/m^2K^3$
Ref. 164, 2019	Graphene on SiO_2	Dirty	T^4	$0.32 W/m^2K^4$
Ref. 168, 2019	Graphene between hBN	Clean	T^3	$2.4 W/m^2K^3$
Ref. 155, 2019	Graphene between hBN	Clean	T^3	$10 W/m^2K^3$

Table 5.1: Summary of power vs temperature behavior reported in literature.

Unlike previous measurements which showed a T^3 or T^4 dependence [157, 160, 163, 164, 155], we do not see a clear temperature dependence on the electron side with a reasonable exponent and T^5 dependence on the hole side. Although this could be due to aluminum, technique, cleaner sample, or lower temperatures, we believe it's because of quasi-particle recombination on the electron side and edge dominant scattering on the hole side, as we will discuss.

We have also been able to explore the temperature dependence of the holes for the first time in this work. It is well known that the hole side has worse contact

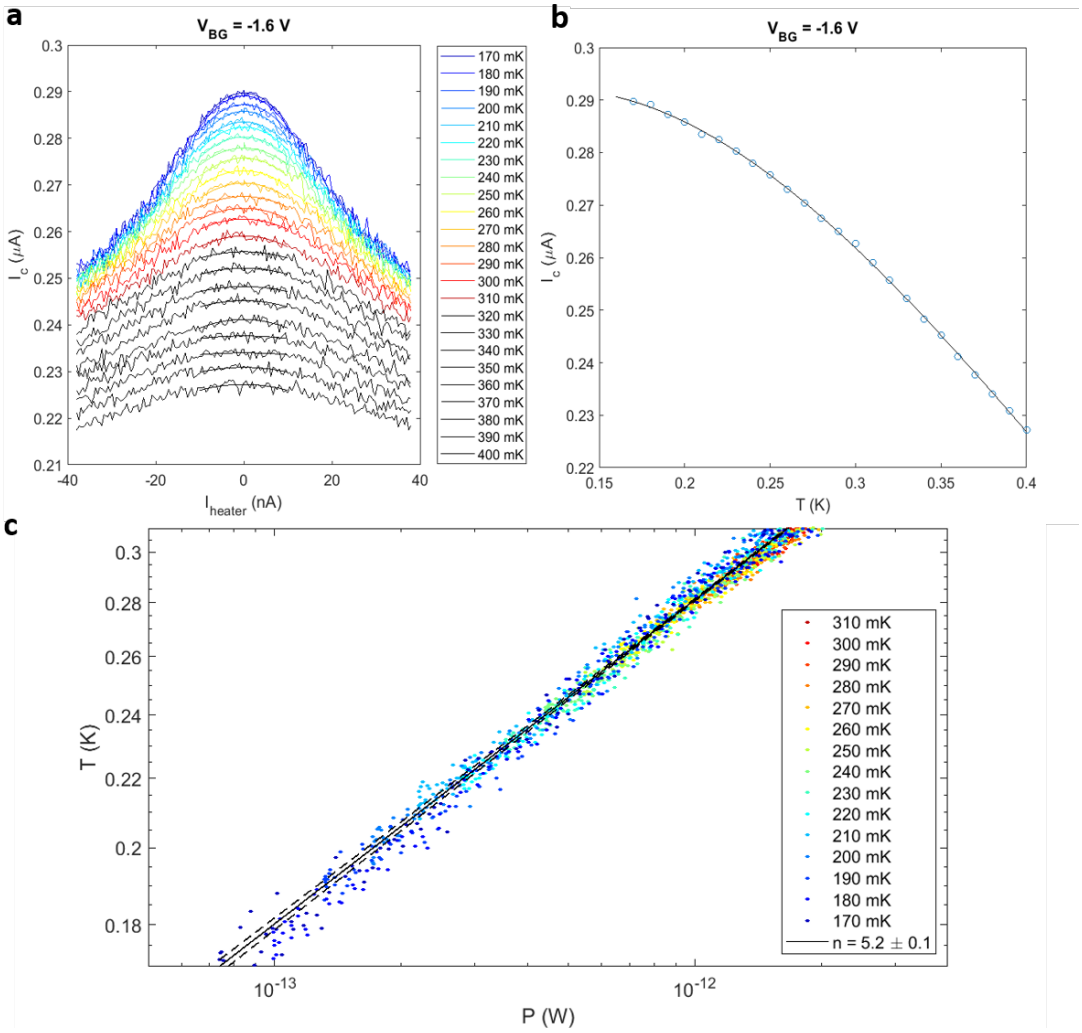

Figure 5.10: Fit of power vs temperature for the electron side. The T^5 dependence is different from what has been reported in literature for 2-D metals but is consistent with a resonant scattering mechanism proposed for graphene in [167].

transparency than the electron side, and therefore the critical current values are a lot lower. In our case, even though the critical current on the hole side is a lot lower than the electron side, it is still high enough that we see a resolvable resonance, allowing us to monitor the behavior of the hole side.

A likely mechanism for the discrepancy between the expected temperature vs power dependence is the scattering of holes (or electrons) not occurring in the bulk which is assumed by most transport studies. Indeed, local thermometry measurements demonstrate that the edges are playing a more prominent role than the bulk in cooling the graphene sheet, in contrast to several previous transport studies [165, 166]. Our

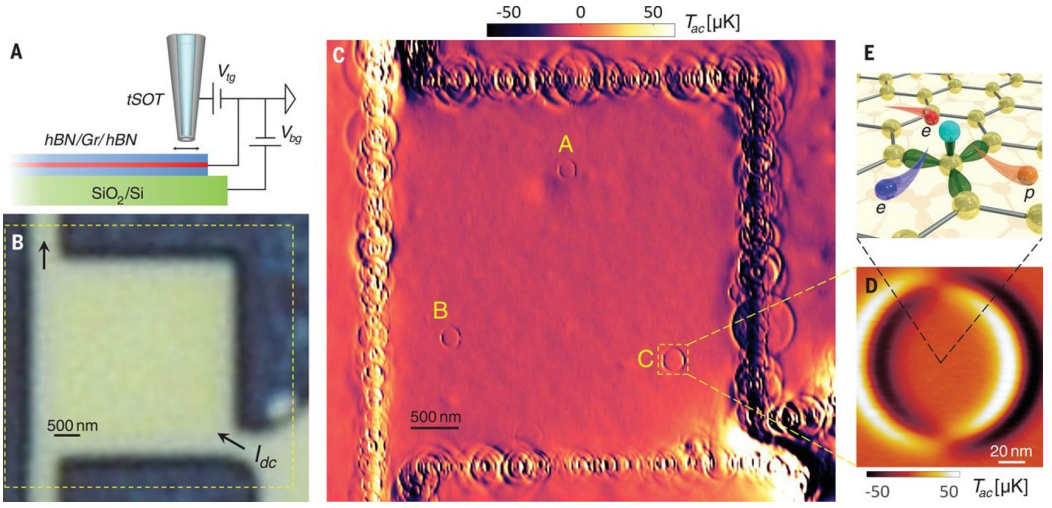

Figure 5.11: Dissipation of heat by electrons at edges and resonant scatterers in the bulk as imaged by a Scanning Squid on Tip (SOT) setup [166]. Reprinted with permission from the copyright holder, The American Association for the Advancement of Science.

data from the hole side is more consistent with resonant scattering on the edges as proposed by Kong *et al.* [167], where

$$P \propto (T_e^5 - T_{bath}^5)$$

A complication regarding the power laws that has not been fully resolved in existing literature is the observation of T^3 dependence when the graphene is actually in the "clean" limit [155, 168] and T^4 dependence when the graphene is in the "dirty" limit [160, 164]. This observation contradicts theoretical predictions for bulk electron-phonon coupling based thermalization. The discrepancies are attributed to supercollisions or disorder [169, 170, 168], but the picture is not clear for graphene encapsulated by h-BN [171]. Additionally, according to several transport measurements, thermalization in graphene Josephson junction is solely driven by the electron-phonon interaction, as the diffusion of unpaired electrons or holes appears to be suppressed due to superconducting gap. However, the extracted values of e-ph coupling appear to be roughly two orders of magnitude larger than theoretical predictions [163, 168]. Therefore, we also calculated the theoretical heat loss through the aluminum leads if the electrons from graphene were to diffuse into the leads (through Andreev reflection) following the theoretical treatment of [172]. As we can see in Fig. 5.13, on the electrons side it is pretty clear that the dominant source of heat loss is the diffusion of hot electrons from graphene into aluminum, whereas on the hole side, the diffusion doesn't seem to play a major role.

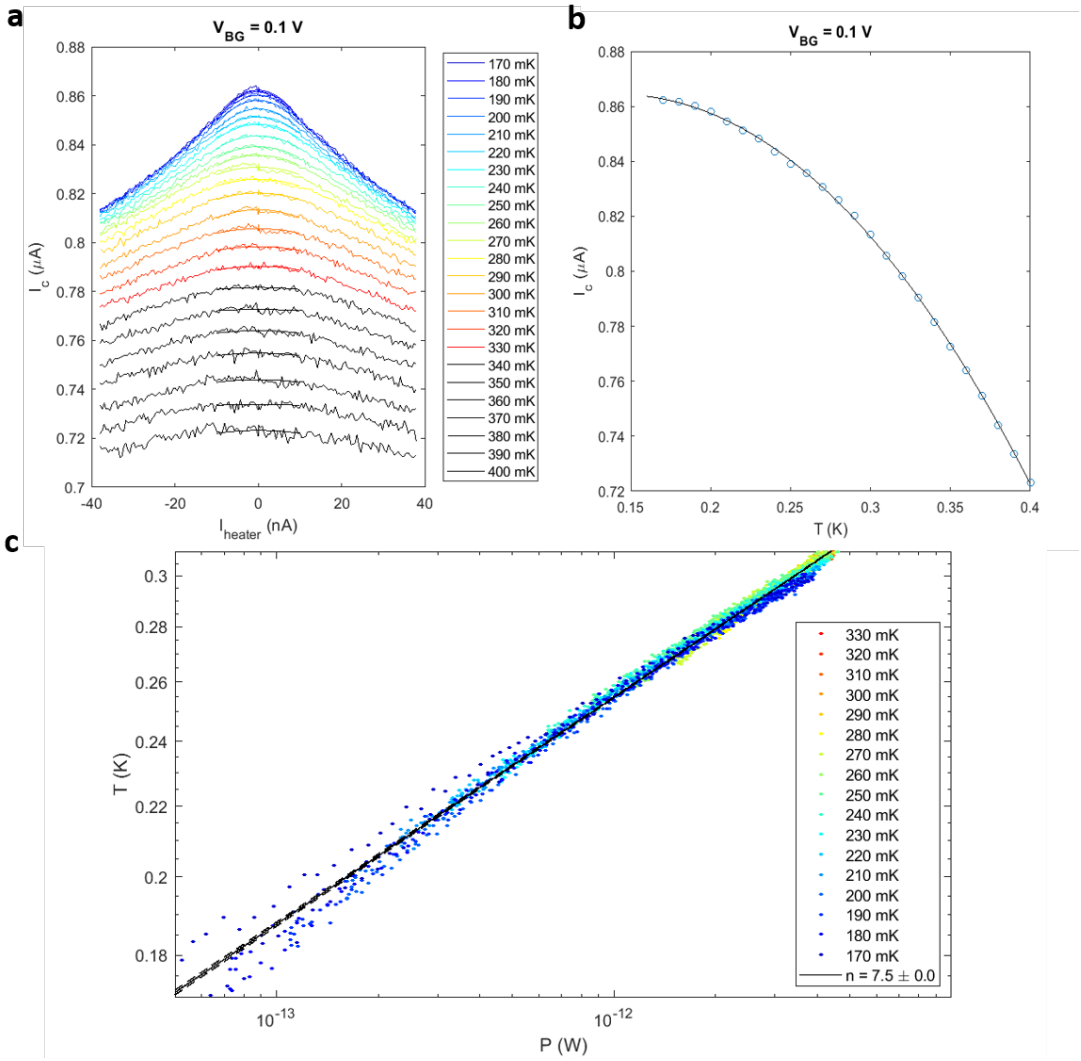

Figure 5.12: Fit of power vs temperature for the electron side. The exponent is unreasonably high suggesting that a mechanism other than electron-phonon coupling based cooling is at play here.

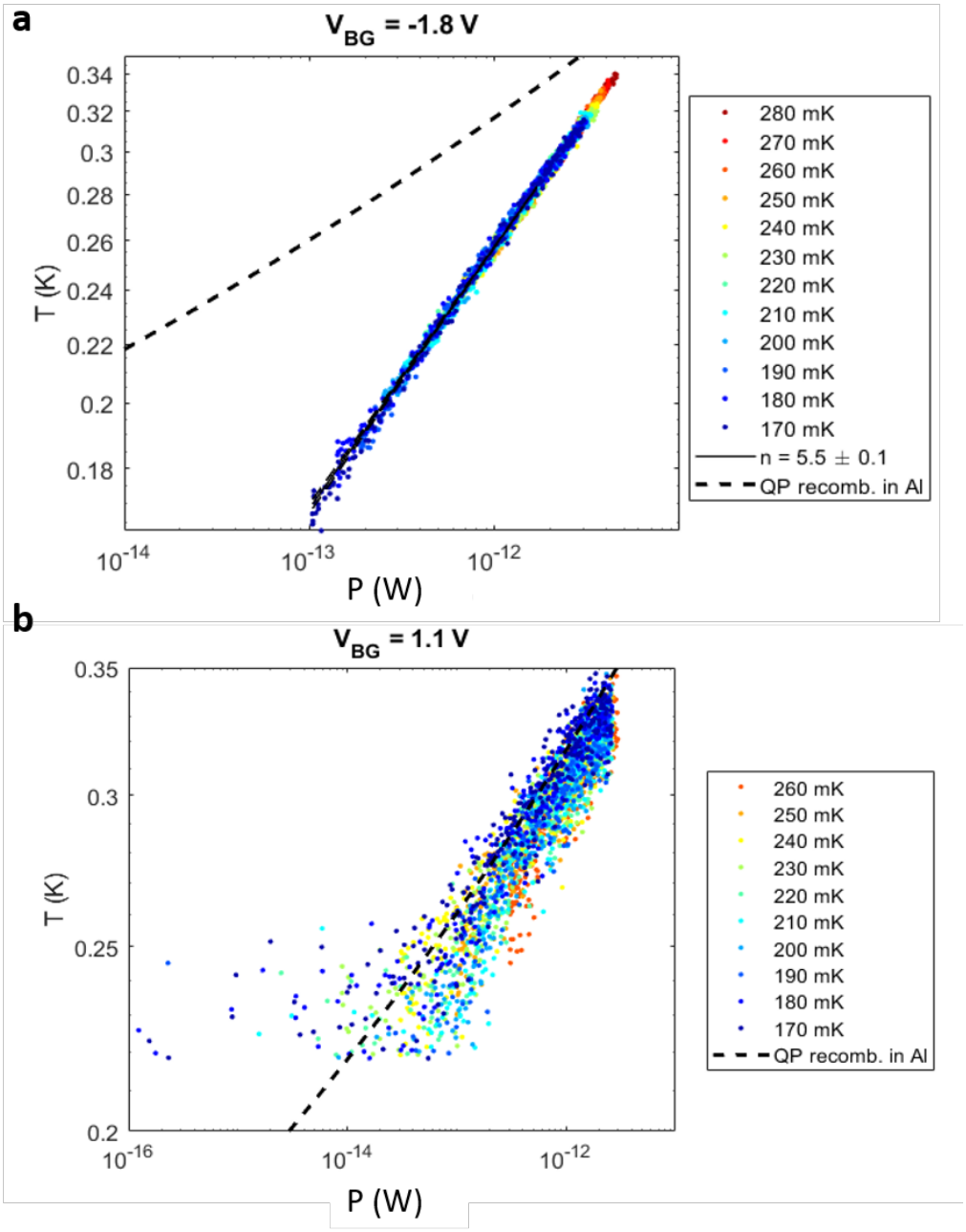

Figure 5.13: **a)** Comparison of power lost through quasi-particle recombination (diffusion of hot electrons from graphene into the superconducting contact) in aluminum and power dissipated through electron-phonon coupling on the hole side. It is clear from the fit that the actual mechanism of energy dissipation is unlikely due to quasi-particle recombination but more due to electron-phonon coupling. **b)** Comparison of power lost through quasi-particle recombination in aluminum and power dissipated through electron-phonon coupling on the electron side. Contrary to the hole side, the actual mechanism of energy dissipation here is likely due to quasi-particle recombination and not due to electron-phonon coupling.

An important disclaimer we need to make here is that the temperature vs power dependence is usually calibrated using at least a decade of temperature change as exemplified by Fong *et al.* [160, 157]. The fits have more of a global nature in temperature compared to thermal conductance, which is limited to a specific point in temperature. However with superconducting contacts (especially aluminum) at low temperatures, it is not always possible to access a big range of temperatures because once the electron temperature exceeds a critical value (usually when the temperature exceeds 1/3 of the superconducting gap Δ of the contacts), quasi-particle recombination increases in the contacts. Using the values shown in Table 5.1, we plot P vs T fits for some representative values found in transport studies on graphene along with fits for our data, both on electron and hole side, as shown in Fig. 5.14. It is clear that our data strongly suggests a mechanism of thermalization in our device different from what has been described in previous transport studies.

However, we can claim with a lot of confidence that in this "limited" temperature range, the data strongly suggests that the temperature dependence of both electrons and holes doesn't follow the conventionally expected exponents. Our belief is that the thermalization of electrons in ballistic graphene is very poorly understood, and the details of the microscopic mechanisms leading to heat loss for electrons are missing. This leaves room for a lot of exploration in further experiments with more optimized geometry and different superconducting electrodes such as Nb or NbTiN.

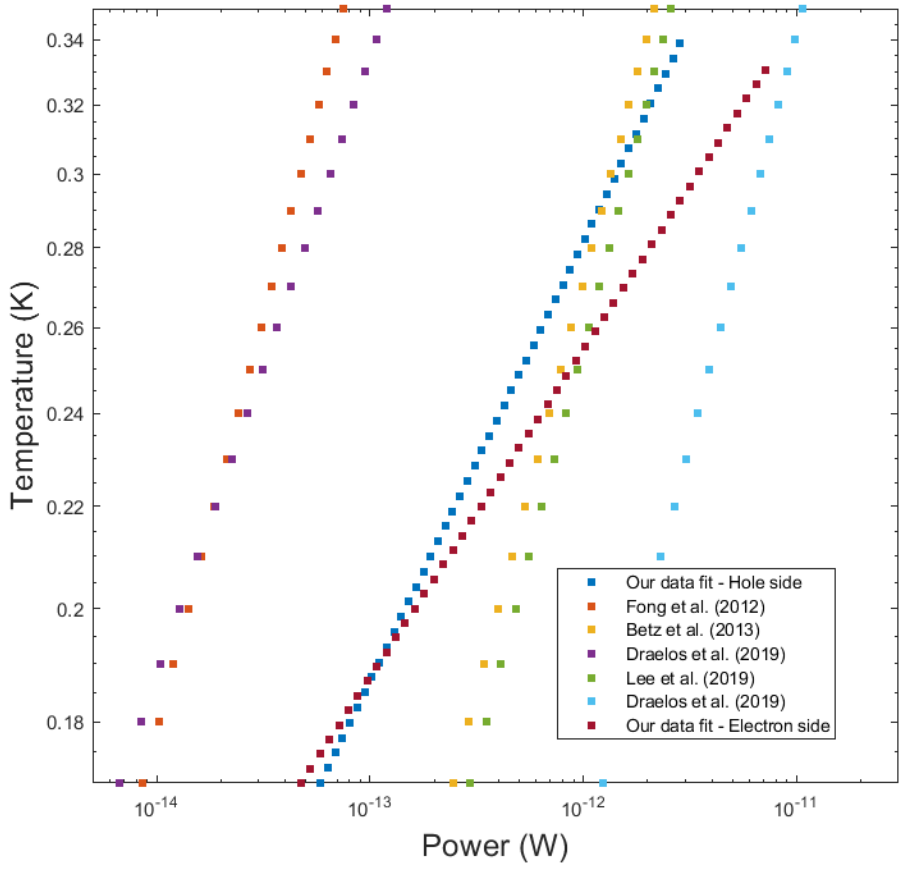

Figure 5.14: Comparison of our data to values reported in literature. It is clear that our data strongly suggests a mechanism of thermalization in our device different from what has been described in previous transport studies

Chapter 6

OUTLOOK

While a lot of new phenomena have been discovered in Twisted Bilayer Graphene (TBG), the underlying physical mechanisms remain highly disputed. Here, we first discuss experiments which can possibly shed more light on the electronic states in TBG with a combination of novel device geometries and new measurement techniques accessible to us. We then move to proposals for stabilizing exotic electronic phases in other vdW materials including single layer graphene.

6.1 TBG encapsulation with other materials

It is our hope that this work has made clear that the choice of substrate plays a crucial role in stabilizing different phases in TBG along with physical effects such as decreasing the angle disorder. A simple extension to TBG devices after TBG/WSe_2 devices would be to encapsulate TBG with a 2-D ferromagnetic insulator such as $CrBr_3$ (Curie temperature of about 37K). The main goal here would be to stabilize ferromagnetism in TBG (leading to a quantized conductance) without the need to align it with h-BN, which complicates the fabrication process. A reliable way to achieve the Quantum Anomalous Hall (QAH) phase in TBG would be highly prized in the community. Additionally, it would be very exciting if the magnetism could co-exist in the same device with superconductivity, assuming that the magnetism can exist without breaking the $C_2\tau$ symmetry, which appears crucial for the existence of superconductivity [127, 173].

6.2 Shot noise measurements in TBG

There has been significant debate in the theoretical community about the importance of the so-called "strange metal" state around half-filling that precedes the development of superconductivity [174, 99] and its possible connection to the superconducting phase. Some of the questions that plague the understanding of superconductivity in TBG are similar to questions posed in high T_c superconductors. More specifically, there are two opposing points of view regarding the charge of the carriers above the superconducting transition temperature in TBG: one believing that electrons have some mechanism of pairing above the critical temperature of superconducting TBG, and the other believing that they exist in the form of individual carriers. In the high

T_c Cuprate system, shot noise was recently used to uncover some secrets of the "pseudogap" state.

Shot noise is the intrinsic fluctuations in current caused by charge carriers moving through a device, and its intensity depends on the charge of these carriers. A landmark experiment used the measurement of shot noise to observe the 1/3 charge carrier value of the Loughlin fractional quantum hall state [175]. More recently, a similar experiment in the Cuprates, studied the nature of the pseudogap state [176] in LSCO/LCO/LSCO tunnel junctions. This beautiful experiment demonstrated that in the pseudogap state, the shot noise was substantially higher than theoretically expected from single particle tunneling. This supports the existence of the so called "pair density wave" phase where the charge carriers are paired well above the superconducting transition temperature, pointing to a deep connection between superconductivity and the pseudogap phase in this material system.

A requirement for this experiment would be a device with relatively high homogeneity of twist angle between multiple pairs of electrodes to eliminate effects that could arise due to disparate superconducting pockets. Narrow top gate fingers (40-50 nm) would deplete regions of superconducting TBG out of the superconducting phase, yielding a Josephson Junction. One could then measure the shot noise across this junction to answer the questions about the existence of pairing in the strange metal phase in TBG. From a fabrication standpoint, this is one of the most challenging experiments proposed here. However, based on the relatively high yield of superconducting TBG/WSe_2 devices, this experiment should be possible in the near future.

6.3 Simultaneous electron transport and Scanning Tunneling Microscopy (STM) measurements in TBG

DC transport measurements on TBG that have been discussed in this work and in literature are looking at TBG on a global scale where the properties of the TBG area between a pair of contacts are some "average" of the total area (usually about $1\mu m^2$). Because the typical moiré length in superconducting TBG is of the order of 10 nm, this leaves a lot of microscopic details rendered inaccessible by transport measurements. Scanning Tunneling Microscopy (STM) is a tool that can study the electronic properties of materials on a scale from the atomic level to few hundred nm^2, which makes it ideal to help us understand the mechanisms of exotic phenomena in TBG. Unfortunately, so far, STM studies have not been able to observe superconductivity

in TBG or magnetism. One of the biggest obstacles in bridging this gap between DC transport and STM measurements has been the incompatibility between superconducting transport samples and STM samples. More specifically, superconducting TBG devices always have a layer of insulating h-BN on top to protect the graphene from contamination during device processing, whereas STM samples need to able to tunnel into the graphene layers from the top, which is impossible with a few nm thick layer of insulating h-BN. Encapsulation with monolayer WSe_2 offers a path to making compatible devices. The entire hetero-structure would be made by having just a WSe_2 monolayer on top of the TBG (no h-BN). The WSe_2 monolayer would protect the WTe_2 during device processing but also allow tunneling experiments. First, these devices would be measured in a dilution fridge to check for superconductivity and to identify promising electron density ranges. Then they would be loaded into the STM to study areas that were superconducting in transport at the correct densities. This would allow for a thorough investigation of the percolation paths in TBG along with the determination of the superconducting gap size as well as its nematic behavior.

6.4 Bolometry and heat capacity measurements of TBG

Theoretical studies on heat capacity of twisted bilayer graphene have shown intriguing results with regards to the dependence of heat capacity on temperature [177]. It has been predicted that phonons can be engineered by twisting atomic planes to change the specific heat capacity significantly at low temperatures. Utilizing a geometry used in Chapter 5, but replacing monolayer graphene with TBG of different twist angles, could provide a lot of insight into the physics of phonons in this system and the dependence of electron-phonon coupling on the twist angle.

From a detector point of view, superconducting TBG in itself provides an intriguing platform for single photon detection. Traditionally, Transition Edge Sensors (TES) have been used to detect incoming radiation by relying on the steep transition to a resistive phase upon absorption of photons, which raises the temperature of the electron gas. Because the heat absorbed is quickly distributed to the entire electron bath, the detection limits of the sensor are dependent upon the electronic heat capacity of the calorimetric materials. Due to the ultra-low carrier density at which superconductivity is achieved in TBG (which are three to four orders of magnitude smaller than conventional superconducting thin films used in TES bolometers), it has been proposed that TBG can serve as a single photon detector upto the THz range [178]. Additionally, because the resistance jumps in TBG at

the superconducting transition temperature can be of the order of a few kΩs to few hundred kΩs, it is possible to obtain large jumps in voltage providing for an easier readout. It's clear that 2-D materials have a lot of inherent advantages for being deployed in calorimetry and single photon detection, and with optimization, they have the potential to revolutionize the world of quantum sensing.

6.5 Quantum Spin Hall effect in graphene through screening

One of the most seminal predictions about graphene that has never been experimentally realized is the Quantum Spin Hall Effect [33]. Theoretical calculation predicted that at sufficiently low temperatures and energies, graphene would host edge states where spin and momentum would be locked in a way that would prevent backscattering. In addition, they predicted that the bulk would be gapped. There are two main reasons however, that have made it difficult to observe this effect in graphene. The intrinsic spin-orbit coupling in graphene is very small (few hundred μeV), which makes it very difficult to gap out the bulk at experimentally accessible low temperatures. Additionally, the electron-electron interactions in graphene break the SU(4) symmetry that makes the system unstable towards a spin hall phase. Although this novel state of matter hasn't been realized in graphene yet, it has given rise to a burgeoning field of condensed matter physics which is dedicated to finding new materials that host these states.

Recently, it was shown that graphene could host helical quantum hall edge states [179]. The observation of this state had also been hindered by electron-electron interactions in graphene. However, through clever device design, the authors were able to screen out the interactions. This was achieved by bringing a material ($SrTiO_3$) with an extremely high dielectric constant around (10,000 at low temperatures) in close proximity to graphene, thereby separating the $SrTiO_3$ from graphene by a thin layer of h-BN (about 3nm thick). The thin h-BN ensures high mobility in graphene but is not thick enough to wash out the screening effect of $SrTiO_3$.

A schematic for the proposed experiment is shown in Fig. 6.1.

In the proposed experiment, one would boost the spin orbit coupling in graphene by proximitizing it with WSe_2 on the top and reducing the electron-electron interactions by bringing $SrTiO3_3$ close to graphene on the bottom separated by thin h-BN. Combining these two techniques should be a promising avenue for observing the Quantum Spin Hall state in graphene.

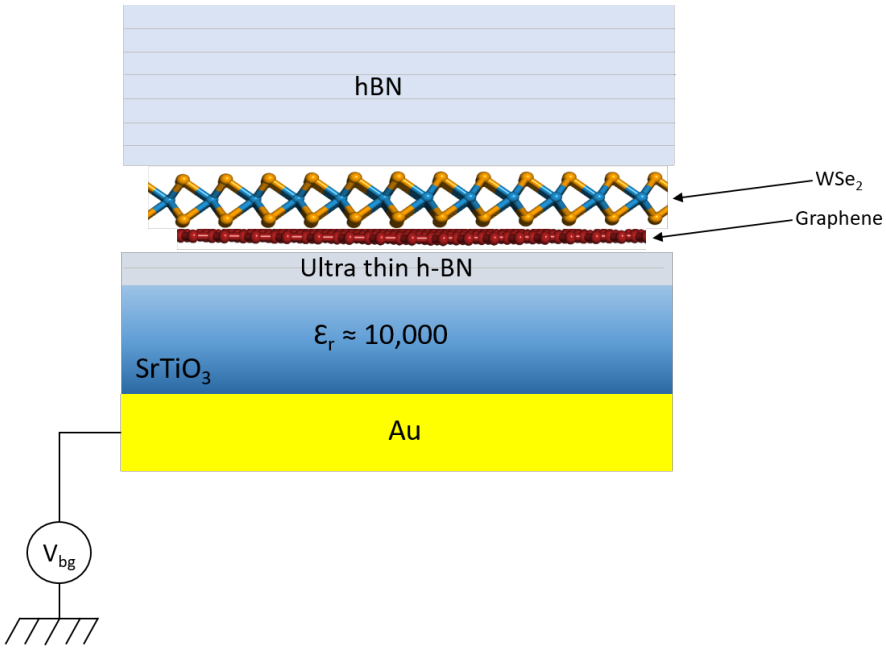

Figure 6.1: Proposed device geometry for QSH effect in graphene.

6.6 Simultaneous electron transport and Scanning Tunneling Microscopy (STM) measurements in WTe_2

WTe_2 is another interesting material (we touched upon it in Chapter 1, but we haven't discussed it in detail in this thesis) for this experiment. The bulk material is a Weyl semimetal, and the monolayer was recently shown to be a Quantum Spin Hall Insulator (QSHI) [42, 43]. Moreover, upon doping this material with electrons through a gate, it exhibits superconductivity [180, 181]. The nature of superconductivity in this exotic material is also unknown at this point and has not been observed in an STM so far. This material is very air sensitive and needs to encapsulated by h-BN for transport measurements. The idea for WTe_2 experiment would be along the same lines, a monolayer of WTe_2 would be exfoliated inside a glovebox (< 0.5 ppm O_2 and H_2O). The monolayer WTe_2 would be picked up by a monolayer of WSe_2 and then stacked on top of a h-BN crystal. This heterostructure would be made into a device wiith electrodes that can be measured in the STM. This would open a whole new class of air sensitive vdW materials to be explored by the STM.

6.7 vdW Josephson junctions with air-sensitive materials

As mentioned above, monolayer WTe_2 is very interesting as it is a Quantum Spin Hall Insulator, which, when coupled to a superconductor, can result in a topo-

logical Josephson junction. In a topological Josephson junction, it is possible to engineer topological zero energy modes (Majorana modes) by applying a perpendicular magnetic field [182]. These Majorana modes are crucial for the realization of topological quantum computing. The biggest issue is being able to couple an air sensitive monolayer to a superconductor while maintaining a transparent interface. Conventional lithographic techniques don't work because they either degrade the monolayer by exposure to air or leave residues on the superconductor surface which limits the transparency of the contacts. The other method used frequently in vdW heterostructures utilizes "edge contacts" between 2-D layers and 3-D metals [109]. Unfortunately, this works well only for metals or semi-metals, limiting its use in the case of WTe_2.

Focused Ion Beams (FIB) that use inert gas ions as beams present an exciting opportunity in this context. A beam of high energy ions (Helium or Neon) can remove material from thin films with very high precision. With such a FIB, it is possible to cut thin flakes of superconductors without damaging them and obtaining very narrow channels (10nm-70nm) of empty space between two superconducting regions. This technique was pioneered in 2015 by Cybart *et al.* [183] by using a He ion beam for YBCO based junctions. Some initial devices fabricated in this way that used Neon ions instead of Helium ions are shown in Fig. 6.2. We discovered that helium ions don't work well for cutting $NbSe_2$, even after the flake is optically fully cut through into two, the two parts remain electrically connected, which could be a result of carbon deposition during the cutting process. The quality of the separation achieved here is a big function of dose and incident Neon ion beam energy, and requires a lot of optimization (which is the trickiest part of this proposal). Also, the top surface of the superconductors that are usually used ($NbSe_2$) can get partially oxidized during the transfer from the glovebox to the FIB and back, resulting in reduced transparency of the contacts. However, if these issues are resolved, it will open doors to making vdW Josephson junctions with a lot of other air sensitive 2-D materials, such as black phosphorous, indium selenide (InSe), and vanadium diselenide (VSe_2).

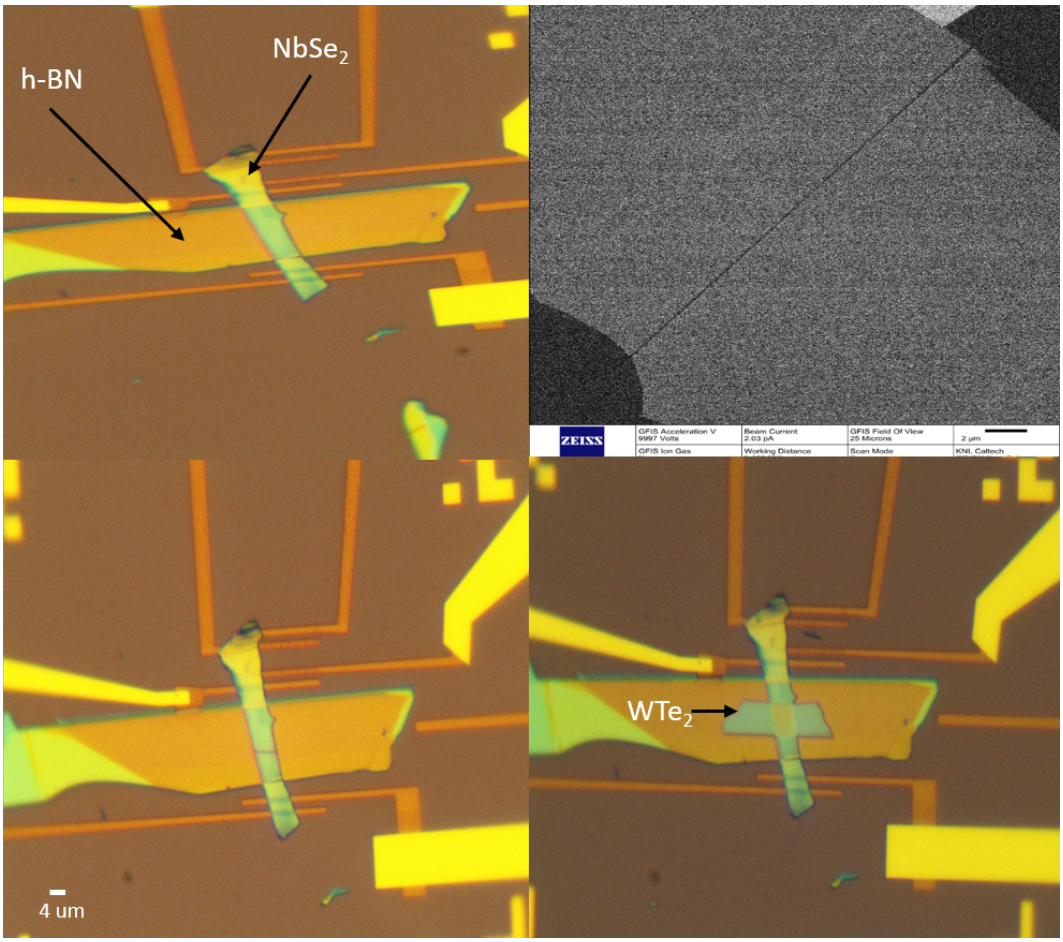

Figure 6.2: Optical and SEM images showing different steps towards making a topological vdW junction. The SEM image shows the 30 nm cut in the $NbSe_2$ layers caused by a 30keV Ne ion beam.

Appendix A

FABRICATION OF GRAPHENE-RESONATOR DEVICES

Fabricating the on-chip resonator for inductive readout of graphene temperature.

1) Deposition of superconductor and dicing of wafer: We start with a commercially available undoped silicon wafer that has 300 nanometers (nm) thermally grown silicon oxide on it. The wafer is put inside a sputtering machine where a few hundred nanometers of Niobium Titanium Nitride (NbTiN) is sputtered on it using a commercially available NbTiN sputtering target. The transition temperature for our NbTiN thin films is typically around 14 Kelvin. Note that, any high transition temperature superconductor can replace NbTiN in this part of the process. Subsequently, the wafer is diced into smaller pieces (chips) that can fit inside the experimental apparatus, typically 5 millimeters (mm) x 7 millimeters (mm) using a handheld diamond scriber pen.

2) Resist preparation and pattern writing: Commercially available electron beam resist (e-beam) is then spun on these chips individually. In our case, we have used ZEP 520-A made by Zion chemicals, but that can be easily substituted by other available e-beam resists. A few drops of the resist were placed on each chip, and they were spun at 5000 revolutions per minute (rpm) for 90 seconds. These chips were then put on a hotplate and baked at 150° Celsius, which ensures a uniform coating of the resist. Once the baking is done, the chips are transferred inside an electron beam writing instrument. Patterns for the resonator design are inscribed into the resist by the electron beam with a beam current of 1 nanoamperes (nA) and a dose of 350μC/cm^2.

3) Developing, etching, and cleaning: After the writing is done, the chips are dipped in a developer solution (commercially available ZED N50 in our case) for 90 seconds and then dipped in Isopropyl Alcohol (IPA) for 30 seconds before being blow dried by a nitrogen gun. To make a smoother profile on the resonator, we put the chips on a hotplate at 150° Celsius again for about 3 minutes, which rounds the edges. To further clean up resist residues before etching, we clean the chips in a mild O_2 reactive ion plasma for 45 seconds with the following parameters: 50 sccm O_2 flow, 60mtorr O_2 pressure, and 40 Watts (W) RF power. Then the resonator pattern is etched thorough a combination of Sulfur Hexafluoride (SF_6) and Argon reactive ion

etching with the following parameters: SF_6 flow 20 sccm, Argon flow 10 sccm, chamber pressure 15mtorr, and RF power 80W. 100 nm of NbTiN is etched through this process in roughly 120 seconds. The chips are finally cleaned off in hot N-Methyl-2-Pyrrolidinone (NMP), at 80° Celsius for an hour. A mild O_2 clean (50 sccm O_2 flow, 60mtorr O_2 pressure, and 40 Watts (W) RF power for 60 seconds) is performed on the completed resonator chips before transferring the graphene stack, which helps the adhesion between the chip and the graphene stack.

4) Assembly of graphene stack and fabrication of electrodes: Once the graphene stack is assembled (see stack schematic below) and dropped off onto the resonator chip, we begin the process of making superconducting electrodes to it. Aluminum is chosen as the material of choice because of the reliability of contact transparency between graphene and aluminum. A relatively thick layer of PMMA 950A5 (400-500 nm) is first spun on the graphene at 2000 rpm and then baked at 180°C for 90 seconds. Following this, electrodes are drawn using electron beam lithography with a dose of 1200 μC/cm^2. This high dose is essential to remove the PMMA effectively during development (90 seconds in MIBK:IPA 1:3). Before etching the stack, a quick O_2 plasma is performed to ensure a clean interface between the aluminum and graphene. The etch is a Reactive Ion Etch (RIE) performed in steps of 30s, this is done to avoid overheating of the PMMA [184]. The gases used for the etch are CHF_3/O_2, and the parameters are 40 mTorr pressure, 60 W RF power, and 40/4 sccm of flow (CHF_3/O_2 respectively).

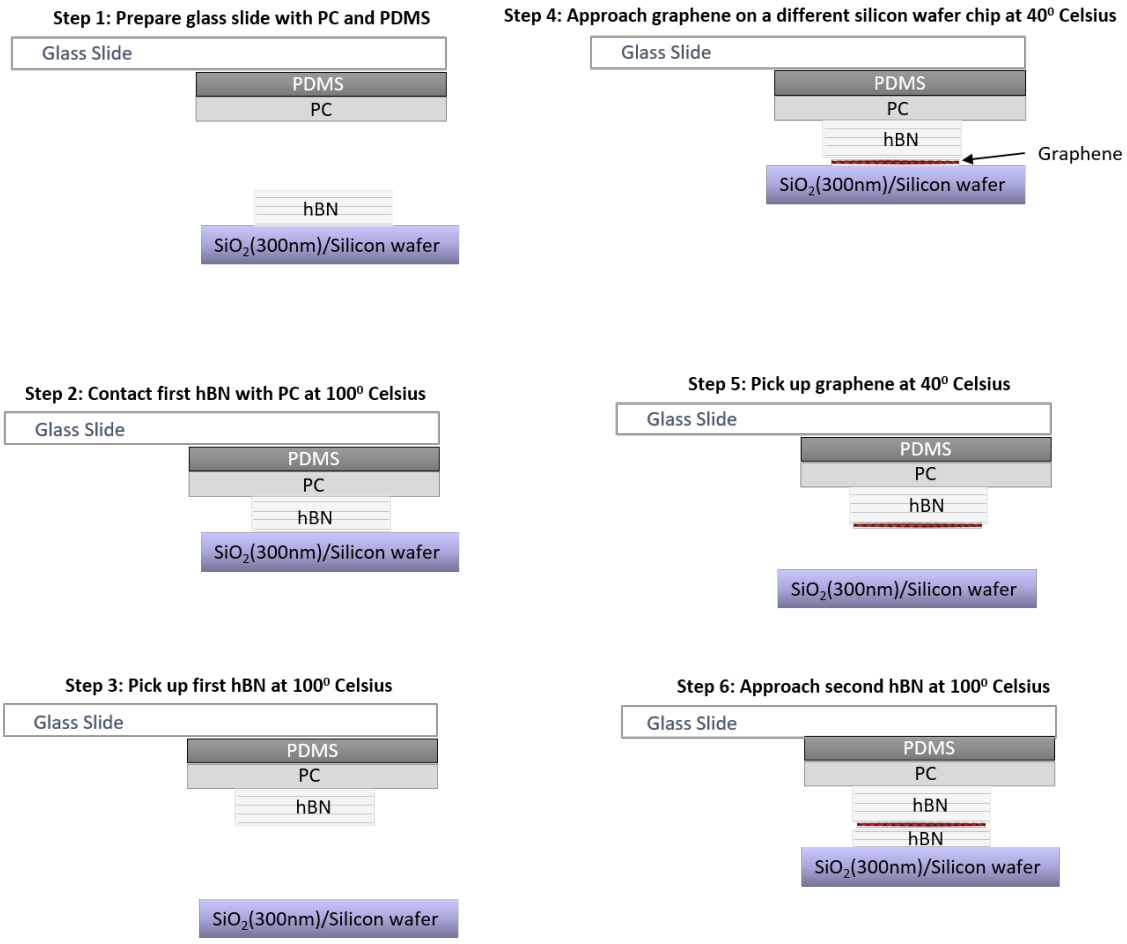

Figure A.1: Stacking schematic for graphene-resonator samples: Part 1.

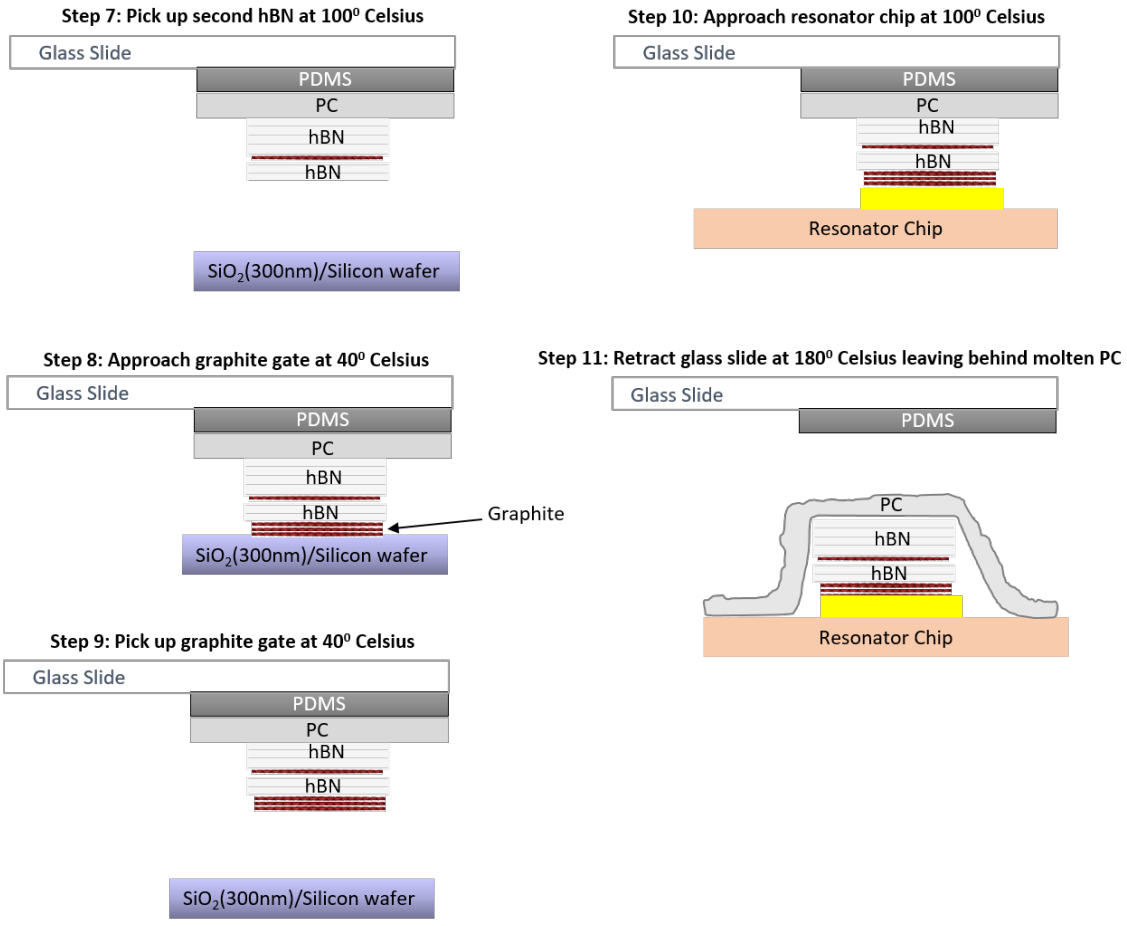

Figure A.2: Stacking schematic for graphene-resonator samples: Part 2.

Appendix B

Modified "tear and stack" method for TBG/WSe_2 devices

The TBG/WSe_2 devices in this work were fabricated using a modified "tear and stack" method, see Fig B.1. First, a thin hBN flake (7-15 nm) is picked up using a propylene carbonate film (PC) previously placed on a polydimethyl siloxane (PDMS) stamp. The PC is made is by dissolving 6% Poly(Bisphenol A) carbonate from Sigma Aldrich (CAS Number: 25037-45-0, item# 181625) in chloroform. Many different PDMS films were tried over the years (including curved stamps cured in the lab), but the commercially available Gel-Pak, Gel Film PF-60-X4 works the best. Then, the hBN is used to pick an exfoliated monolayer of WSe_2 before approaching and "tearing" the graphene. After picking up the first half of the graphene, the transfer stage is rotated by approximately 1.1-1.3° (overshooting the target angle slightly), and then the second half of the graphene is picked up, forming the TBG.

Care was taken to approach each stacking step extremely slowly and at a high enough temperature (90°C) to minimize the formation of bubbles while avoiding the risk of twist angle relaxation. See Fig. B.1 for a representative image of the stack on PC. In the last step, a thicker hBN (30-70 nm) is picked up, and the whole stack is dropped on a predefined local gold back-gate at 90°C while the PC is released at 165°C. The PC is then cleaned off with N-Methyl-2-Pyrrolidinone (NMP). The PMMA bake is also performed at low temperatures for these samples (110°C) for about 2 minutes to prevent twist angle relaxation. A single layer of PMMA 950 A4 spun at 1500 rpm works well for both etching and contact deposition.

The final geometry is defined by dry etching with a CHF_3/O_2 plasma (40mtorr pressure, 40/4 sccm flow respectively and 60W RF power resulting in an etch rate of about 28 nm/min) and deposition of ohmic edge contacts (Ti/Au, 5 nm/100 nm). It is important to note that the plasma chamber was pre-cleaned with O_2 for about 20 mins every single time an etch was performed, which maintained the accuracy of the etch rate and ensured clean edges upon etching. We have used both commercial (HQ graphene) and lab-grown WSe_2 crystals (from University of Washington) and found no obvious difference in the resulting quality of devices.

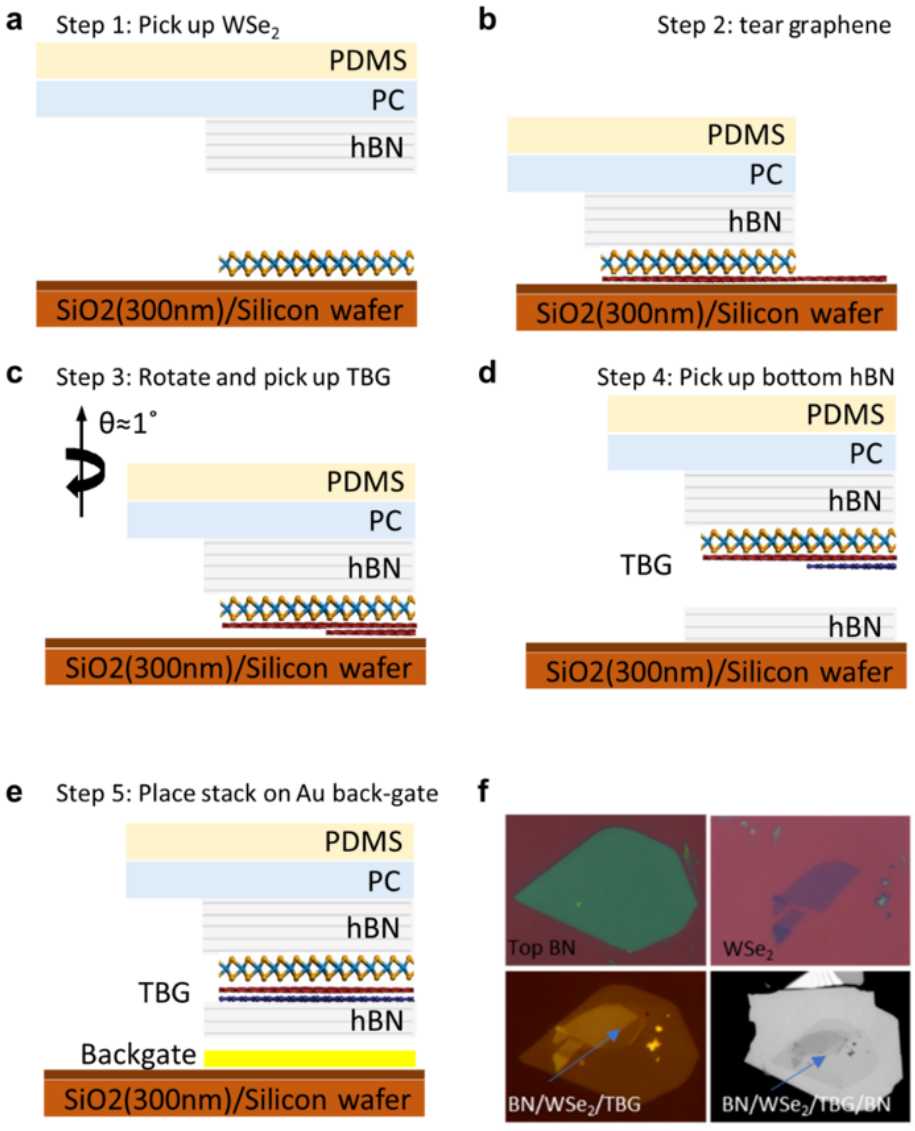

Figure B.1: Assembling TBG/WSe_2 stacks.

Appendix C

SETUP FOR HIGH FREQUENCY MEASUREMENTS

The figure below shows in more detail the configuration of the attenuators, amplifiers, and DC lines used for the experiment discussed in Chapter 5. As the probe powers that we use are fairly small (around -110 dBm), the RF line going into the sample is heavily attenuated. The signal coming out of the device is amplified first by a 4K cryoamp providing about 30 dB gain and then amplifiers at room temperature outside the fridge that provide an additional 30 dB or so of amplification.

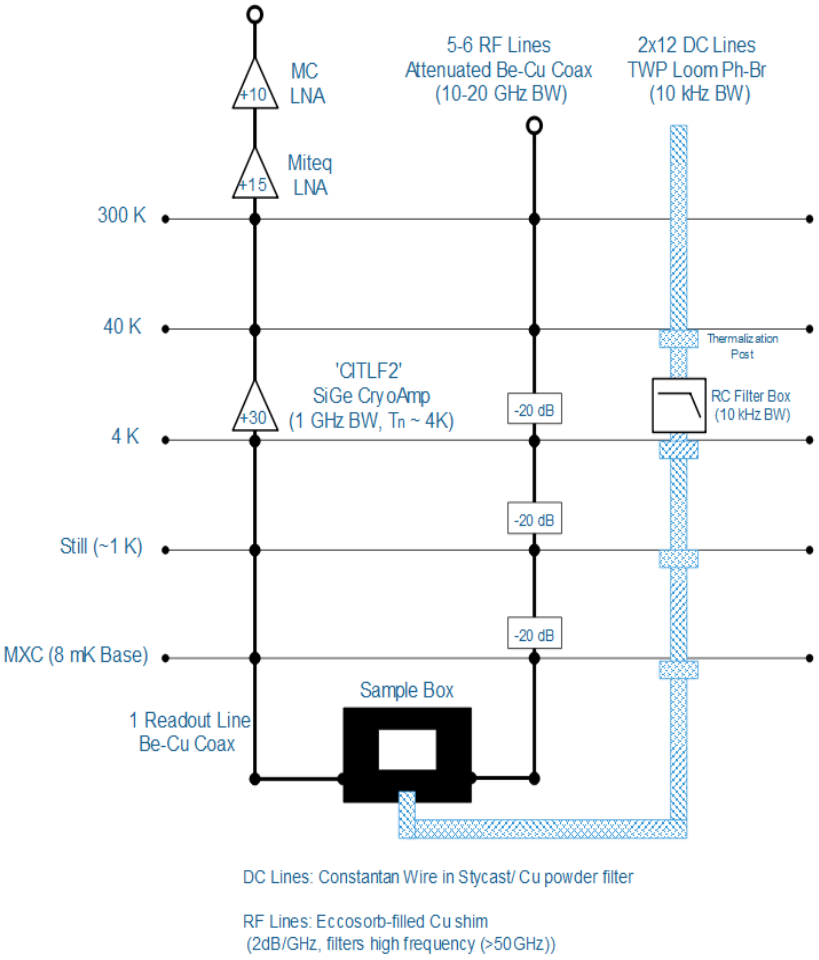

Figure C.1: Fridge wiring.

Appendix D

HEATER RESPONSE FOR DIFFERENT GATE VOLTAGES

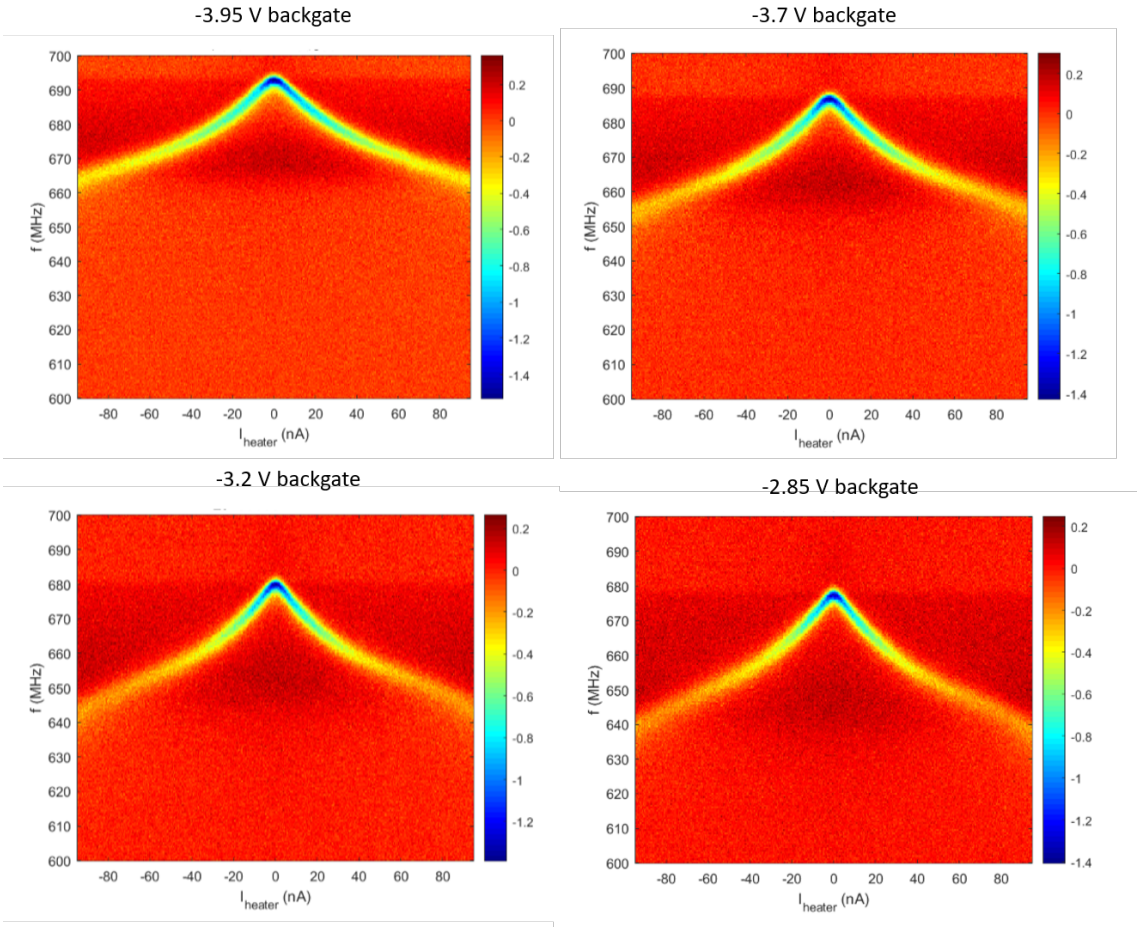

Figure D.1: Heater plots in the hole doped regime.

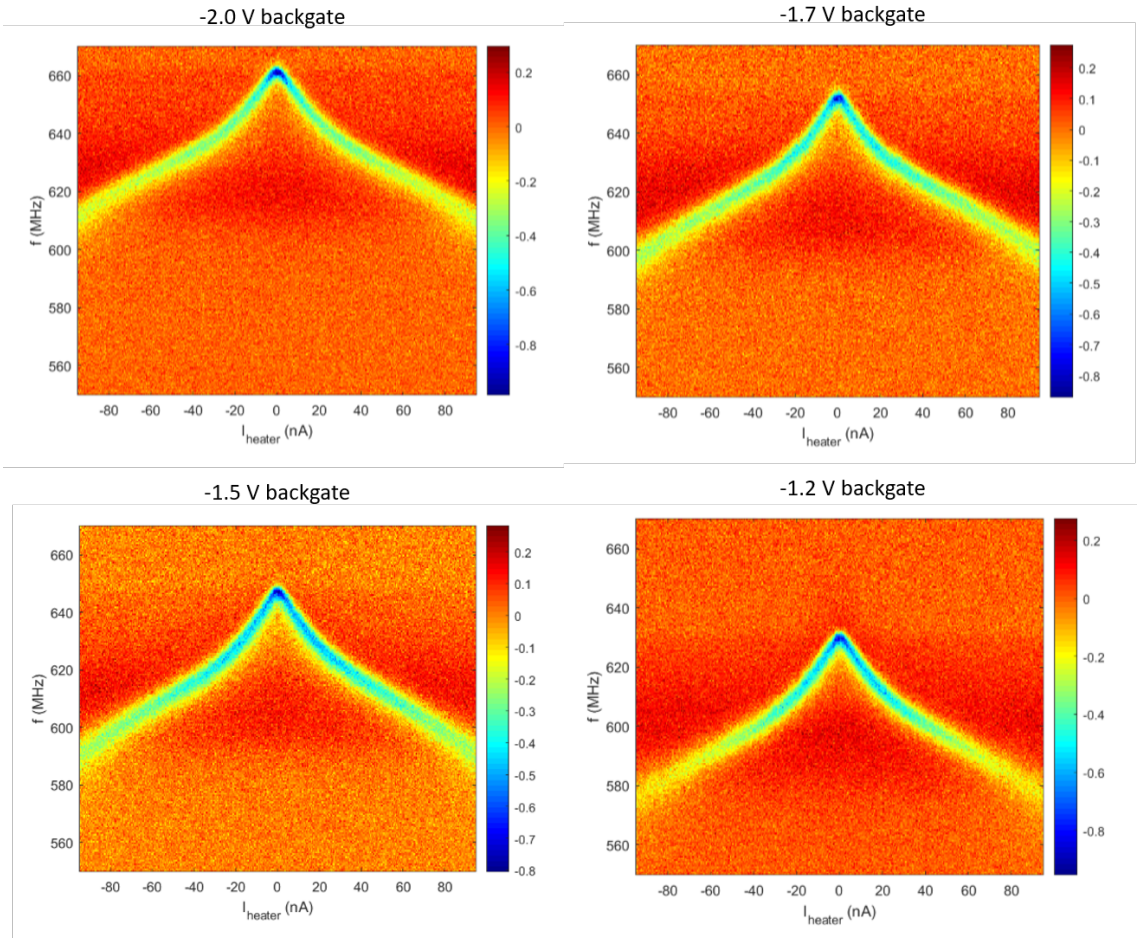

Figure D.2: Heater plots in the hole doped regime and near the Dirac point.

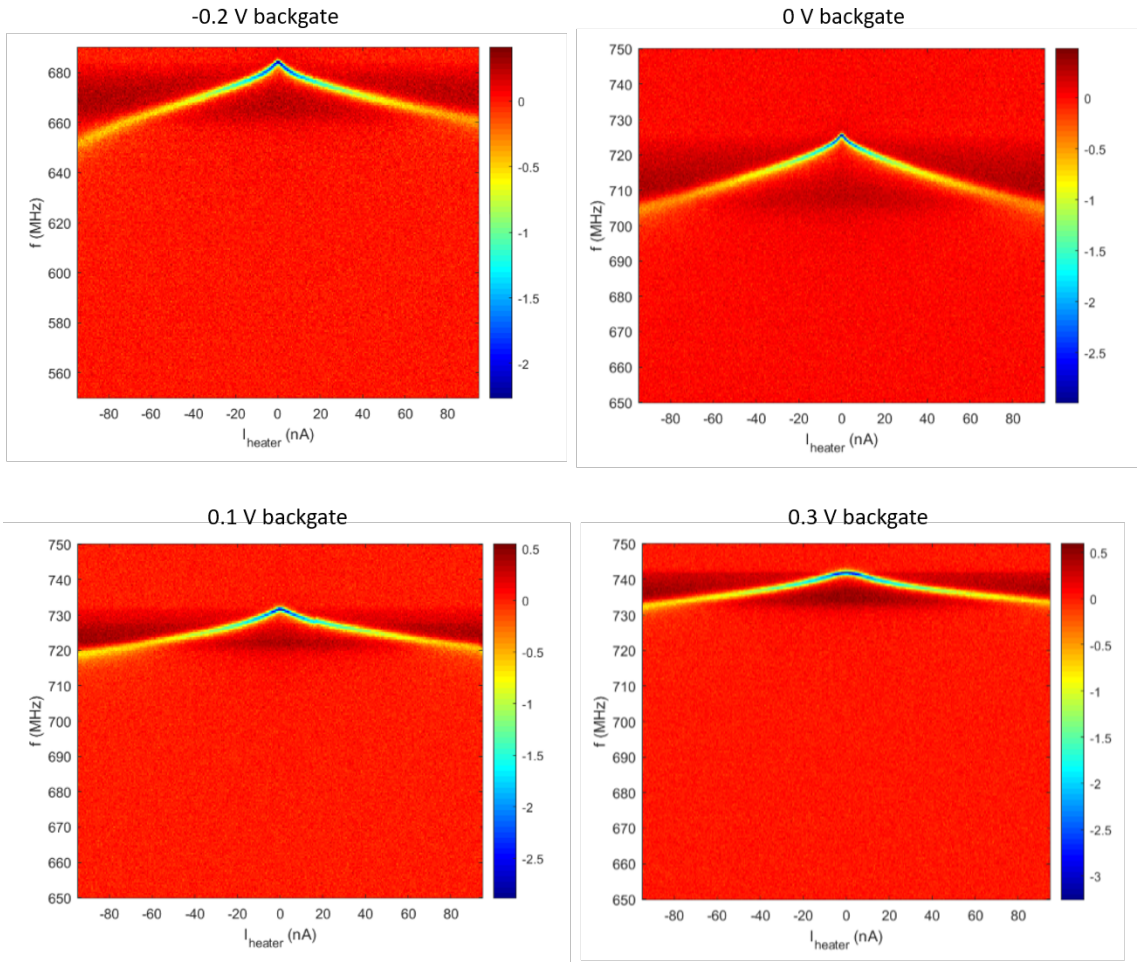

Figure D.3: Heater plots in the electron doped regime.

Appendix E

MODELING OF CRITICAL CURRENT (I_C) VS RESONANT FREQUENCY

Here, we discuss how we modeled a critical current into a resonant frequency for Chapter 5. Using the expression for a quarter wave impedance transformer and the design parameters (obtained from simulations in National Instruments microwave office tool), the coplanar waveguide (CPW) solution is as follows

$$l = 4989 \times 10^{-6} m$$
$$C_k = 0.3 \times 10^{-12} F$$
$$C_0 = 3515 \times 10^{-12} F$$
$$L_0 = 1130 \times 10^{-9} H$$

where C_k is the coupling capacitor to the waveguide and l is the length of the waveguide.

$$Z_0 = \sqrt{\frac{L_0}{C_0}} \tag{E.1}$$

$$\omega_0 = \frac{1}{\sqrt{C_0 \cdot L_0}} \tag{E.2}$$

giving us Z_0 as 17.9298 ohms and ω_0 as 1.58671 x 10^7 Hz.

The L and R termination at the end of the line then determines the resonant frequency as:

$$Z_L = \frac{1}{\frac{1}{R} + \frac{1}{i\omega L}}; \tag{E.3}$$

$$Z_{in} = Z_0 \cdot \frac{Z_L + iZ_0 \tan(\frac{l\omega}{\omega_0})}{Z_0 + iZ_L \tan(\frac{l\omega}{\omega_0})} \tag{E.4}$$

Now we solve for resonant frequency (f) by finding the zero of the imaginary part of Y_{tot} which is,

$$Y_{tot} = i\omega C_k + \frac{1}{Z_{in}} \tag{E.5}$$

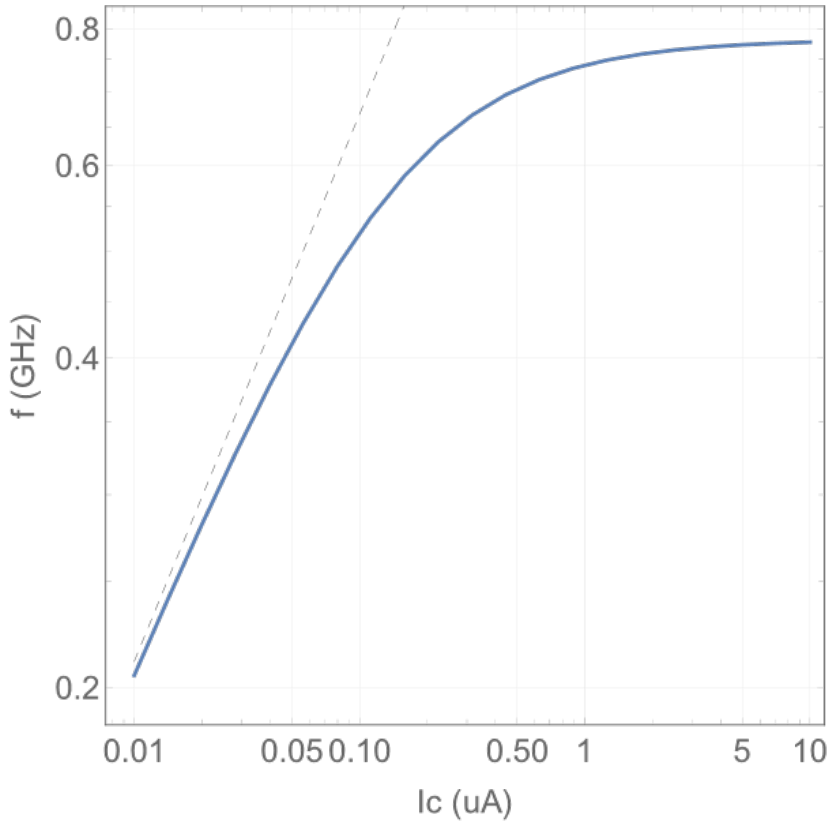

Figure E.1: Estimating the critical current as a function of resonant frequency based on simulated parameters for a quarter wave impedance transformer.

the other parameters used are:

$$R = 1000\ ohms$$

$$L = \varphi_0 / I_c$$

$$\varphi_0 = \frac{2 \times 10^{-15}}{2\pi}$$

Appendix F

DESIGN WINDOW FOR MICROWAVE SIMULATION

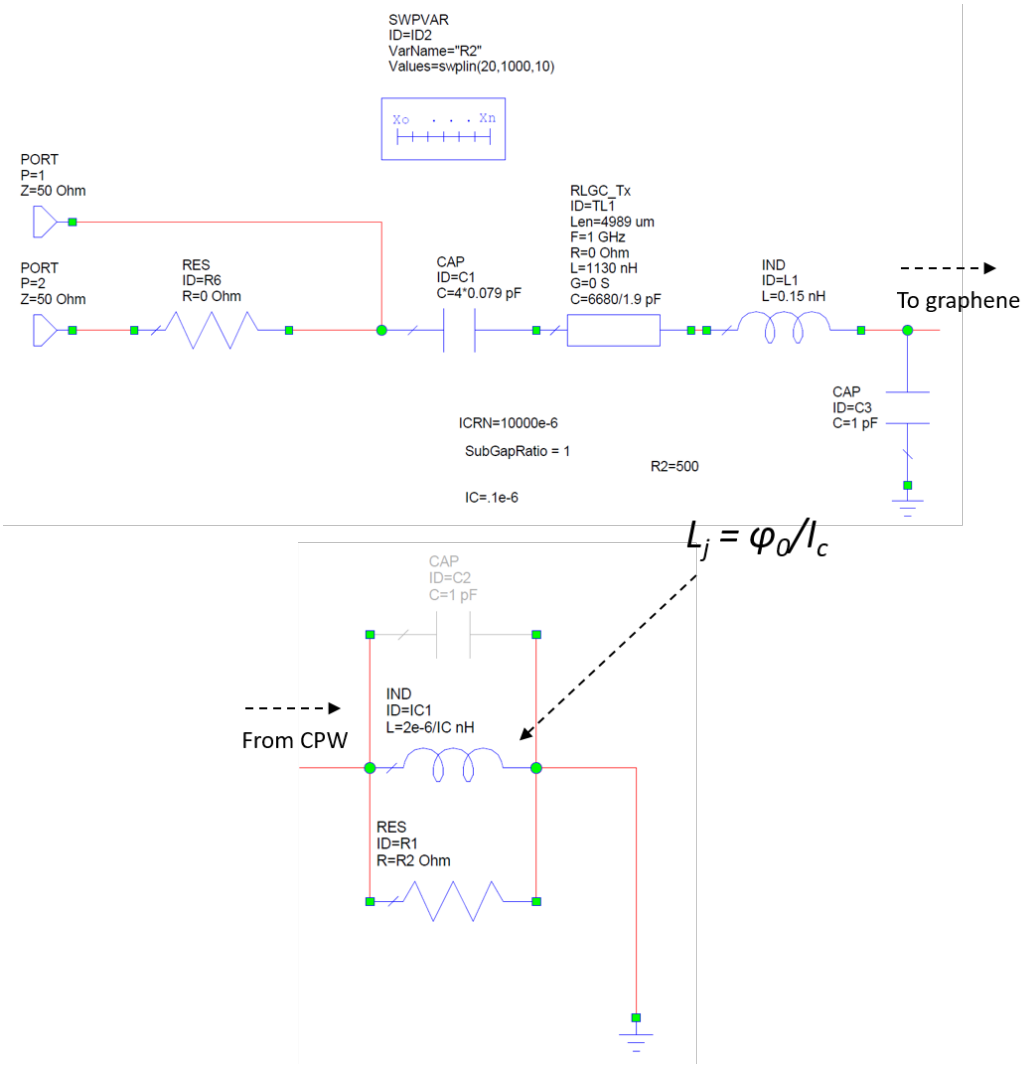

Figure F.1: Snapshot of the parameters used in National Instruments microwave design module.

BIBLIOGRAPHY

[1] Novoselov, K. S. *et al.* Electric field effect in atomically thin carbon films. *Science* **306**, 666–669 (2004).

[2] Nan, H. Y. *et al.* The thermal stability of graphene in air investigated by Raman spectroscopy. *Journal of Raman Spectroscopy* **44**, 1018–1021 (2013).

[3] Geim, A. K. & Novoselov, K. S. The rise of graphene. *Nature Materials* **6**, 183–191 (2007).

[4] Novoselov, K. S. *et al.* Room-Temperature Quantum Hall Effect in Graphene. *Science* **315**, 1379 (2007).

[5] Lee, C., Wei, X., Kysar, J. W. & Hone, J. Measurement of the Elastic Properties and Intrinsic Strength of Monolayer Graphene. *Science* **321**, 385–388 (2008).

[6] Balandin, A. A. *et al.* Superior Thermal Conductivity of Single-Layer Graphene. *Nano Letters* **8**, 902–907 (2008).

[7] Pop, E., Varshney, V. & Roy, A. K. Thermal properties of graphene: Fundamentals and applications. *MRS Bulletin* **37**, 1273–1281 (2012).

[8] Mill, J. S. *A System of Logic, Ratiocinative and Inductive: Being a Connected View of the Principles of Evidence and the Methods of Scientific Investigation* (Harper, 1846).

[9] Anderson, P. W. More Is Different. *Science* **177**, 393–396 (1972).

[10] Wigner, E. & Seitz, F. *Solid State Physics* **1**, 97 (1955).

[11] Cao, Y. *et al.* Unconventional superconductivity in magic-angle graphene superlattices. *Nature* **556**, 43–50 (2018).

[12] Cao, Y. *et al.* Correlated insulator behaviour at half-filling in magic-angle graphene superlattices. *Nature* **556**, 80–84 (2018).

[13] Sharpe, A. L. *et al.* Emergent ferromagnetism near three-quarters filling in twisted bilayer graphene. *Science* **365**, 605–608 (2019).

[14] Efetov, D. K. *et al.* Specular interband Andreev reflections at van der Waals interfaces between graphene and NbSe 2. *Nature Physics* **12**, 328–332 (2016).

[15] Island, J. O. *et al.* Spin–orbit-driven band inversion in bilayer graphene by the van der Waals proximity effect. *Nature* **571**, 85–89 (2019).

[16] Fei, Z. *et al.* Ferroelectric switching of a two-dimensional metal. *Nature* **560**, 336–339 (2018).

[17] Wang, Z. *et al.* Very large tunneling magnetoresistance in layered magnetic semiconductor CrI 3. *Nature Communications* **9**, 1–8 (2018).

[18] Kane, C. L. & Mele, E. J. Z_2 topological order and the quantum spin hall effect. *Phys. Rev. Lett.* **95**, 146802 (2005).

[19] Chen, G. *et al.* Evidence of a gate-tunable Mott insulator in a trilayer graphene moiré superlattice. *Nature Physics* **15**, 237–241 (2019).

[20] Regan, E. C. *et al.* Mott and generalized Wigner crystal states in WSe 2 /WS 2 moiré superlattices. *Nature* **579**, 359–363 (2020).

[21] Tang, Y. *et al.* Simulation of Hubbard model physics in WSe 2 /WS 2 moiré superlattices. *Nature* **579**, 353–358 (2020).

[22] Wang, L. *et al.* Magic continuum in twisted bilayer WSe2. *arXiv:1910.12147* (2019).

[23] Cao, Y. *et al.* Quality Heterostructures from Two-Dimensional Crystals Unstable in Air by Their Assembly in Inert Atmosphere. *Nano Letters* **15**, 4914–4921 (2015).

[24] Li, L. *et al.* Quantum oscillations in a two-dimensional electron gas in black phosphorus thin films. *Nature Nanotechnology* **10**, 608–613 (2015).

[25] Beenakker, C. W. J. Colloquium: Andreev reflection and klein tunneling in graphene. *Rev. Mod. Phys.* **80**, 1337–1354 (2008).

[26] Katsnelson, M. I., Novoselov, K. S. & Geim, A. K. Chiral tunnelling and the Klein paradox in graphene. *Nature Physics* **2**, 620–625 (2006).

[27] Shytov, A. V., Rudner, M. S. & Levitov, L. S. Klein backscattering and fabry-pérot interference in graphene heterojunctions. *Phys. Rev. Lett.* **101**, 156804 (2008).

[28] Young, A. F. & Kim, P. Quantum interference and Klein tunnelling in graphene heterojunctions. *Nature Physics* **5**, 222–226 (2009).

[29] Stander, N., Huard, B. & Goldhaber-Gordon, D. Evidence for klein tunneling in graphene $p-n$ junctions. *Phys. Rev. Lett.* **102**, 026807 (2009).

[30] Klitzing, K. v., Dorda, G. & Pepper, M. New method for high-accuracy determination of the fine-structure constant based on quantized hall resistance. *Phys. Rev. Lett.* **45**, 494–497 (1980).

[31] Haldane, F. D. M. Model for a quantum hall effect without landau levels: Condensed-matter realization of the "parity anomaly". *Phys. Rev. Lett.* **61**, 2015–2018 (1988).

[32] Bernevig, B. A. & Zhang, S.-C. Quantum Spin Hall Effect. *Physical Review Letters* **96**, 106802 (2006).

[33] Kane, C. L. & Mele, E. J. Quantum Spin Hall Effect in Graphene. *Physical Review Letters* **95**, 226801 (2005).

[34] Liu, C.-X., Zhang, S.-C. & Qi, X.-L. The Quantum Anomalous Hall Effect: Theory and Experiment. *Annual Review of Condensed Matter Physics* **7**, 301–321 (2016).

[35] Jung, J., DaSilva, A. M., MacDonald, A. H. & Adam, S. Origin of band gaps in graphene on hexagonal boron nitride. *Nature Communications* **6**, 6308 (2015).

[36] Hunt, B. *et al.* Massive Dirac Fermions and Hofstadter Butterfly in a van der Waals Heterostructure. *Science* **340**, 1427 (2013).

[37] Ponomarenko, L. A. *et al.* Cloning of Dirac fermions in graphene superlattices. *Nature* **497**, 594–597 (2013).

[38] Dean, C. R. *et al.* Hofstadter's butterfly and the fractal quantum Hall effect in moiré superlattices. *Nature* **497**, 598–602 (2013).

[39] Serlin, M. *et al.* Intrinsic quantized anomalous Hall effect in a moiré heterostructure. *Science* (2019).

[40] Topology in Condensed Matter: Tying Quantum Knots. URL https://www.edx.org/course/topology-in-condensed-matter-tying-quantum-knots.

[41] König, M. *et al.* Quantum Spin Hall Insulator State in HgTe Quantum Wells. *Science* **318**, 766–770 (2007).

[42] Wu, S. *et al.* Observation of the quantum spin Hall effect up to 100 kelvin in a monolayer crystal. *Science* **359**, 76–79 (2018).

[43] Qian, X., Liu, J., Fu, L. & Li, J. Quantum spin hall effect in two-dimensional transition metal dichalcogenides. *Science* **346**, 1344–1347 (2014).

[44] Weeks, C., Hu, J., Alicea, J., Franz, M. & Wu, R. Engineering a robust quantum spin hall state in graphene via adatom deposition. *Phys. Rev. X* **1**, 021001 (2011).

[45] Zihlmann, S. *et al.* Large spin relaxation anisotropy and valley-zeeman spin-orbit coupling in wse_2/graphene/h-bn heterostructures. *Phys. Rev. B* **97**, 075434 (2018).

[46] Wang, D. *et al.* Quantum Hall Effect Measurement of Spin–Orbit Coupling Strengths in Ultraclean Bilayer Graphene/WSe2 Heterostructures. *Nano Letters* **19**, 7028–7034 (2019).

[47] Wakamura, T. *et al.* Spin-orbit interaction induced in graphene by transition metal dichalcogenides. *Physical Review B* **99**, 245402 (2019).

[48] Manchon, A., Koo, H. C., Nitta, J., Frolov, S. M. & Duine, R. A. New perspectives for Rashba spin–orbit coupling. *Nature Materials* **14**, 871–882 (2015).

[49] Wang, Z. *et al.* Origin and Magnitude of 'Designer' Spin-Orbit Interaction in Graphene on Semiconducting Transition Metal Dichalcogenides. *Physical Review X* **6**, 041020 (2016).

[50] Heersche, H. B., Jarillo-Herrero, P., Oostinga, J. B., Vandersypen, L. M. K. & Morpurgo, A. F. Bipolar supercurrent in graphene. *Nature* **446**, 56–59 (2007).

[51] Weller, T. E., Ellerby, M., Saxena, S. S., Smith, R. P. & Skipper, N. T. Superconductivity in the intercalated graphite compounds C6Yb and C6Ca. *Nature Physics* **1**, 39–41 (2005).

[52] Emery, N. *et al.* Superconductivity of bulk CaC_6. *Phys. Rev. Lett.* **95**, 087003 (2005).

[53] Tinkham, M. *Introduction to Superconductivity* (Courier Corporation, 2004).

[54] Profeta, G., Calandra, M. & Mauri, F. Phonon-mediated superconductivity in graphene by lithium deposition. *Nature Physics* **8**, 131–134 (2012).

[55] Nandkishore, R., Levitov, L. S. & Chubukov, A. V. Chiral superconductivity from repulsive interactions in doped graphene. *Nature Physics* **8**, 158–163 (2012).

[56] Shankar, R. Renormalization-group approach to interacting fermions. *Rev. Mod. Phys.* **66**, 129–192 (1994).

[57] Dzyaloshinskii, I. E. Superconducting transitions due to van hove singularities in the electron spectrum. *Sov. Phys. JETP* **66**, 848–854 (1987).

[58] Ludbrook, B. M. *et al.* Evidence for superconductivity in Li-decorated monolayer graphene. *Proceedings of the National Academy of Sciences* **112**, 11795 (2015).

[59] Tiwari, A. P. *et al.* Superconductivity at 7.4K in few layer graphene by li-intercalation. *Journal of Physics: Condensed Matter* **29**, 445701 (2017).

[60] Chapman, J. *et al.* Superconductivity in Ca-doped graphene laminates. *Scientific Reports* **6**, 1–6 (2016).

[61] Ichinokura, S., Sugawara, K., Takayama, A., Takahashi, T. & Hasegawa, S. Superconducting Calcium-Intercalated Bilayer Graphene. *ACS Nano* **10**, 2761–2765 (2016).

[62] Cartlidge, E. Graphene superconductivity seen. *Physics World* **28**, 6–7 (2015).

[63] Efetov, D. K. *Towards inducing superconductivity into graphene*. Ph.D. thesis, Columbia University (2014).

[64] Ye, J. T. *et al.* Superconducting Dome in a Gate-Tuned Band Insulator. *Science* **338**, 1193–1196 (2012).

[65] Yankowitz, M. *et al.* Emergence of superlattice Dirac points in graphene on hexagonal boron nitride. *Nature Physics* **8**, 382–386 (2012).

[66] Lopes dos Santos, J. M. B., Peres, N. M. R. & Castro Neto, A. H. Graphene bilayer with a twist: Electronic structure. *Phys. Rev. Lett.* **99**, 256802 (2007).

[67] Schmidt, H. *et al.* Tunable graphene system with two decoupled monolayers. *Applied Physics Letters* **93**, 172108 (2008).

[68] Li, G. *et al.* Observation of Van Hove singularities in twisted graphene layers. *Nature Physics* **6**, 109–113 (2010).

[69] Sanchez-Yamagishi, J. D. *et al.* Quantum hall effect, screening, and layer-polarized insulating states in twisted bilayer graphene. *Phys. Rev. Lett.* **108**, 076601 (2012).

[70] Sanchez-Yamagishi, J. D. *et al.* Helical edge states and fractional quantum Hall effect in a graphene electron–hole bilayer. *Nature Nanotechnology* **12**, 118–122 (2017).

[71] Choi, Y. *et al.* Electronic correlations in twisted bilayer graphene near the magic angle. *Nature Physics* **15**, 1174–1180 (2019).

[72] Bistritzer, R. & MacDonald, A. H. Moiré bands in twisted double-layer graphene. *Proceedings of the National Academy of Sciences* **108**, 12233–12237 (2011).

[73] Kim, K. *et al.* Van der Waals Heterostructures with High Accuracy Rotational Alignment. *Nano Letters* **16**, 1989–1995 (2016).

[74] Cao, Y. *et al.* Superlattice-Induced Insulating States and Valley-Protected Orbits in Twisted Bilayer Graphene. *Physical Review Letters* **117**, 116804 (2016).

[75] Kim, K. *et al.* Tunable moiré bands and strong correlations in small-twist-angle bilayer graphene. *Proceedings of the National Academy of Sciences* **114**, 3364–3369 (2017).

[76] Lee, D. S. *et al.* Quantum hall effect in twisted bilayer graphene. *Phys. Rev. Lett.* **107**, 216602 (2011).

[77] Schmidt, H., Rode, J. C., Smirnov, D. & Haug, R. J. Superlattice structures in twisted bilayers of folded graphene. *Nature Communications* **5**, 5742 (2014).

[78] Lu, X. *et al.* Superconductors, orbital magnets and correlated states in magic-angle bilayer graphene. *Nature* **574**, 653–657 (2019).

[79] MacDonald, A. H. Trend: Bilayer Graphene's Wicked, Twisted Road. *Physics* **12** (2019).

[80] Yankowitz, M. *et al.* Tuning superconductivity in twisted bilayer graphene. *Science* **363**, 1059–1064 (2019).

[81] Lantos, A. *Topology in Modern Solid State Physics: From Topological Insulators to Weyl Semimetals*. Ph.D. thesis (2019).

[82] Chen, S. *et al.* Electrically tunable correlated and topological states in twisted monolayer-bilayer graphene. *arXiv:2004.11340* (2020).

[83] Polshyn, H. *et al.* Nonvolatile switching of magnetic order by electric fields in an orbital Chern insulator. *arXiv:2004.11353* (2020).

[84] Witczak-Krempa, W., Chen, G., Kim, Y. B. & Balents, L. Correlated Quantum Phenomena in the Strong Spin-Orbit Regime. *Annual Review of Condensed Matter Physics* **5**, 57–82 (2014).

[85] Rau, J. G., Lee, E. K.-H. & Kee, H.-Y. Spin-orbit physics giving rise to novel phases in correlated systems: Iridates and related materials. *Annual Review of Condensed Matter Physics* **7**, 195–221 (2016).

[86] Zhang, Y., Tan, Y.-W., Stormer, H. L. & Kim, P. Experimental observation of the quantum Hall effect and Berry's phase in graphene. *Nature* **438**, 201–204 (2005).

[87] Du, X., Skachko, I., Barker, A. & Andrei, E. Y. Approaching ballistic transport in suspended graphene. *Nature Nanotechnology* **3**, 491–495 (2008).

[88] Bolotin, K. I. *et al.* Ultrahigh electron mobility in suspended graphene. *Solid State Communications* **146**, 351–355 (2008).

[89] Bolotin, K. I., Sikes, K. J., Hone, J., Stormer, H. L. & Kim, P. Temperature-dependent transport in suspended graphene. *Phys. Rev. Lett.* **101**, 096802 (2008).

[90] Bolotin, K. I., Ghahari, F., Shulman, M. D., Stormer, H. L. & Kim, P. Observation of the fractional quantum Hall effect in graphene. *Nature* **462**, 196–199 (2009).

[91] Du, X., Skachko, I., Duerr, F., Luican, A. & Andrei, E. Y. Fractional quantum Hall effect and insulating phase of Dirac electrons in graphene. *Nature* **462**, 192–195 (2009).

[92] Dean, C. R. *et al.* Boron nitride substrates for high-quality graphene electronics. *Nature Nanotechnology* **5**, 722–726 (2010).

[93] Kretinin, A. V. *et al.* Electronic Properties of Graphene Encapsulated with Different Two-Dimensional Atomic Crystals. *Nano Letters* **14**, 3270–3276 (2014).

[94] Yankowitz, M. *et al.* Intrinsic disorder in graphene on transition metal dichalcogenide heterostructures. *Nano Letters* **15**, 1925–1929 (2015).

[95] Kerelsky, A. *et al.* Maximized electron interactions at the magic angle in twisted bilayer graphene. *Nature* **572**, 95–100 (2019).

[96] Xie, Y. *et al.* Spectroscopic signatures of many-body correlations in magic-angle twisted bilayer graphene. *Nature* **572**, 101–105 (2019).

[97] Jiang, Y. *et al.* Charge order and broken rotational symmetry in magic-angle twisted bilayer graphene. *Nature* **573**, 91–95 (2019).

[98] Koshino, M. *et al.* Maximally Localized Wannier Orbitals and the Extended Hubbard Model for Twisted Bilayer Graphene. *Physical Review X* **8**, 031087 (2018).

[99] Polshyn, H. *et al.* Large linear-in-temperature resistivity in twisted bilayer graphene. *Nature Physics* **15**, 1011–1016 (2019).

[100] Lilly, M. P. *et al.* Resistivity of Dilute 2D Electrons in an Undoped GaAs Heterostructure. *Physical Review Letters* **90**, 056806 (2003).

[101] Stepanov, P. *et al.* The interplay of insulating and superconducting orders in magic-angle graphene bilayers. *arXiv:1911.09198 [cond-mat]* (2019). 1911.09198.

[102] Saito, Y., Ge, J., Watanabe, K., Taniguchi, T. & Young, A. F. Decoupling superconductivity and correlated insulators in twisted bilayer graphene. *arXiv:1911.13302 [cond-mat]* (2019). 1911.13302.

[103] Lee, P. A., Nagaosa, N. & Wen, X.-G. Doping a Mott insulator: Physics of high-temperature superconductivity. *Reviews of Modern Physics* **78**, 17–85 (2006).

[104] Stewart, G. R. Heavy-fermion systems. *Reviews of Modern Physics* **56**, 755–787 (1984).

[105] Ardavan, A. *et al.* Recent Topics of Organic Superconductors. *Journal of the Physical Society of Japan* **81**, 011004 (2011).

[106] Stewart, G. R. Superconductivity in iron compounds. *Reviews of Modern Physics* **83**, 1589–1652 (2011).

[107] Lian, B., Wang, Z. & Bernevig, B. A. Twisted Bilayer Graphene: A Phonon-Driven Superconductor. *Physical Review Letters* **122**, 257002 (2019).

[108] Wu, F., Hwang, E. & Das Sarma, S. Phonon-induced giant linear-in-T resistivity in magic angle twisted bilayer graphene: Ordinary strangeness and exotic superconductivity. *Physical Review B* **99**, 165112 (2019).

[109] Wang, L. *et al.* One-dimensional electrical contact to a two-dimensional material. *Science* **342**, 614–617 (2013).

[110] Isobe, H., Yuan, N. F. Q. & Fu, L. Unconventional superconductivity and density waves in twisted bilayer graphene. *Phys. Rev. X* **8**, 041041 (2018).

[111] Liu, C.-C., Zhang, L.-D., Chen, W.-Q. & Yang, F. Chiral spin density wave and $d + id$ superconductivity in the magic-angle-twisted bilayer graphene. *Phys. Rev. Lett.* **121**, 217001 (2018).

[112] Zondiner, U. *et al.* Cascade of Phase Transitions and Dirac Revivals in Magic Angle Graphene. *arXiv:1912.06150 [cond-mat]* (2019). 1912.06150.

[113] Wong, D. *et al.* Cascade of transitions between the correlated electronic states of magic-angle twisted bilayer graphene. *arXiv:1912.06145 [cond-mat]* (2019). 1912.06145.

[114] Guinea, F. & Walet, N. R. Electrostatic effects, band distortions, and superconductivity in twisted graphene bilayers. *Proceedings of the National Academy of Sciences* **115**, 13174–13179 (2018).

[115] You, Y.-Z. & Vishwanath, A. Superconductivity from valley fluctuations and approximate SO(4) symmetry in a weak coupling theory of twisted bilayer graphene. *npj Quantum Materials* **4**, 1–12 (2019).

[116] Kozii, V., Isobe, H., Venderbos, J. W. F. & Fu, L. Nematic superconductivity stabilized by density wave fluctuations: Possible application to twisted bilayer graphene. *Physical Review B* **99**, 144507 (2019).

[117] Gu, X. *et al.* Antiferromagnetism and chiral d-wave superconductivity from an effective $t-J-D$ model for twisted bilayer graphene. *arXiv:1902.00029 [cond-mat]* (2019). 1902.00029.

[118] Lopes dos Santos, J. M. B., Peres, N. M. R. & Castro Neto, A. H. Graphene Bilayer with a Twist: Electronic Structure. *Physical Review Letters* **99**, 256802 (2007).

[119] Gmitra, M. & Fabian, J. Graphene on transition-metal dichalcogenides: A platform for proximity spin-orbit physics and optospintronics. *Physical Review B* **92**, 155403 (2015).

[120] Zaletel, M. P. & Khoo, J. Y. The gate-tunable strong and fragile topology of multilayer-graphene on a transition metal dichalcogenide. *arXiv:1901.01294 [cond-mat]* (2019). 1901.01294.

[121] Gmitra, M., Kochan, D., Högl, P. & Fabian, J. Trivial and inverted Dirac bands and the emergence of quantum spin Hall states in graphene on transition-metal dichalcogenides. *Physical Review B* **93**, 155104 (2016).

[122] Kane, C. L. & Mele, E. J. Quantum Spin Hall Effect in Graphene. *Physical Review Letters* **95**, 226801 (2005).

[123] Min, H. *et al.* Intrinsic and Rashba spin-orbit interactions in graphene sheets. *Physical Review B* **74**, 165310 (2006).

[124] Yao, Y., Ye, F., Qi, X.-L., Zhang, S.-C. & Fang, Z. Spin-orbit gap of graphene: First-principles calculations. *Physical Review B* **75**, 041401 (2007).

[125] Sichau, J. *et al.* Resonance Microwave Measurements of an Intrinsic Spin-Orbit Coupling Gap in Graphene: A Possible Indication of a Topological State. *Physical Review Letters* **122**, 046403 (2019).

[126] Nam, N. N. T. & Koshino, M. Lattice relaxation and energy band modulation in twisted bilayer graphene. *Physical Review B* **96**, 075311 (2017).

[127] Po, H. C., Zou, L., Vishwanath, A. & Senthil, T. Origin of Mott Insulating Behavior and Superconductivity in Twisted Bilayer Graphene. *Physical Review X* **8**, 031089 (2018).

[128] Carr, S., Fang, S., Zhu, Z. & Kaxiras, E. Exact continuum model for low-energy electronic states of twisted bilayer graphene. *Physical Review Research* **1**, 013001 (2019).

[129] Goodwin, Z. A. H., Corsetti, F., Mostofi, A. A. & Lischner, J. Twist-angle sensitivity of electron correlations in moir\'e graphene bilayers. *Physical Review B* **100**, 121106 (2019).

[130] Pizarro, J. M., Rösner, M., Thomale, R., Valentí, R. & Wehling, T. O. Internal screening and dielectric engineering in magic-angle twisted bilayer graphene. *Physical Review B* **100**, 161102 (2019).

[131] Uri, A. *et al.* Mapping the twist angle and unconventional Landau levels in magic angle graphene. *arXiv:1908.04595 [cond-mat]* (2019). 1908.04595.

[132] Codecido, E. *et al.* Correlated insulating and superconducting states in twisted bilayer graphene below the magic angle. *Science Advances* **5**, eaaw9770 (2019).

[133] Yoo, H. *et al.* Atomic and electronic reconstruction at the van der Waals interface in twisted bilayer graphene. *Nature Materials* **18**, 448–453 (2019).

[134] Anderson, P. W. Absence of Diffusion in Certain Random Lattices. *Physical Review* **109**, 1492–1505 (1958).

[135] Ihn, T. *Semiconductor Nanostructures: Quantum states and electronic transport* (Oxford University Press, 2009).

[136] Senz, V. *et al.* Coexistence of weak localization and a metallic phase in si/sige quantum wells. *Phys. Rev. B* **61**, R5082–R5085 (2000).

[137] Senz, V. *et al.* Analysis of the metallic phase of two-dimensional holes in sige in terms of temperature dependent screening. *Phys. Rev. Lett.* **85**, 4357–4360 (2000).

[138] Bergmann, G. Consistent temperature and field dependence in weak localization. *Phys. Rev. B* **28**, 515–522 (1983).

[139] Spin-Orbit Interaction and Magnetoresistance in the Two Dimensional Random System. *Prog. Theor. Phys.* **63**, 707 (1980).

[140] Bergmann, G. Weak anti-localization—An experimental proof for the destructive interference of rotated spin 12. *Solid State Communications* **42**, 815–817 (1982).

[141] Tikhonenko, F. V., Kozikov, A. A., Savchenko, A. K. & Gorbachev, R. V. Transition between Electron Localization and Antilocalization in Graphene. *Physical Review Letters* **103**, 226801 (2009).

[142] McCann, E. *et al.* Weak-localization magnetoresistance and valley symmetry in graphene. *Phys. Rev. Lett.* **97**, 146805 (2006).

[143] McCann, E. & Fal'ko, V. I. $z \rightarrow -z$ symmetry of spin-orbit coupling and weak localization in graphene. *Phys. Rev. Lett.* **108**, 166606 (2012).

[144] Wang, Z. *et al.* Strong interface-induced spin–orbit interaction in graphene on WS2. *Nature Communications* **6**, 8339 (2015).

[145] Couto, N. J. G. *et al.* Random strain fluctuations as dominant disorder source for high-quality on-substrate graphene devices. *Phys. Rev. X* **4**, 041019 (2014).

[146] Kumar, C. *et al.* Localization physics in graphene moiré superlattices. *Phys. Rev. B* **98**, 155408 (2018).

[147] Wu, F., Hwang, E. & Das Sarma, S. Phonon-induced giant linear-in-t resistivity in magic angle twisted bilayer graphene: Ordinary strangeness and exotic superconductivity. *Phys. Rev. B* **99**, 165112 (2019).

[148] Chung, T.-F., Xu, Y. & Chen, Y. P. Transport measurements in twisted bilayer graphene: Electron-phonon coupling and landau level crossing. *Phys. Rev. B* **98**, 035425 (2018).

[149] Neto, A. C., Guinea, F., Peres, N. M., Novoselov, K. S. & Geim, A. K. The electronic properties of graphene. *Reviews of modern physics* **81**, 109–162 (2009).

[150] Bultinck, N. *et al.* Ground State and Hidden Symmetry of Magic Angle Graphene at Even Integer Filling. *arXiv:1911.02045* (2019).

[151] Banerjee, M. *et al.* Observed quantization of anyonic heat flow. *Nature* **545**, 75–79 (2017).

[152] Banerjee, M. *et al.* Observation of half-integer thermal Hall conductance. *Nature* **559**, 205–210 (2018).

[153] Schwab, K., Henriksen, E. A., Worlock, J. M. & Roukes, M. L. Measurement of the quantum of thermal conductance. *Nature* **404**, 974–977 (2000).

[154] Calado, V. E. *et al.* Ballistic Josephson junctions in edge-contacted graphene. *Nature Nanotechnology* **10**, 761–764 (2015).

[155] Draelos, A. W. *et al.* Supercurrent Flow in Multiterminal Graphene Josephson Junctions. *Nano Letters* **19**, 1039–1043 (2019).

[156] Wang, J. I.-J. *et al.* Coherent control of a hybrid superconducting circuit made with graphene-based van der Waals heterostructures. *Nature Nanotechnology* **14**, 120–125 (2019).

[157] Fong, K. C. *et al.* Measurement of the Electronic Thermal Conductance Channels and Heat Capacity of Graphene at Low Temperature. *Physical Review X* **3**, 041008 (2013).

[158] Efetov, D. K. *et al.* Fast thermal relaxation in cavity-coupled graphene bolometers with a Johnson noise read-out. *Nature Nanotechnology* **13**, 797–801 (2018).

[159] Jauregui, L. A. *et al.* Thermal Transport in Graphene Nanostructures: Experiments and Simulations. *ECS Transactions* **28**, 73 (2010).

[160] Fong, K. C. & Schwab, K. C. Ultrasensitive and Wide-Bandwidth Thermal Measurements of Graphene at Low Temperatures. *Physical Review X* **2**, 031006 (2012).

[161] Zhu, M. *et al.* Supercurrent and multiple Andreev reflections in micrometer-long ballistic graphene Josephson junctions. *Nanoscale* **10**, 3020–3025 (2018).

[162] Schmidt, F. E., Jenkins, M. D., Watanabe, K., Taniguchi, T. & Steele, G. A. A ballistic graphene superconducting microwave circuit. *Nature Communications* **9**, 1–7 (2018).

[163] Borzenets, I. V. *et al.* Phonon Bottleneck in Graphene-Based Josephson Junctions at Millikelvin Temperatures. *Physical Review Letters* **111**, 027001 (2013).

[164] Draelos, A. W. *et al.* Subkelvin lateral thermal transport in diffusive graphene. *Physical Review B* **99**, 125427 (2019).

[165] Halbertal, D. *et al.* Nanoscale thermal imaging of dissipation in quantum systems. *Nature* **539**, 407–410 (2016).

[166] Halbertal, D. *et al.* Imaging resonant dissipation from individual atomic defects in graphene. *Science* **358**, 1303–1306 (2017).

[167] Kong, J. F., Levitov, L., Halbertal, D. & Zeldov, E. Resonant electron-lattice cooling in graphene. *Phys. Rev. B* **97**, 245416 (2018).

[168] Lee, G.-H. *et al.* Graphene-based Josephson junction microwave bolometer. *arXiv:1909.05413 [astro-ph, physics:cond-mat, physics:quant-ph]* (2019).

[169] Betz, A. C. *et al.* Hot electron cooling by acoustic phonons in graphene. *Phys. Rev. Lett.* **109**, 056805 (2012).

[170] Betz, A. C. *et al.* Supercollision cooling in undoped graphene. *Nature Physics* **9**, 109–112 (2013).

[171] Yang, W. *et al.* A graphene Zener–Klein transistor cooled by a hyperbolic substrate. *Nature Nanotechnology* **13**, 47–52 (2018).

[172] Levine, J. L. & Hsieh, S. Y. Recombination time of quasiparticles in superconducting aluminum. *Phys. Rev. Lett.* **20**, 994–997 (1968).

[173] Xie, M. & MacDonald, A. Nature of the Correlated Insulator States in Twisted Bilayer Graphene. *Physical Review Letters* **124**, 097601 (2020).

[174] Cao, Y. *et al.* Strange metal in magic-angle graphene with near Planckian dissipation. *arXiv:1901.03710 [cond-mat]* (2019). 1901.03710.

[175] de Picciotto, R. *et al.* Direct observation of a fractional charge. *Nature* **389**, 162–164 (1997).

[176] Zhou, P. *et al.* Electron pairing in the pseudogap state revealed by shot noise in copper oxide junctions. *Nature* **572**, 493–496 (2019).

[177] Nika, D. L., Cocemasov, A. I. & Balandin, A. A. Specific heat of twisted bilayer graphene: Engineering phonons by atomic plane rotations. *Applied Physics Letters* **105**, 031904 (2014).

[178] Seifert, P. *et al.* Magic-angle bilayer graphene nano-calorimeters – towards broadband, energy-resolving single photon detection. *arXiv:1911.04403* (2019).

[179] Veyrat, L. *et al.* Helical quantum Hall phase in graphene on SrTiO3. *Science* **367**, 781–786 (2020).

[180] Sajadi, E. *et al.* Gate-induced superconductivity in a monolayer topological insulator. *Science* **362**, 922–925 (2018).

[181] Fatemi, V. *et al.* Electrically tunable low-density superconductivity in a monolayer topological insulator. *Science* **362**, 926–929 (2018).

[182] Fu, L. & Kane, C. L. Josephson current and noise at a superconductor/quantum-spin-hall-insulator/superconductor junction. *Phys. Rev. B* **79**, 161408 (2009).

[183] Cybart, S. A. *et al.* Nano Josephson superconducting tunnel junctions in YBa2Cu3O7–δ directly patterned with a focused helium ion beam. *Nature Nanotechnology* **10**, 598–602 (2015).

[184] Mills, S. A. *et al.* Single-crystal superconducting nanowires of $NbSe_2$ fabricated by reactive plasma etching. *Applied Physics Letters* **104**, 052604 (2014).